

Monitoring the film formation during sputter deposition of vanadium
carbide by *in situ* X-ray reflectivity measurements

Zur Erlangung des akademischen Grades eines
DOKTORS DER NATURWISSENSCHAFTEN
von der Fakultät für Physik des
Karlsruher Institut für Technologie (KIT)

genehmigte

DISSERTATION

von

Dipl.-Phys. Marthe Kaufholz
aus Heidelberg

Tag der mündlichen Prüfung: 21.11.2014
Referent: Prof. Dr. Tilo Baumbach
Korreferentin: Prof. Dr. Dagmar Gerthsen

Contents

Introduction	1
I Fabrication, properties and analysis methods for hard coating materials	5
1 Sputter deposition from a compound target	7
1.1 The sputter process	7
1.1.1 Ignition of the plasma	8
1.1.2 Interaction of the plasma species with the target atoms	9
1.1.3 Motion of the target atoms through the gas phase	11
1.1.4 Interaction of plasma species and the substrate	14
1.2 Thin film formation	15
1.3 Summary	17
2 Hard coating materials	19
2.1 Hard materials: monocarbides of transition metals	19
2.2 Influence of the chemical composition	20
2.3 Multilayer coatings	23
2.4 Summary	24
3 X-ray reflectivity (XRR)	25
3.1 Scattering of X-rays	25
3.2 Specular X-ray reflectivity	27
3.3 Characteristic features of the specular XRR curve	28
3.3.1 The critical angle	29
3.3.2 Kiessig fringes	30
3.3.3 Influence of roughness	30
3.4 Diffuse scattering	32
4 X-ray Photoemission spectroscopy (XPS)	35
4.1 Basics of X-ray photoemission spectroscopy	35
4.2 Characteristics of XPS spectra	36

II	Experimental Details & Simulations of the sputter process	39
5	Experimental details	41
5.1	The portable sputter chamber system at IPS	41
5.2	Sample preparation	42
5.3	Experimental setup for the synchrotron experiments	45
5.3.1	Ångstromquelle Karlsruhe	45
5.3.2	The Max-Planck Beamline at ANKA	46
5.4	X-ray reflectivity measurements	48
5.4.1	<i>Angle-dependent</i> XRR measurements	48
5.4.2	<i>Stationary</i> XRR measurements	50
5.5	X-ray Photoemission spectroscopy measurements at the UHV Analysis Laboratory	53
5.5.1	The UHV Analysis Laboratory	53
5.5.2	XPS measurements	53
5.6	Further complementary methods	55
6	Simulations of the sputter process	57
6.1	The sputter process at the target position	57
6.2	Travel of the particles through the gas phase	60
6.3	Summary	62
III	Monitoring the film formation	65
7	Optimization of the <i>in situ</i> XRR measurement	67
8	Simulation of the <i>in situ</i> XRR curves	71
8.1	Parratt algorithm for growing films	71
8.2	Calculation of the rate of the thickness increase	72
8.3	Influence of the experimental setup	75
9	Influence of the DC power on the thin film formation	79
9.1	<i>Stationary</i> measurements	79
9.2	Determination of the rate of the thickness increase	81
9.3	Microstructural changes at different DC power	81
9.4	Simulations of the sputtering process at different DC powers	83
9.5	Discussion & summary	86
10	Influence of the Pressure on the Thin Film Formation	89
10.1	<i>In situ</i> XRR measurements at different working gas pressures	89
10.2	Angle-dependent XRR measurements before and after growth	91
10.3	Simulations of the <i>in situ</i> XRR measurements	92

10.4	Simulations of the sputtering process at different gas pressures	94
10.5	X-ray spectroscopy measurements	95
10.5.1	Qualitative analysis of the XPS spectra	95
10.5.2	Quantitative analysis of the XPS spectra	95
10.6	Discussion: Pressure-induced variations of the chemical composition	98
10.7	Texture investigations	100
10.8	Summary & conclusion	102
11	Initial growth of a VC thin film	103
11.1	Characterization of the Si substrates	103
11.2	<i>In situ</i> measurements of the specular reflectivity	104
11.3	X-ray reflectivity after growth for different initial pressure	108
11.4	Transmission electron microscopy	111
11.5	Summary & proposed growth models	112
12	Simulation of <i>in situ</i> X-ray reflectivity measurements	115
12.1	Growth model	115
12.2	Influence of the distance L of the islands	119
12.3	Influence of the shape of the islands	122
12.4	Influence of the deposition rate	125
12.5	Comparison with the experimental data	126
12.6	Summary	127
13	Tailoring the microstructure	129
13.1	Periodic interruption of the growth process	129
13.2	Confirmation of the multilayer structure after deposition	134
13.3	Influence of the growth interruption	138
13.4	Summary & discussion	142
	Summary & outlook	143
	References	148
	List of figures and tables	160
	Appendix: Growth model: Calculations	170
	Acknowledgements	174

Introduction

Magnetron sputtered polycrystalline coatings are widely used, e.g. as protective hard coatings for cutting tools and medical implants, or as anti-reflection coatings for solar cells and glasses. For such applications, usually a coating thickness in the micrometer regime is desired. Hence the industrial sputter process typically involves high deposition rates (nm/s) and long deposition times (up to hours).

The deposition conditions during the sputter process affect different aspects of the microstructure such as roughness, texture, and grain size of the film. The microstructure, in turn, influences the optical and mechanical properties of the coating. The exact relation between deposition conditions and microstructure formation is not yet fully understood. Monitoring the material distribution during growth, however, can give valuable information about the thin film formation.

In situ X-ray Reflectivity (XRR) measurements are non-destructive and compatible with the pressure conditions during sputter deposition. Due to their general sensitivity to the mean electron density, independent of the crystalline sample structure, they can be applied to a wide range of coatings [Ren09, Yu13]. The measurements allow the monitoring of the temporal changes of the thickness, roughness and electron density of the film. Due to the high penetration depth of X-rays, the material distribution at the growth front, as well as microstructural changes in buried layers, can be observed in real time.

In situ XRR measurements during the sputter deposition with low deposition rates have been successfully performed e.g. by [Lou94, Chi97, Pev05, Lee08]. In this work, this method is applied to a hard coating material during application-relevant growth conditions, in particular dealing with high deposition rates.

The first aim of this thesis is the optimization of such *in situ* XRR experiments. Here two aspects for the optimization are addressed:

- (1) Online monitoring of the *in situ* data giving instant feedback to the operator of the coater. This includes the development of guidelines for qualitative real-time interpretation of the experimental data.
- (2) Procedures for detailed quantitative offline analysis of the recorded data, based on simulations.

As a second goal of this work, the optimized *in situ* XRR approach is applied to gain insight into the film formation of a specific material system: the monocarbides of transition metals.

As a model system for this material group, the composite material vanadium carbide (V-C) was chosen. Different films were deposited on silicon by DC sputtering, using a

V-C compound target.

In case of a compound target, the two elements, V and C, which differ significantly in mass, are sputtered simultaneously from one target. The deposition conditions might influence the element-specific angular and energetic distribution of the sputtered particles, which is well known to strongly influence the thin film formation [Bar98, Pet03]. This in turn might change the chemical composition of the film [Mra13, Nei08]. Depending on the chemical composition, V-C can form two separate phases, VC_{1-x} in cubic rock salt structure and amorphous carbon (a-C) [Stu02, EM10a, Pfl84]. This phase composition influences strongly the microstructure formation [Zha13, Ekl07, Nei08, Lia05]. Therefore in this work the microstructure formation during deposition from a compound target is investigated. Two important growth parameters, the DC power and the working gas pressure, are addressed.

In general, the applied DC power affects the number of sputtered particles as well as the nascent energetic and angular distribution at the target position [Wai78].

The working gas pressure in the chamber influences the mean free paths of the sputtered particles and in turn their motion through the gas phase [Mah06b, Aek08].

The optimized *in situ* technique was used to monitor the growth of V-C under different deposition conditions. For a comprehensive understanding of the film formation, the *in situ* results were supported by the use of complementary methods for the investigation of the chemical composition, textural changes and local variations in the microstructure.

The microstructure formation was monitored at constant deposition conditions. Here always one of the two growth parameters, DC power and working gas pressure, was kept fixed. This allowed distinguishing the influence on the film formation due to changes in the sputter process at the compound target position (DC power) and due to collisions of the different elements in the gas phase (working gas pressure).

The knowledge, how the material distribution is related to these two growth parameters at constant conditions, was then used to gain insight in the thin film formation during the more complex initial growth regime. Here, the influence of fast variations of the pressure and the power on the initial growth was investigated.

For a fundamental understanding how the *in situ* XRR data are influenced by variations in the initial microstructure formation, simulations using a 2D island growth model were performed.

The growth conditions can influence the average density of a layer. This gives the great possibility to grow a multilayer structure by the controlled variation of deposition conditions. Such metastructures can significantly enhance the mechanical properties of the coating compared to single layers [Hol90, Ulr04, Aba08b, Stu09, Kle10]. Moreover, by performing *in situ* XRR measurements during the deposition, the periodic modulation of the microstructure can be observed.

This thesis is divided into three parts:

The first part outlines the fabrication, properties and analysis methods for hard coating materials. The second part presents the details of the experimental stations, the *in situ*

sputter system, sample description, and the details of the simulations of the sputter process. In the third part, the optimization of the *in situ* experiment and the theoretical approach are outlined, followed by the results of the *in situ* measurements during the above-mentioned growth conditions.

Finally, a summary of this work and an outlook are given.

Part I

Fabrication, properties and analysis
methods for hard coating materials

1 Sputter deposition from a compound target

Physical vapor deposition (PVD) techniques as e.g. sputter deposition are common deposition techniques for polycrystalline coatings. In this work, the microstructural evolution of mono-carbides of transition metals is investigated. Vanadium Carbide films prepared by *non-reactive direct current magnetron sputtering* from a *compound target* serve as a model system.

In this chapter, the fundamental process of this sputter process is described, based on the sputter system used for this work. Further details about PVD processes can be found in [Mat98, Bun01, Dep08].

In this work, the growth of V-C films is monitored. The fundamental processes of the microstructure formation are therefore presented at the end of this chapter.

1.1 The sputter process

In the following, the sputter process is outlined. A detailed description of the sputter chamber used for this work, and the deposition conditions for the different samples, is given in Chap. 5.

Fig. 1.1 shows schematically the important features of a sputter chamber. The sputter process takes place in a vacuum chamber. In our case, a V-C compound target is mounted at the top of the chamber. The substrate is located at the bottom of the chamber.

As a first step, the sputtering gas - the inert gas Argon - is let into the chamber via a gas valve. By applying a high voltage, the Ar atoms are ionized and bombard the target.

On the back side of the target permanent magnets are positioned. Secondary electrons are generated, which are confined in the magnetic field at the target position, leading to an enhancement of the ionization process.

When the Ar^+ ions bombard the target, atoms are sputtered. Due to the confinement of the electrons in the magnetic field, a race track is generated.

The sputtered particles move through the gas phase to the substrate. In the gas phase, they undergo collisions which change their angular and energetic distribution.

Finally, the sputtered particles arrive at the substrate position, and the nucleation process takes place. The different steps of the sputter process are described in more detail in the next sections.

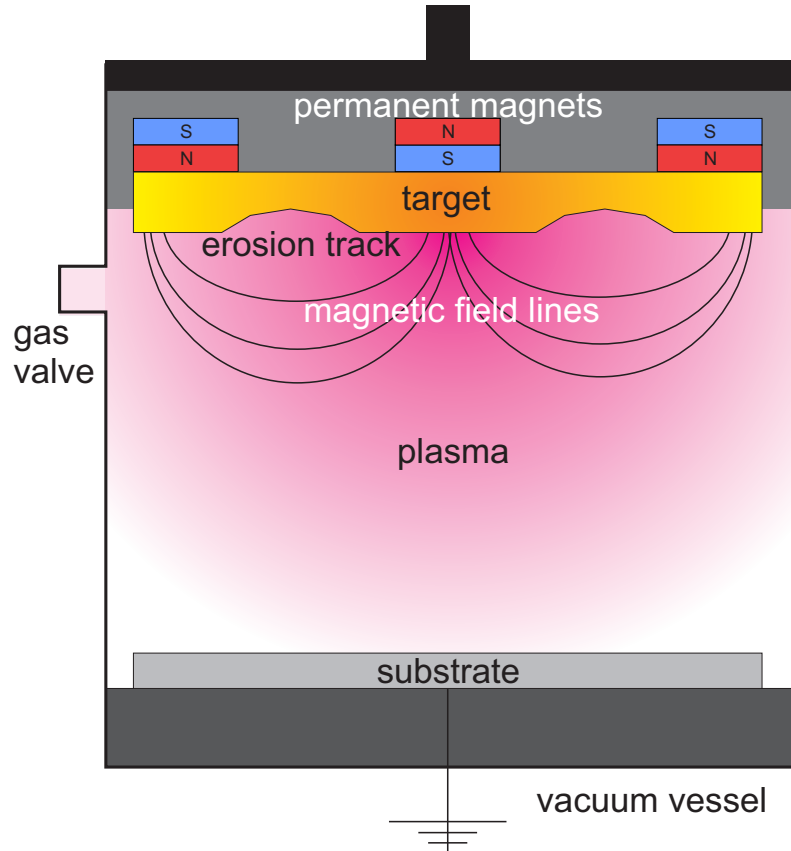


Figure 1.1: Schematic of a sputter chamber during deposition. The main components are shown.

1.1.1 Ignition of the plasma

The sputter gas is let in the chamber. In our case, a high direct-current (DC) voltage is applied between the electrodes - the target (cathode) and the grounded substrate (anode). A free electron collides with the neutral gas atom. If the energy of the free electron exceed the ionization threshold of the Ar atom at 15.7596 eV, the Ar atom is ionized by releasing an electron ($\text{Ar} + e \rightarrow \text{Ar}^+ + 2 e$).

After the collision with an Ar atom, the electron drifts to the anode. On its way to the substrate, the electron gains energy due to the high field strength, leading to further ionization of Ar atoms in case of another collision. Another electron is free now and can ionize further neutral gas atoms. An avalanche-like ionization of the gas takes place, the so called *Townsend avalanche*. This quasi neutral and partially ionized gas is called *plasma*.

Since there are only a few free electrons in the sputter chamber, a high Ar flux is needed for the plasma ignition. Besides the ionization, several other interactions occur, e.g. :

- Excitation, Relaxation and Penning ionization
If the transferred energy is too low to ionize the gas atom, it may be *excited* to a higher state ($\text{Ar} + e \rightarrow \text{Ar}^* + e$). When the system returns to the ground state (*Relaxation*), a photon is emitted ($\text{Ar}^* + e \rightarrow \text{Ar} + e + h\nu$). In case of Argon, this leads to a magenta/pink color of the plasma. Another possibility is the further ionization of a neutral gas atom via *Penning ionization* ($\text{Ar}^* + \text{Ar} \rightarrow \text{Ar} + \text{Ar}^+ + e$).
- Recombination
An ionized gas atom and an electron can recombine to a neutral Ar atom ($\text{Ar}^+ + e \rightarrow \text{Ar}$). This process is not desired during the sputter deposition, since it decreases the amount of ionized Ar atoms.

The Ar^+ drift towards the target and initializes the sputter process. The interaction of Ar^+ with the target is discussed in the next section.

1.1.2 Interaction of the plasma species with the target atoms

The Ar^+ ions from the plasma bombard the target. Several interactions can occur, as presented in Fig.1.2.

1. A collision cascade can be triggered, leading to sputtering of target atoms.
2. Secondary electrons can be generated.
3. High-energetic Ar^+ ions can be incooperated in the target as impurities.
4. For lower ion energies, the momentum of the ion can get reversed by collisions, so that the ion leaves the surface.

In the following, the processes (1.) and (2.) are described in more detail, since they are the most important for the sputter deposition process used for this work.

Sputtering of the target atoms

If the maximum energy of Ar^+ ions is high, a collision cascade is triggered between the target atoms as presented in Fig. 1.2 (1). In this process, the atoms are displaced from their lattice sites. The stopping power describes the energetic loss of the particles along their path. The stopping power is influenced by the density ρ of the target material.

Due to several collisions, some target atoms will gain a momentum transfer directed along the surface normal (indicated by green arrows in Fig. 1.2 (1)). Those atoms travel to the target surface. Only if the kinetic energy of the target atom at the target surface is higher than its surface binding energy (*SBE*), the atom leaves the target surface and is

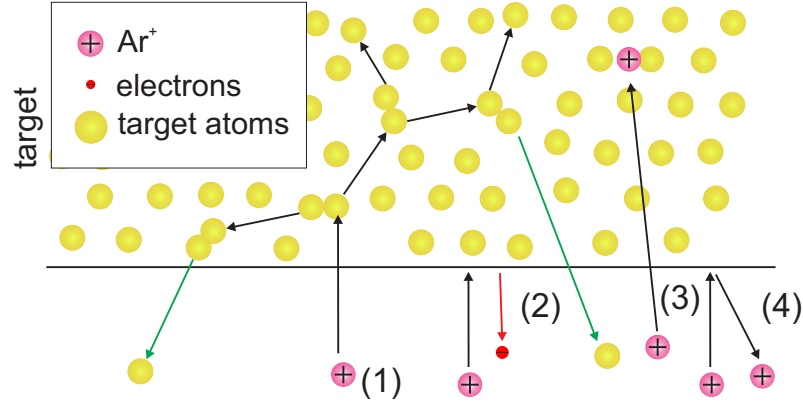


Figure 1.2: The Ar ion bombard the composite target leading to a sputtering of target atoms. For more details s. text.

sputtered.

The number of sputtered particles per incident ion is defined as the *sputtering yield* Y . Due to the collisions in the target, the sputtered particles leave the target in a cosine-close distribution, which can be described in good approximation by

$$\frac{d^2Y}{d^2\Omega} = \sum_{i=1}^5 c_i \cos_i(\theta), \quad (1.1)$$

where θ is the polar emission angle. c_i are fitting parameters with $\sum_{i=1}^5 c_i < 1$. $\frac{d^2Y}{d^2\Omega}$ is called the *nascent* angular distribution in the following chapters.

As stated above, a V-C *composite* target is used for the preparation of the thin films. Hence, V and C atoms are sputtered from the target simultaneously [Adj95, Lia04, Lia05].

For single element targets, a higher DC current leads to a higher flux of Ar^+ ions, an increase in the applied DC voltage increases the energy of the impinging Ar^+ ions [Wai78]. Changes in the nascent angular and energetic distribution can occur when changing the applied DC Power.

C and V vary significantly in their mass (12 amu and 51 amu). Furthermore, they have different *SBEs*. Values for the *SBEs* are known for only few materials. However, the heat of sublimation is commonly used as *SBE*. Assuming single element targets, values of the *SBE* for V of 5.33 eV and for C of 7.41 eV are reported in literature [Moe88, Sri14]. For compound targets, usually the values for the *SBE* and ρ are approximated by a linear combination of the individual *SBEs* weighted to their fraction in the target [Moe88, Nei08, Mra13]

The influence of the DC Power on the sputter process from a V-C compound target will

be discussed in chapter 9.

Generation of Race Track

During the Ar^+ ions bombardment which leads to the sputtering of the target atoms (s. Fig 1.2), additionally secondary electrons are generated (2). These electrons are trapped in the magnetic field created by permanent magnets, which are mounted on the backside of the target. This leads to a higher ionization process of the Ar atoms close to the target surface. As a result, the high Ar flow, needed for the plasma ignition, can be reduced.

Due to the confinement of the plasma close to the target, an *erosion track* or *racetrack* on the target surface is generated. The race rack of the target (s. Fig. 1.3) can be approximated by a Gauss function. It describes the probability at which distance x from the center of the target a particle is sputtered [Mah06a]:

$$R(x) = \frac{1}{\sigma_G \sqrt{2\pi}} e^{-\frac{(x-\mu_G)^2}{2\sigma_G^2}}, \quad (1.2)$$

μ_G corresponds to the distance between the center of the target and the center of the racetrack. σ_G is estimated form the visible width w of the erosion track assuming $\frac{w}{2} = 3\sigma_G$. The race track is important since sputtering of target atoms is mostly restricted to this area. A broader racetrack, e.g., allows the removal of more target atoms than a narrow race track.

1.1.3 Motion of the target atoms through the gas phase

The sputtered atoms travel through the gas phase towards the substrate. In the gas phase, they collide mostly with the gas atoms. Collisions with ions and electrons as well as multi-atomic particles can be neglected, since the concentration of these species is negligibly small compared to the concentration of the gas atoms (ratio in the order of 10^{-3})[Aek08].

The mean free path λ of a target atom is determined by

$$\lambda = \frac{k_B T}{p \sigma_{ccs}}, \quad (1.3)$$

where k_B is the Boltzmann constant, T the temperature, p the pressure of the gas, and σ_{ccs} is the collision cross section.

The collision cross section can be calculated via kinetic gas theory in the hard sphere approximation. Here the sputtering gas is assumed to be a Maxwellian gas. From this

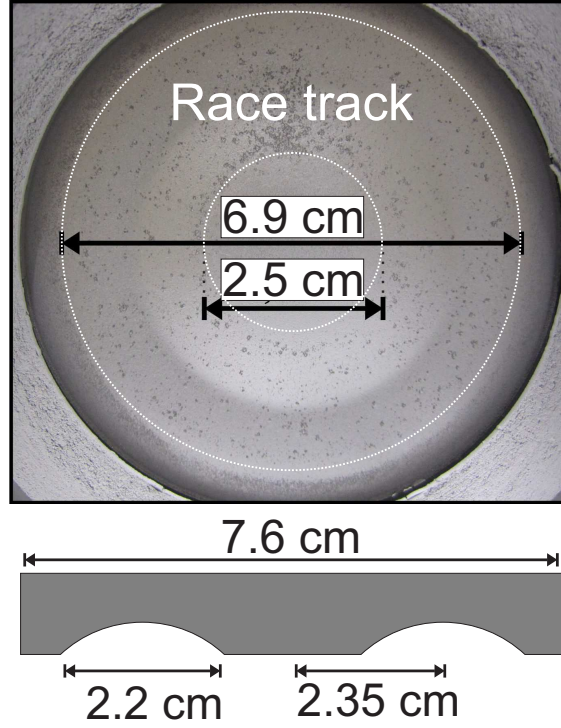


Figure 1.3: Image of the V-C target. The racetrack is indicated by circles.

assumption it follows:

$$\sigma_{ccs} = \pi(r_s + r_g)^2 \sqrt{1 + \frac{m_s}{m_g}}, \quad (1.4)$$

where r_s, r_g are the radii and m_s, m_g the masses of the sputtered and the gas atom, respectively.

In the previous case, σ_{ccs} was assumed to be constant in time and space. In reality, σ_{ccs} depends on the nascent average energy of the sputtered particle E_{sp} . According to the empirical study of [Rob79], for $E_{sp} > 1\text{eV}$, the energy-dependent mean free path $\lambda(E_{sp})$ can be estimated by:

$$\lambda(E_{sp}) = \frac{k_B T}{p \sigma_{ccs}} E_{sp}^{0.29}. \quad (1.5)$$

Using $\lambda(E_{sp})$, the number n of collisions of the sputtered particle with Ar^+ ions is given

by

$$n = \frac{d_{TS}}{\lambda(E_{sp})}, \quad (1.6)$$

where d_{TS} is the target-substrate distance.

When the sputtered particles undergo collisions with the gas atoms, they lose energy. The final energy E_{final} of a sputtered particle is determined in the hard sphere approximation via:

$$E_{final} = (E_{sp} - k_B T) \exp(n \ln(E_f/E_i)) + k_B T, \quad (1.7)$$

where the ratio of the energy before and after a single collision of the sputtered particle with an Ar atom is given by

$$E_f/E_i = 1 - \frac{2 (m_s/m_g)}{(1 + m_s/m_g)^2} \quad (1.8)$$

Furthermore, the collisions lead to a change in the angular distribution of the sputtered particles. Using classical scattering theory and assuming a spherically symmetric interaction potential $V(r)$, the polar scattering angle θ_{com} in the center of mass system using classical scattering theory is given by [Aek08]:

$$\theta_{com}(E_{com}, p) = \pi - 2 b \int_R^\infty \frac{1}{r^2 g(r)} dr, \quad (1.9)$$

with

$$g(r) = \sqrt{1 - \frac{V(r)}{E_{com}} - \frac{b^2}{r^2}}, \quad (1.10)$$

where E_{com} is the kinetic energy of the sputtered particle in the center of mass system, b is the impact parameter. R is the largest value for which $g(R) = 0$.

The impact parameter b is defined between 0 and b_{max} . b_{max} is the maximum impact parameter for the minimum deflection at Θ_{min} . Θ_{min} is an arbitrary value, usually between 0.2 and 2 °.

The collisions in the gas phase influence the deposition rate. The Keller-Simmons formula expresses the dependence between pressure and deposition rate, as well as the target-to-substrate distance d_{TS} [Die05, Alv14]:

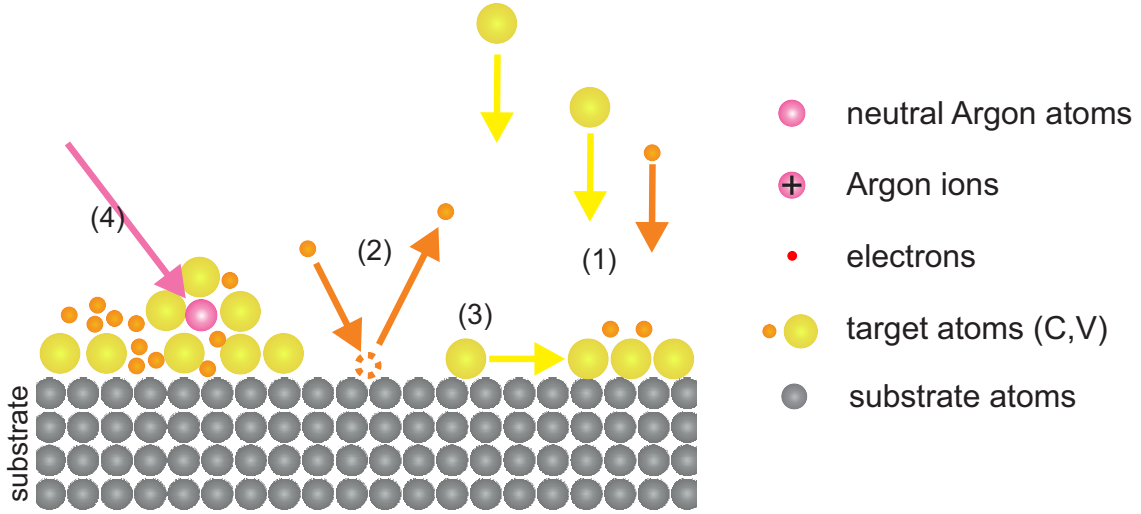


Figure 1.4: The sputtered particles drift to the substrate and diffuse. For more details s. text.

$$F_{KS}(p) = F_0 \cdot \frac{\lambda(E_{sp},p)}{d_{TS}} \left(1 - \exp\left(-\frac{d_{TS}}{\lambda(E_{sp},p)}\right) \right), \quad (1.11)$$

where F_0 is the deposition rate at the target position.

As already mentioned above, C and V vary significantly in their mass. This influences the sputtering process at the target position, as described in Sec. 1.1.2.

In addition, this significant difference in mass will additionally influence the behavior of the single elements during their transport through the gas phase. Both materials have different collision cross sections. Depending on the working gas pressure, element-specific variations in the angular and energetic distribution of the sputtered atoms might occur. This might lead to variations in the chemical composition. Changes of the film formation due to the working gas pressure will be discussed in chapter 10.

1.1.4 Interaction of plasma species and the substrate

The sputtered particles imping on the substrate with a certain impingement rate. Their energetic and angular distribution is determined by the sputtering at the target position and their collision in the gas phase as described in Sec. 1.1.3.

In Fig. 1.4 the important processes are illustrated: The sputtered atoms can be (1) ad-

sorbed or (2) reflected from the substrate. On the surface, the atoms can (3) diffuse or (4) re-evaporate (desorption). (4) High energetic Ar atoms can be implemented in the surface, leading to defects in the film.

Those processes will influence the film formation of the polycrystalline coatings as described in the next section.

1.2 Thin film formation

Thin films exhibit a wide variety of microstructures characterized in terms of grain size and crystallographic orientation, lattice defects, phase composition, and their surface morphology.

Typically thin films are deposited at growth temperatures well below the melting point. Hence, the thin film growth takes place under non-equilibrium conditions, far way from the thermodynamic equilibrium.

In this work, the film formation of Vanadium carbide is monitored. The interaction of 2 elements in the material system influence the film formation. In this section, as a first step, basic aspects of the film growth during sputter deposition are described. The strong influence of the C content in the film on the microstructure and morphology will be discussed in more detail in Chap. 2. For more details we refer to [Mat98, Tho00, Pet03, Iba06, Lüt10].

The thin film formation proceeds in the following steps, which are schematically shown in Fig. 1.5: nucleation, island growth, impingement, coalescence and formation of the islands, and the development of a continuous structure, and film growth. The adsorbed particles diffuse along the surface. The diffusion can be described by the diffusion equation

$$\vec{j} = D \nabla \rho, \quad (1.12)$$

where D is the diffusion coefficient. The diffusion equation relates the adatom current \vec{j} with the diffusion current, given by the gradient of the adatom density.

The diffusion length L_{diff} is related to D via

$$L_{diff} = \sqrt{D \tau_{ad}} \approx \sqrt{\frac{D}{F_I}}, \quad (1.13)$$

where τ_{ad} is the time, an adatom has to diffuse. This time is inversely proportional to the impingement rate F_I . A higher flux hence leads to a reduction of the diffusion length. Clusters are formed, which grow either due to binding of diffusing atoms or by direct impingement of other atoms. These clusters are called nuclei [Tho00].

This very first stage is called *primary nucleation*.

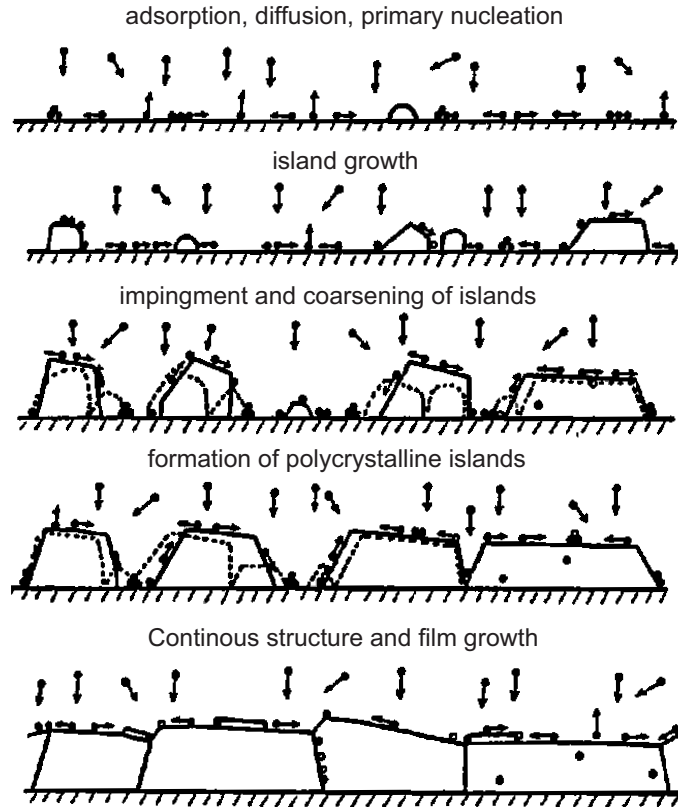


Figure 1.5: Scheme, showing the several stages of microstructural evolution. Adapted from [Pet03].

Secondary nucleation takes place, if during the growth and coalescence of the islands, the coverage of the substrate decreases. Uncovered regions on the substrate exist, where again atoms can form nuclei.

Repeated or re-nucleation processes can occur e.g. if the growth of an island is blocked due to impurities.

In the simplest case, the nuclei are randomly oriented [Pet03]. They grow in size due to diffusion of other atoms or by impingement of sputtered atoms. A crystal is formed. Its orientation in the simplest case is defined by the orientation of the nuclei. If crystallites touch, they coalesce. Coarsening processes can occur due to differences in the average energy of the atoms in two neighboring islands [Bar98]. The atoms can detach from or attach to islands. Moreover, atoms can move from one island to another due to diffusion.

Due to Ostwald ripening - a large island can increase in size by the diffusion of atoms from a smaller island. In this process, the covered fraction of the substrate decreases.

The generated voids might be filled by newly arriving particles (*Secondary nucleation*). Often in the case of sputter deposition, the diffusion is limited. The further growth is influenced by shadowing effects and competitive grain growth.

Shadowing effects occur when condensation at one side of a free-standing column is enhanced in expense to hidden areas [Pet03]. This leads to the growth of porous coating structures.

For two crystals with different orientation according to the types of their growing faces, competitive grain growth occurs. In this case, the crystal, which grows faster, will overgrow the slower growing crystals. This usually leads to the growth of strongly textured V-shaped columns. This competition ends, if all crystallites exhibit the same orientation.

Impurity species can be adsorbed, segregated or dissolved in the crystal structure [Bar98].

They either inhibit or promote the above-mentioned structure formation as grain growth, and texture development. The influence of the impurity strongly depends on the chemical interaction of the metal and the impurity.

If the surface is completely covered, constant re-nucleation takes place. In this case, the thick film consists of two phases - crystals, which are overgrown by layers of an impurity phase. The impurity phase inhibits the grain boundary migration. This can lead to a decrease in the grain size and a suppression of a strong texture. However, the influence of the impurities on the thin film formation strongly depends on the amount of the impurities.

1.3 Summary

In this chapter, the fundamental processes of DC Sputtering from a compound target was outlined. The target contains out of the two elements V and C, which differ significantly in their properties, e.g. mass.

This can influence -element-specific- the angular and energetic distribution of the particles, which arrive on the substrate.

The microstructure formation is dominated by the non-equilibrium conditions during sputtering process. This influences the thin film formation for single element films. In this work, the emphasis lies in monocarbides of transition metals. Hence, the growth process involves 2 elements. Their properties and variations in the microstructure due to different chemical composition are presented in the next chapter.

2 Hard coating materials

Hard coatings are nowadays commonly used for tools, artificial medical implants and many other components to improve their duration of life.

Mono-carbides of transition metals form a major group of these materials. In general they are complex material systems, however among themselves they have similar properties. The main emphasis of this work lies on the investigation of Vanadium Carbide thin films, which serve as a model system for monocarbides of transition metals.

In the following, the main properties of this material group are presented.

2.1 Hard materials: monocarbides of transition metals

Hard coatings usually exhibit a hardness higher than 20 GPa. Diamond, for comparison, can exhibit hardness between to 70-150 GPa [Iri03]. However, for most of the applications, the desired properties -besides high hardness - are a good adhesion to the (metallic) substrate, good toughness, and a low friction coefficient [Tot71, Rei09, Bun01].

Two important groups of the hard materials are [Sch07]:

- *metallic* hard materials: Bonding of one or more transition metals of the group IVA to VIIa to the elements C,N,B,Si, and sometimes P,S and O.
- *nonmetallic* hard material: Covalent bonding of different elements as B,C,N,S to each other. Moreover, hard coating materials as AlN and SiC are belonging to this group. The most famous hard material of this type is diamond.

In this work, we focus on carbides of transition metals (TM-Cs) including, e.g., Ti-C, V-C or Ta-C.

TM-Cs have a good adhesion to metallic substrates since their dominant chemical bonding is metallic. The C content in the film leads to low-friction coatings. Therefore, they are used for wear-resistant protective coatings of cutting tools, tribological applications and abrasion-resistant layers on optical components [Aba08a, Jan13].

TM-Cs are similar in their properties amongst each other due to the comparable size of the atoms, the electronic structure and the electronegativity of C [Tot71, Rei09, Bun01]. Table 2.1 summarizes some of the important properties of the TM-Cs of group IV and V. All TM-Cs have a high hardness above 20 GPa. Due to their very high melting point around 3000 °C, they are often called *refractory carbides*. They are usually metallic in they electrical, optical and magnetic properties. The properties are usually comparable

	Melting Temperature	Microhardness	Structure	Lattice Parameter	X-ray density
	[°C]	[GPa]		[Å ⁻¹]	[g/cm ³]
Group IV					
TiC	3067	28.44	Rocksalt	4,328	4,91
ZrC	3420	25.50	Rocksalt	4,698	6,59
HfC	3928	26.48	Rocksalt	4,166	12.67
Group V					
VC	2830	28.44	Rocksalt	4,140	5.77
NbC	3600	23.54	Rocksalt	4,240	7.79
TaC	3950	24.52	Rocksalt	4,577	14.5

Table 2.1: Properties of monocarbides of Group IVA and VA - transition metals after [Tot71, Pie96, GES14, ICS14]

to the pure transition metals[Aba08a]. Furthermore, they are chemically stable at room temperature.

However, the here presented values depend on the investigated films. Variations in the microstructure due to different deposition conditions were reported by e.g. [Lia05, Aba08a, Teg09]. Due to the non-equilibrium conditions of the sputter process, the microstructure of the coating can be drastically influenced by the deposition conditions. The microstructure of TM-C depends strongly on the C content in the film as shown in the next section.

2.2 Influence of the chemical composition

Fig. 2.1 (a) shows schematically the binary phase diagram of TM-Cs. The TMs usually crystallize in bcc or hcp structure. In the TM-Cs, the carbon atoms occupy the interstitial position, forming a NaCl-Rocksalt structure with slightly increased lattice parameters (s. Fig. 2.1 (b)).

According to [Häg31], those interstitial compounds are stable if the ratio between the radius of the metal (r_{TM}) and the carbide (r_C) is within $0.43 < r_{TM}/r_C < 0.59$, which is fulfilled for all TM-Cs of Group IV and Group V.

However, it is very rare that the C atoms fill all octahedral sides in the unit cell. The occupation of the interstitial position is given only by certain probability $p = 1 - x$.

For very low C content, the occupation of the interstitial positions is strongly reduced and the carbide structure is less stable. Carbon vacancies can lead to the formation of superstructures with vacancy ordering ,e.g., Nb₆C₅ or V₈C₇. Additionally, due to stacking faults, defects structures are observed, e.g., Ta₄C₃ [Lip05, Jan13].

With increasing C content (usually between 35-49 at.%), a thermodynamical stable structure evolves. For even higher content of C in the TM-C coating, phase separation

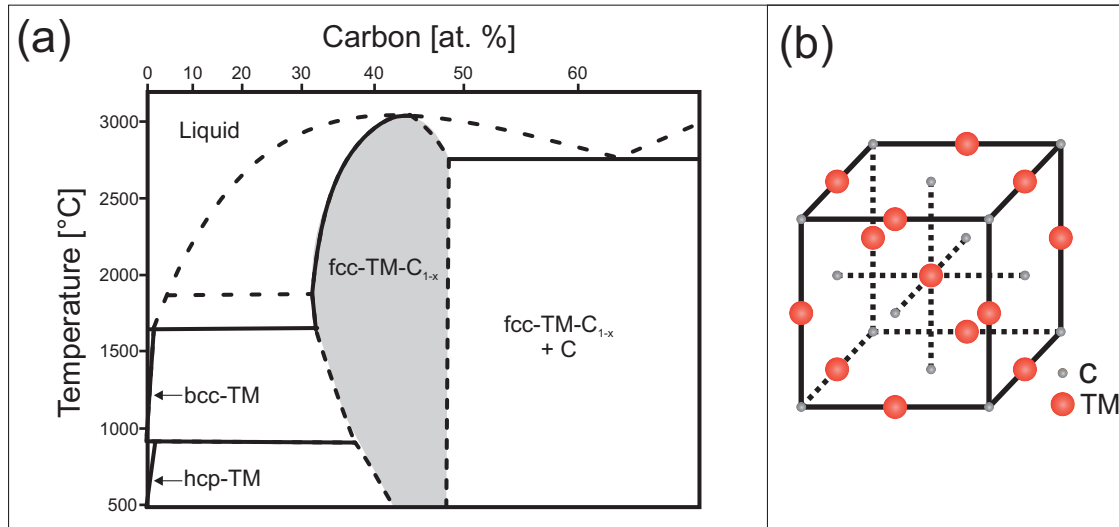


Figure 2.1: (a) Schematic binary phase diagram of TM-C (adapted from [Mur87],[Jan13]),(b) Rocksalt structure. The non-metal sublattice sites are only randomly occupied.

occurs. Besides the rocksalt structure (TM-C_{1-x}) amorphous C (a-C) is coexisting [Stu02, EM10a, Pfi84].

In this work, the presented VC_{1-x} films exhibit C contents above 37 at.% (s. Chap. 10). This value corresponds to the lower range for thermodynamical stable structures in NaCl structure. The maximum occupation of interstitial position of C has been found for VC_{0.92} at C=48 at.% for equilibrium structure [Lip05]. For higher C content, the above-mentioned phase separation occurs.

The chemical composition influences the microstructure evolution. [Sun10], [Lip05]. Fig. 2.2 shows schematically the evolution of the coating structure with increasing C content. With higher amount of C the grain size decreases. The grains have the typical NaCl-structure, while a-C is located at the grain boundaries. With even higher C content, the coating structure resolves in nanoclusters, which are embedded in a a-C cluster.

This is in good agreement with the experimental findings reported in literature.

[MM09] investigated the influence of the C content in Ti-C. The films were deposited using two single targets of Ti and C. The C content was changed by variation of the applied power of the targets. The chemical composition was determined using electron energy loss spectroscopy. The microstructure was investigated by TEM, SEM and ED. For low C content < 5 % atm., single-phase TiC was found. With increasing C content, the grain size is reduced. The amount of the amorphous phase increases. At high C content, the grain size is strongly reduced size. The grains are embedded in an amorphous C matrix. They state, that C hinders the grain growth.

[Ned11] investigated the NbC system. The films were prepared by dual DC magnetron

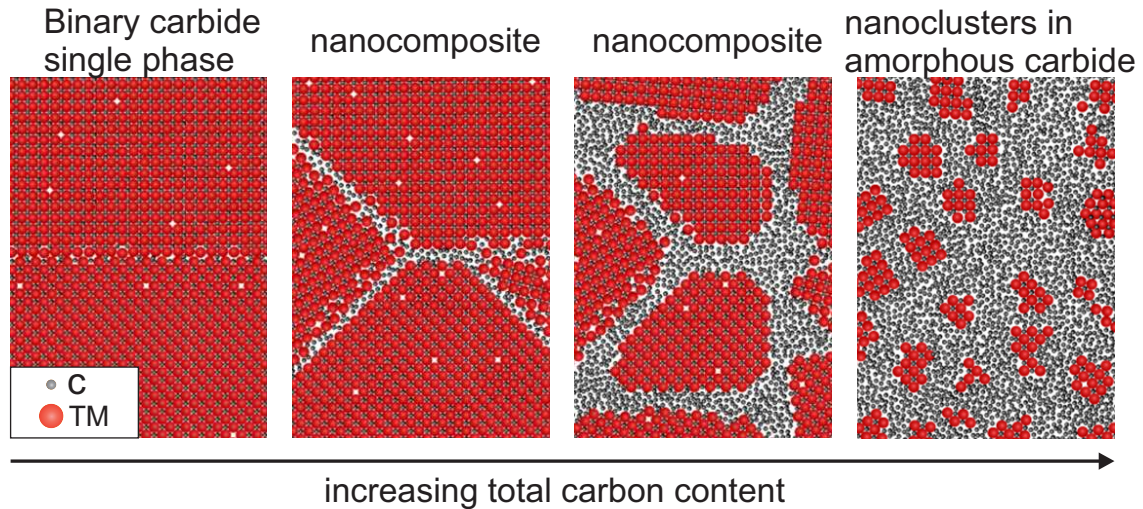


Figure 2.2: Schematic of the evolution of the microstructure depending on the C content, adapted from [Jan13].

sputtering. The carbon content from 43 to 64 at.% was achieved by changing the applied power. The chemical composition was determined by XPS measurements. The TEM images showed small crystallites which are embedded in a amorphous C matrix. With increasing C content, the grain size decreases due to the hindering of the grain growth. [Sam12] investigated the influence of C content in Ti-C systems. The films were prepared by reactive sputtering from a metal Ti target. The composition was determined by X-ray photoelectron spectroscopy. X-ray diffraction measurements showed an decrease in grain size with increasing C content. The identified three groups depending on the C content: nanocomposite Ti/TiC, nanocrystalline TiC and embedded TiC grains in an amorphous matrix.

The evolution of the microstructure depending on the C content is in good agreement with the phase diagram. The changes in the microstructure are driven by the coexisting phase. The decrease in grain size in case of higher C content is due to the agglomeration of C at the grain boundaries, which hinders the grain growth during the deposition [Stu02, MM09, Sam12, EM10a].

Deposition conditions can change the C content in the film and hence lead to composition-induced changes of the microstructure. This will be discussed further in Chap. 10. By the controlled change of the growth parameters it might be possible grow a multilayer system of layers with different microstructure. Properties of multilayer systems are presented in the next section.

2.3 Multilayer coatings

One approach to enhance the properties of a coating is the fabrication of multilayer systems [Hol90, Ulr04, Abo08b, Kle10, Stu09]. Those systems are usually grown by alternating layers of two materials combining their attractive properties. Multilayer systems can provide barriers for dislocation motion, which increases the hardness and toughness of the coating.

Successful hard coating multilayers have been reported in literature (s. Review [Stu09]). A strong enhancement in hardness was found for several systems e.g. for Ti-N/V-N, Ti-C/V-C and Ti-C/Nb-C superlattices. However, it is reported that the improvement of the single properties as hardness or toughness strongly depends on the individual layer thickness.

Besides the variation of the chemical component of the bilayer, multiphase crystalline/amorphous layer have been produced e.g. in Ti-S-N systems. Here the amorphous layer is introduced to block the columnar growth of the crystalline layer. This is a desired process, since the grain boundaries of the columns can lead to cracks and hence to a failure of the multilayer structure.

The growth process of a multilayer system is more complex compared to a single layer due to the optimization of the deposition process of two different materials. Multilayer growth of hard coating is often successful for laboratory deposition systems, but fails in case of larger production for industrial use [Stu09].

Therefore, it is desirable to reduce the complexity of the deposition process of such systems.

As stated above, the microstructure of TM-C depends on the chemical composition and can be influenced by the growth conditions. Hence it might be possible to achieve the fabrication of multilayer systems using one compound target.

[Bul96] tried to achieve such a multilayer system by the variation of the applied bias during the sputtering of Ti-N. An improvement of the properties was realized, however the multilayer structure could not be resolved by SEM and XRR. The same result was found by [Yoo96], who alternated the growth temperature during deposition of a-Si:H. However, in this work, the multilayer structure was not confirmed by TEM or XRR.

A more promising approach was reported by [Li11]. A multilayer structure was grown by alternating the bias during the sputter process in a diamond-like carbon system. They exploited, that structural changes occur, since the alternation of the bias changed the bonding of C ($1sp_2$ (Soft Carbon), $1sp_3$ (Hard Carbon)).

As a last example, the result of [Lai11] is presented. In this work a confirmed multistructure was produced by the use of two different deposition techniques in one chamber. Here a C/C multilayer system was grown by sequentially changing the deposition technique (radio-frequency sputter deposition and plasma assisted chemical vapor deposition).

In chapter 13 the growth of a V-C/V-C multilayer systems by the controlled variation of the gas pressure will be presented.

2.4 Summary

In this chapter, the main properties of monocarbides of transition metals were outlined. TM-Cs are complex material systems. However, among themselves they have similar properties. Their mechanical properties strongly depend on the chemical composition, which influences - beside the deposition conditions - the coating structure.

Since a similar growth behavior is expected for all TM-C, as model system, the thin film formation of vanadium carbide (VC_{1-x}) is investigated. Due to its hardness at high temperatures, it is a promising material system for future tribological and engineering applications. For high C content, phase separation in VC_{1-x} and a-C can occur. An enhancement of C in the film leads to the hindering of the grain growth. The coating structure is hence not only influenced by changes in the energetic and angular distribution (s. Chap. 1.2), but also driven by variations in the chemical composition. Those composition-induced changes in the microstructure give the opportunity to grow multi-layer systems using only one material (s. Chap. 13).

3 X-ray reflectivity (XRR)

Hard coatings such as VC_{1-x} can have various coating structures as shown in chapter 2. X-ray Reflectivity (XRR) measurements are independent of the crystalline structure and can be applied to almost any coating [Ren09, Yu13]. They are used for the investigation of the thickness, roughness and mean electron density of films.

In this chapter, the fundamentals of specular XRR after growth are presented, which serve as a basis for the calculation of the *in situ* XRR in Chap. 8. The typical features of such curves are presented. Interfacial roughness leads to diffuse scattering. The basics of diffuse scattering are outlined. The temporal changes in the diffuse scattering during the growth are presented in Chap. 13. Further details about standard XRR measurements can be found in [AN11, Lek87, Pie04, Tol99].

3.1 Scattering of X-rays

X-rays are electromagnetic waves with wavelengths in the range of 0.01 to 10 nm. This corresponds to frequencies in the range 30 PHz to 30 EHz and energies in the range 100 eV to 100 keV.

In vacuum, a electromagnetic plane wave is given by its electric field vector $\vec{E}(\vec{r})$

$$\vec{E}(\vec{r}) = \vec{E}_0 \exp(i\vec{k}\vec{r}) \quad (3.1)$$

where \vec{E}_0 is the amplitude of the electromagnetic field and \vec{k} is the wave vector, with $k = \frac{2\pi}{\lambda}$. λ is the wavelength of the electromagnetic wave.

If the X-rays penetrate a medium, the wave propagates according to the Helmholtz Equation

$$[\Delta + k^2(\vec{r})] \vec{E}(\vec{r}) = V(\vec{r}) \vec{E}(\vec{r}). \quad (3.2)$$

The potential $V(\vec{r})$, interacting with the electromagnetic wave, can be described by the

refractive index $n(\vec{r})$ of the medium. The Helmholtz Equation is then given by

$$\Delta \vec{E}(\vec{r}) + k^2 n^2(\vec{r}) \vec{E}(\vec{r}) = 0. \quad (3.3)$$

Here only the propagation of the electric field is considered, since the magnetizing field \vec{H} has only a considerable influence in case of polarized X-ray radiation (in case of magnetic materials).

The refractive index for N atoms, assuming to be harmonic oscillators with a resonant frequency ω_i , in a unit volume is expressed as

$$n^2(\vec{r}) = 1 + N \frac{e}{\epsilon_0 m} \sum_{i=1}^N \frac{f_i}{\omega_i^2 - \omega^2 - 2i\omega \eta_i}, \quad (3.4)$$

where ω is the frequency of the incoming wave, e the charge and m the mass of the electron, η_i are damping factors, f_i is the atomic form factor. f_i are in general complex and depend on the wavelength of the incoming wave:

$$f_i(\lambda) = f_i^0 + f_i'(\lambda) + f_i''(\lambda). \quad (3.5)$$

where $f_i'(\lambda)$ and $f_i''(\lambda)$ account for correction due to dispersion and absorption. f_i^0 can be approximated by the number Z_i of the electrons of an atom in the unit volume. The frequency ω of the X-rays is larger than the resonant frequency of the atoms ω_i , therefore Eqn. 3.4 is usually written as

$$n(\vec{r}) = 1 - \delta(\vec{r}) + i \beta(\vec{r}). \quad (3.6)$$

The dispersion $\delta(\vec{r})$ and the absorption $\beta(\vec{r})$ are given by:

$$\delta(\vec{r}) = \frac{\lambda^2}{2\pi} \rho_e r_e \sum_{i=1}^N \frac{f_i^0 + f_i'(\lambda)}{Z} \quad (3.7)$$

$$\beta(\vec{r}) = \frac{\lambda^2}{2\pi} \rho_e r_e \sum_{i=1}^N \frac{f_i''(\lambda)}{Z} = \frac{\lambda}{4\pi} \mu(\vec{r}) \quad (3.8)$$

where r_e is the classical electron radius, ρ_e the electron density of the film and $\mu(\vec{r})$ is the linear absorption coefficient.

In case of a homogenous medium and far away from absorption edges, Eqn. 3.7 simplifies to

$$n = 1 - \delta + i \beta = 1 - \frac{2\pi\rho_e r_e}{k^2} + i \frac{\mu}{2k}. \quad (3.9)$$

In the X-ray regime, δ is always positive and in the order of 10^{-6} . As a result, the refractive index n is always slightly smaller than 1. β is usually 2 orders of magnitude smaller.

3.2 Specular X-ray reflectivity

In case of specular X-ray reflectivity, the angle α_i of the incoming wave and the angle α_f of the reflected beam are kept equal with respect to the the surface of the interface (s. Fig. 3.1).

In this case, the momentum transfer \vec{q} is directed perpendicular to the surface (here denoted as z -direction). The z -component of \vec{q} is given by:

$$q_z = 2|\vec{k}_i| n \sin(\alpha_i). \quad (3.10)$$

A part of the incoming X-ray (\vec{k}_i^z) is reflected from the interface (\vec{k}_r^z), while another part is transmitted (\vec{k}_t^z). The z -components of the wavevectors of the incoming, reflected and transmitted X-ray beam, $\vec{k}_{i,f,t}^z$, are related to the angles via

$$k_{i,f,t}^z = |\vec{k}_i| n \sin(\alpha_{i,f,t}). \quad (3.11)$$

The relation between the amplitudes $r = \vec{E}_f \cdot \vec{E}_i$ for reflection and $t = \vec{E}_t \cdot \vec{E}_i$ for transmission are described by the Fresnel coefficients. For s-polarization, r and t are calculated using the continuity of the tangential components of the electrical field of the plane waves at the interface:

$$\begin{aligned} r &= \frac{k_i^z - k_t^z}{k_i^z + k_t^z} \\ t &= \frac{2k_i^z}{k_i^z + k_t^z} \end{aligned} \quad (3.12)$$

The reflectance R and the transmission T of the impinging plane wave are given by

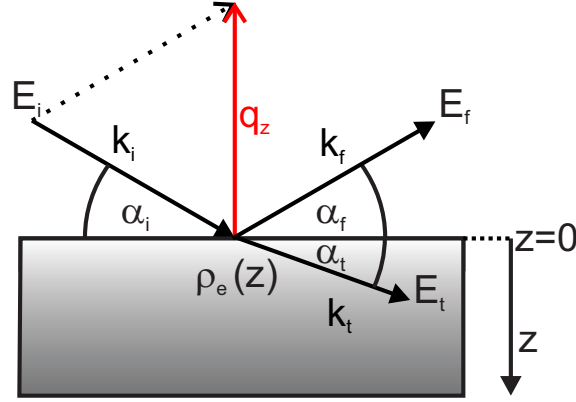


Figure 3.1: Scheme of the X-ray reflectivity geometry, showing the notation used in the text.

$$\begin{aligned} R(\alpha) &= |r(\alpha)|^2 \\ T(\alpha) &= |t(\alpha)|^2 |k^z(\alpha)/k^z(\alpha)| \end{aligned} \quad (3.13)$$

Eqn. 3.13 can be applied for scattering at one interface. For systems with more layers, the scattering process at each individual layer has to be calculated.

For this calculation, the Parratt-Algorithm can be used [Par54]. It is a recursive algorithm, which calculates the ratio of the amplitudes of the reflected and transmitted partial waves in each layer. This algorithm is used in this work and extended to growing films. It will be described in more detail in Chap. 8.

For a typical measurement of the specular XRR, the angles α_i and α_f are changed, keeping the relation $\alpha_i = \alpha_f$.

In the following, typical features of such an XRR curve are presented.

3.3 Characteristic features of the specular XRR curve

Three characteristic features of an XRR curve, namely the critical angle, intensity oscillations and the slope, provide information about the properties of the thin film. They are described in the following using the one layer system of a V-C film on a silicon substrate.

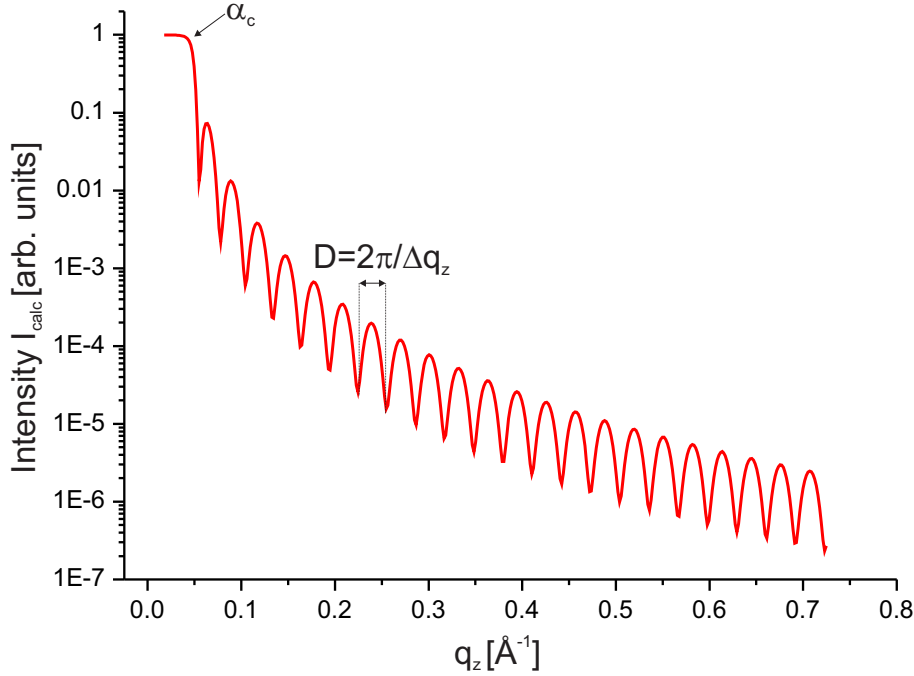


Figure 3.2: Simulated XRR curve of a 20 nm thick V-C film on Silicon substrate.

3.3.1 The critical angle

Fig. 3.2 shows the specular XRR curve simulated for a V-C film on a silicon substrate. For small q_z , the normalized intensity is one. The intensity decreases only when the scanning angle is larger than the critical angle α_c .

Snell's law describes the relation between the incidence, exit angle, and refraction, if light passes through a boundary of two media.

If one media is vacuum ($n_{vacuum} = 1$), the Snells law reduces to

$$\cos(\alpha_i) = n \cos(\alpha_t). \quad (3.14)$$

α_i , the incidence angle, and α_t , the angle of refraction, are defined in respect to the boundary.

Since $n < 1$ in the X-ray regime for any material, *Total External Reflection* (TER) occurs if the incidence angle α_i is smaller than the *critical angle* α_{crit} . At α_{crit} , the X-ray beam is not reflected and the refracted beam propagates parallel to the surface of the interface.

Since $\alpha_t = 0$, and α_c is usually small ($< 1^\circ$),

$$\cos(\alpha_{crit}) \approx 1 - \frac{\alpha_{crit}^2}{2} \approx n \quad (3.15)$$

Neglecting absorption ($\beta = 0$), α_c can be estimated in good approximation by

$$\alpha_{crit} = \sqrt{2\delta}. \quad (3.16)$$

α_{crit} is directly related to the mean electron density ρ_e , since $\delta \propto \rho_e$ (s. Eqns. 3.7 and 3.9).

3.3.2 Kiessig fringes

For system with several interfaces, the reflected intensity is characterized due to interference effects occur due to different refractive indices.

This leads to a optical path difference Δ of the X-rays, reflected at the surface of the individual layers [Kie31].

In case of two interfaces, maxima are found for

$$\Delta = (m + \frac{1}{2})\lambda, \quad (3.17)$$

while minima are found for

$$\Delta = m\lambda \quad m = 0,1,2,\dots \quad (3.18)$$

For $\alpha_i > \alpha_{crit}$, oscillations, the *Kiessig Fringes*, arise (Fig. 3.2). For maximum positions at α_1 and α_2 , the following relation is found:

$$\Delta = 2 D [\sin(\alpha_2) - \sin(\alpha_1)] = \lambda \leftrightarrow D = \frac{\lambda}{2 [\sin(\alpha_2) - \sin(\alpha_1)]} = \frac{2\pi}{\Delta q_z}. \quad (3.19)$$

Hence the film thickness D is related to the period of the Kiessig fringes Δq_z .

3.3.3 Influence of roughness

In reality, all layers exhibit height fluctuations $\tilde{z}(x,y)$ around their mean height $\langle z(x,y) \rangle$ at the point $\vec{r} = (x,y)$, as schematically shown in Fig. 3.3 (a).

The roughness σ of the film can be described by the root-mean-square roughness, which

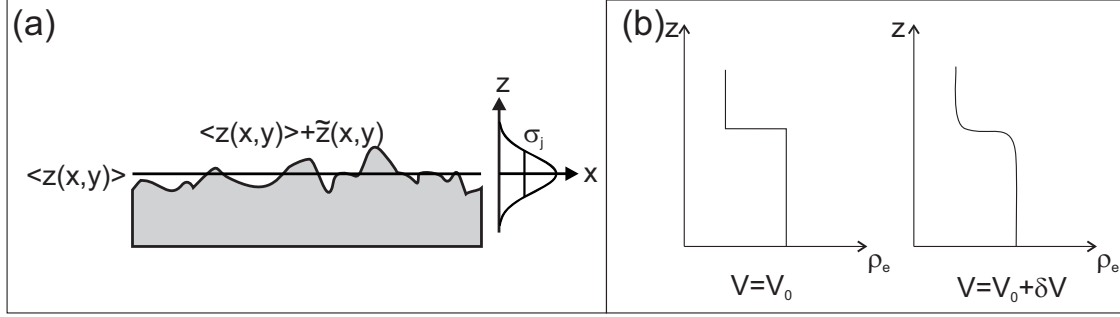


Figure 3.3: (a) Scheme of a rough film. Here the fluctuations around the mean height can be described by a Gaussian distribution. (b) Development of the potential V for the unperturbed (left) and perturbed (right) case. The potential V is proportional to the mean electron density ρ . z is oriented normal to the surface of the interface.

is defined by

$$\sigma(t) = \sqrt{\langle (z(x,y) - \langle z(x,y) \rangle)^2 \rangle} \quad (3.20)$$

The fluctuations around the mean height can be often described by a Gaussian distribution. In this case, the transition of two layers can be approximated using a *tanh*- or *erf*-profile [Tol99].

In case of rough interfaces, the potential $V(\vec{r})$ in Eqn. 3.2 decomposes into an unperturbed part V_0 of the perfect flat surface and δV , representing a weak disturbance due to the roughness. Fig. 3.3 (b) shows schematically the development of $V = V_0 + \delta V$ for a flat (left) and rough interface.

In case of a flat film, a finite step in the potential is visible, which is defined by the difference of ρ_e of both media. Roughness leads to a continuous transition of the depth profile of electron densities and hence to a continuous development of the potential $V(z)$.

For small roughnesses ($\sigma \ll D$), an effective Fresnel coefficient (modified by the Nevot-Croce-Factor [Nev80, Sin88]) is used for the calculation of the specular intensity:

$$\tilde{r}^j = r^j \cdot \exp[-2ik_z^j k_z^{j+1}(\alpha,t)(\sigma^j)^2], \quad (3.21)$$

where in this example, $j = 2$ corresponds to the V-C film, $j = 1$ to the Si substrate, and $j = 0$ to vacuum.

Due to the roughness of the layers, the specular intensity decreases. Interfacial roughness gives rise to intensity in the off-specular direction, the so-called *diffuse scattering*, which will be described in the next section.

3.4 Diffuse scattering

As stated in the previous section, interfacial roughness gives rise to intensity in the off-specular direction ($q_{x,y} \neq 0$). The scattering geometry is schematically represented in Fig. 3.4.

The diffusely scattered intensity can be calculated on the basis of the distorted-wave Born approximation [Sin88, Pie04]. The height fluctuations of the smooth surface are assumed to small perturbations of the perfectly flat interface. The scattered intensity per unit area is given by:

$$I(\vec{q}) = I_0 \frac{\exp(-q_z^2 \sigma^2)}{q_z^2} \int \int \exp(q_z^2 C(x,y)) \exp(-i(q_x x + q_y y)) dx dy, \quad (3.22)$$

where $C(x,y)$ is the height-height correlation function

$$C(x,y) = \langle \tilde{z}(x - x', z - z') z(x,y) \rangle. \quad (3.23)$$

With $C(x,y)$, the surface is described statistically. It provides quantitative information about lateral correlations and height variations.

In multilayer systems, the incident X-rays scatter at each rough interface. The correlation function for each interface and their cross correlations needs to be considered:

$$C_{ij}(x,y) = \langle z_i(x,y) z_j(x,y) \rangle, \quad (3.24)$$

where i and j correspond to different layers i and j . Fig. 3.5 (a) shows schematically different multilayer structures: (1) an ideal multilayer structure with perfectly flat interfaces, (2) a perfectly correlated multilayer in vertical direction, and (3) an extreme case of an uncorrelated multilayer systems.

In the later case, $C_{ij} = 0$, the diffusely scattered intensity of each layer adds up incoherently. The average of the scattering cross sections of the interfaces is measured.

For a perfectly correlated multilayer, the scattering signal of equivalent layers are measured. However, in most cases, the multilayer systems are only partially correlated.

Fig. 3.5 (b) shows schematically the distribution of the diffusely scattered intensity for a partially correlated multilayer system. The red line corresponds to the specular reflected beam at $q_x=0$. The gray area are not accessible, since in this case $\alpha_f < 0$ or $\alpha_i < 0$ in case of coplanar geometry.

For a partial correlation of the roughness of the layers, maxima are visible (1), occurring due to resonant diffuse scattering (RDS). The intensity stripes along $q_{||}$ are located at the

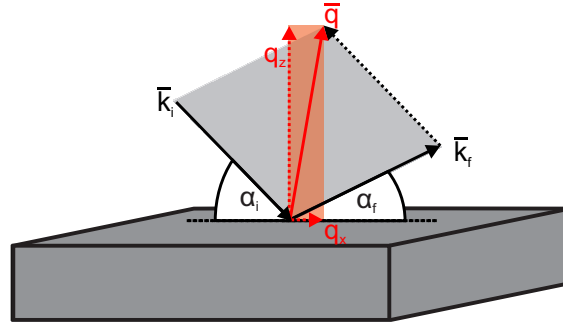


Figure 3.4: Scattering geometry of XRR measurements. Interfacial roughness gives rise to intensity in the non-specular direction.

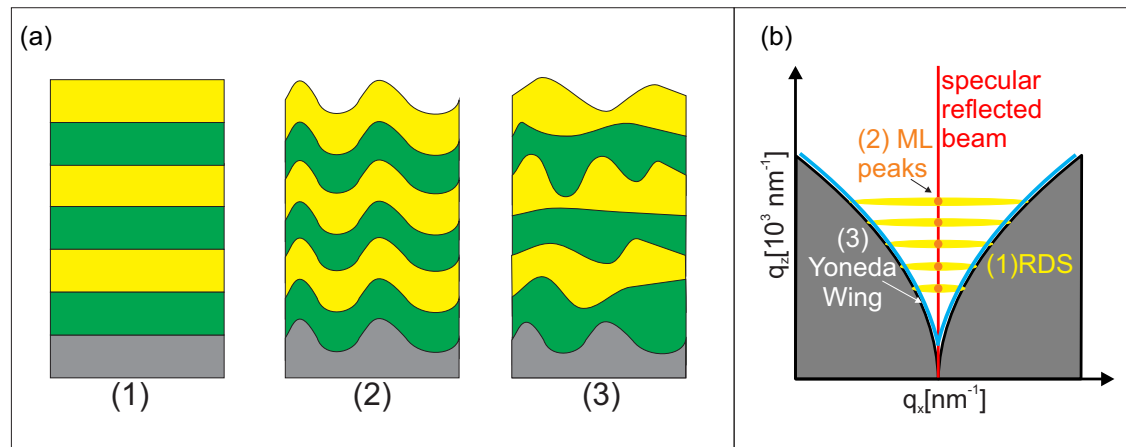


Figure 3.5: (a) Schematic of multilayer structures: (1) ideal multilayer, (2) with perfect correlated roughness, and (3) with uncorrelated roughness. (b) Scheme of a diffuse XRR map indicating the characteristic features in case of measuring a multilayer system with correlated roughness. The gray dotted line indicates More details s. text.

multilayer peak positions (2) in q_z . Bending of the stripes can occur due to refraction. Due to the similarity, they are often called *bananas*.

Another important feature of the diffuse map is the so called Yoneda wings. They appear independent if the roughness of the system is correlated or not if $\alpha_i = \alpha_{crit}$ or $\alpha_f = \alpha_{crit}$. Hence their position in reciprocal space is a direct measure for the electron density (s. Eqn. 3.16).

4 X-ray Photoemission spectroscopy (XPS)

The chemical composition of the VC_{1-x}/a-C thin films is important, since it influences the microstructure formation (s. Chap. 2). In this work, X-ray Photoemission Spectroscopy (XPS) used for the determination of the chemical composition and the chemical bonding in thin films.

In this chapter, the basic principle of XPS is outlined. The characteristic features of an XPS spectrum are presented. Different background subtraction methods are discussed.

4.1 Basics of X-ray photoemission spectroscopy

if an electron within some material absorbs the energy of one photon and acquires more energy than the work function (the electron binding energy) of the material, it is ejected.

In the following, the basic principle of XPS is outlined, based on [Bri03, Mou92, Fai05, Wat03].

In general, XPS uses the external photoelectric effect: *Photoelectrons* are emitted from a solid if they absorb energy from photons (s. Fig. 4.1 (a)).

For an XPS measurement, the sample is illuminated by soft X-rays as illustrated in Fig. 4.1(b).

The kinetic energy E_{kin} of the emitted photoelectrons is detected via an electron energy analyzer.

This method is very surface sensitive (in the regime of few *nm*) due to the low inelastic mean free path $\lambda(E_{kin})$ of the electrons.

Measurements are performed in ultra high vacuum chambers to allow first the photon to reach the sample and secondly the emitted electrons to travel to the energy analyzer. Additionally surface contamination and beam induced damages are reduced.

The binding energy E_B corresponds to the energy difference between the initial state of the atom and its final state after the ionization. The probability for this transition can be estimated in first approximation by Fermis golden rule. The binding energy E_B of the photoelectrons is $E_B = h\nu - E_{kin}$, where $h\nu$ is the energy of the X-ray photons.

For each element, a unique set of E_B for the different atomic orbitals exists, hence XPS is an element-sensitive method. In addition to that, different chemical bonding leads to slight shifts in the binding energy due to different chemical potentials.

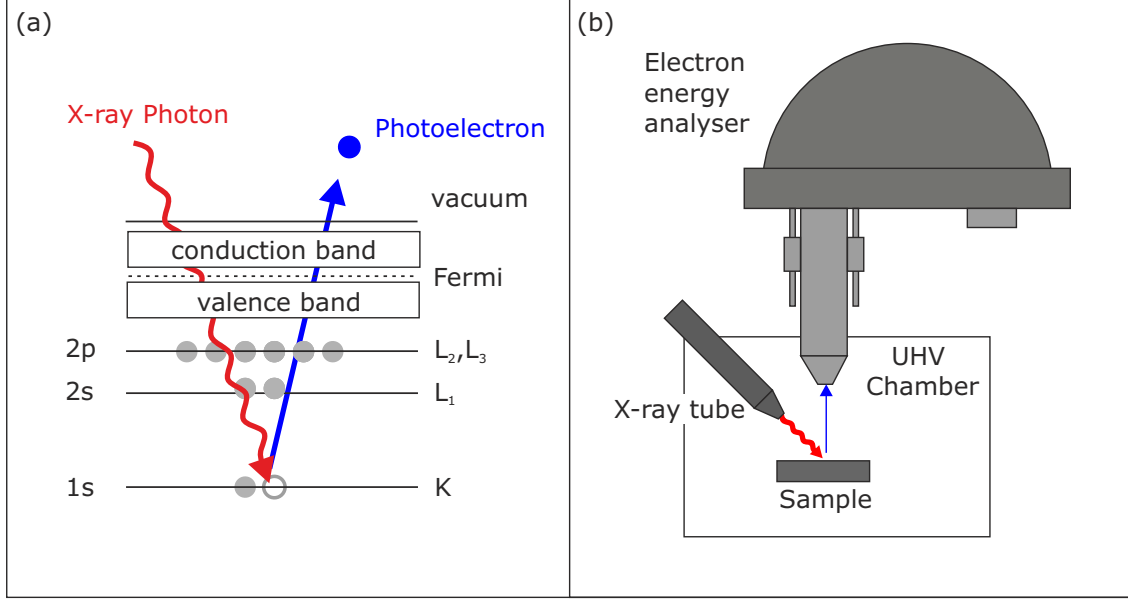


Figure 4.1: (a) Scheme of the emission of a photoelectron due to the irradiation of X-rays. (b) Scheme of an XPS chamber showing X-ray tube, sample and electron energy analyzer

4.2 Characteristics of XPS spectra

In the following, the characteristic features of an XPS spectra is presented. As an example, Fig. 4.2 shows the XPS spectra of a VC_{1-x}/a-C film using Mg as an anode material. The details of the experiment are described in Sec. 5.

The photoemission peaks of V are highlighted in Fig. 4.2 (a) (orange boxes). The V2s and V3s peaks result from photoelectrons from the s-orbital of the second and third shell, respectively. V2p is splitted into the Vp1/2 and Vp3/2 peaks due to spin-orbit-coupling. Besides photoemission lines, other peaks arise in the spectrum. (1) Auger electrons are arising due to the relaxation of the excited ions. The LMM - transition of V is depicted in Fig. 4.2 (a) (blue boxes). (2) In case of an unmonochromatized X-ray beam, satellite peaks occur due to different fluorescence lines of the anode material. Further characteristic features of an XPS spectrum can be found in [Mou92].

Assuming a smooth and homogenous film with a minimum thickness of 10 nm, the intensity of a photoemission peak of an element A with a core level N is given by

$$I(A, N, h\nu, E_{kin}) \propto c(A) \cdot \underbrace{\sigma(A, N, h\nu) \cdot T(E_{kin}) \cdot \lambda(E_{kin})}_{R.S.F}, \quad (4.1)$$

$\sigma(A, N, h\nu)$ is the cross section of the for the investigated transition, $c(A)$ the atomic concentration of the element in the sample and $T(E_{kin})$ is the transmission function of the

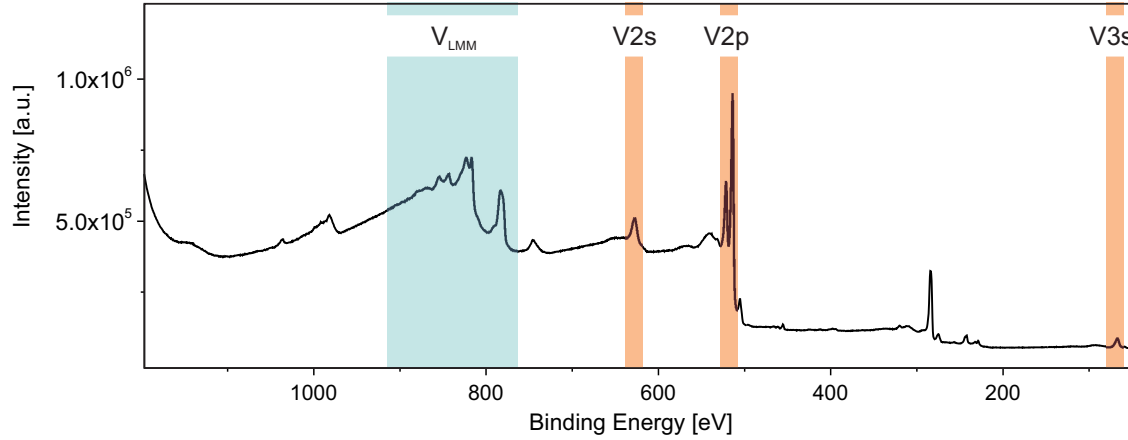


Figure 4.2: XPS spectrum of a VC thin film. The photoemission peaks of V and the Auger line of V (V_{LMM}) are highlighted.

used electron analyzer.

The product $\sigma \cdot \lambda(E_{kin}) \cdot T(E_{kin})$ can be described a relative sensitivity factor (R.S.F) which depends on the instrument used for the measurement.

For the determination of the chemical composition, the peak area has to be determined. The chemical composition for a material consisting of two elements A and B is:

$$\frac{c(A)}{c(B)} = \frac{I(A)}{R.S.F.(A)} / \frac{I(B)}{R.S.F.(B)}. \quad (4.2)$$

where $I(A)$ and $I(B)$ are the peak area of the main peaks of element A and B, respectively.

For the determination of the peak area, the background due to multiple scattering of the electrons needs to be subtracted. The background is strongly dependent on the microstructure of the material and the used element. In general, three background subtraction methods are used: linear, Shirley and Tougaard background.

Fig. 4.3 (a) shows the three different background methods applied to the V2p peak. The most simple background is the linear background (red line) assuming just a straight line between two points right and left of the peak. The Shirley background (blue line) is proportional to the peak area above the background in the given range. The Tougaard background (green line) is based on the universal cross-section approach. The linear and the Shirley background are strongly dependent on the end points of the integration range. For both backgrounds it is possible to generate negative peak areas. In Fig. 4.3 (b) the V2p peak is shown after background subtraction. The peak area is strongly influenced by the choice of background, resulting in a systematic error in the determination of the chemical composition.

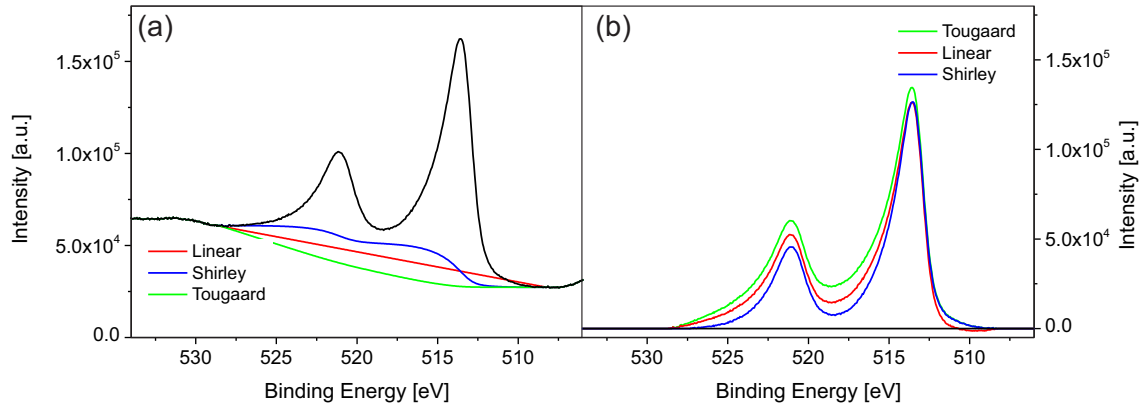


Figure 4.3: (a) V2p peak with the three different backgrounds. (b) V2p after background correction.

For the non-metallic elements, peak area was determined after the background correction using all three backgrounds. The changes in the area are around 3 %.

For the metallic elements, the difference in the area after subtraction of the background exceeds 15%. [Tou93, Rep92] found out that in case of transition metals, the linear as well as the Shirley background lead to a higher error compared to the Tougaard background. This is explained by the additional contribution of the partially filled *d* sub-shells.

Taking additionally slight differences in the R.S.F.s into account, the chemical composition can be determined within an error of 4-5%.

In conclusions, XPS is a surface sensitive method which can be used for the qualitative analysis of the elements in the film and their chemical bonding. Furthermore, the chemical composition in the film can be analyzed. The here described method is used in Chapter 10 to investigate the chemical composition of samples grown at low and high pressure.

Part II

Experimental Details & Simulations of the sputter process

5 Experimental details

In this chapter, the experimental details are outlined.

The sputtering chamber system used for this work is described. The preparation of the samples used in this work are described.

The measurements were mostly performed at the Ångströmquelle Karlsruhe (ANKA), where - besides the a synchrotron radiation source - a growing laboratory infrastructure exists. For the *in situ* measurements, the sputter chamber system was installed at the Max-Planck Beamline (MPI). For *in vacuo* experiments, the chamber was installed at the UHV Analysis Laboratory. The experimental setup of further complementary methods are described at the end of the chapter.

5.1 The portable sputter chamber system at IPS

The modular and portable sputtering system consists of the sputtering chamber, a control unit, and a gas panel (s. Fig. 5.1 (a)). The sputter chamber allows different configurations since the bottom, middle and top part can be exchanged. The currently available options can be found [Kra12].

The configuration of the sputter chamber used for this work is schematically shown in Fig. 5.1 (b):

A 3'' magnetron source (Thin Film Consulting) is attached to the top part via a CF 100 flange. As target material, a stoichiometric V-C target (MaTecK GmbH) was used. The composition of V:C=1:1 of the target was confirmed by EPMA measurements of our collaboration partners at IAM-AWP, KIT.

The central part of the chamber was equipped with Beryllium (Be) windows, covering an azimuthal angle of -50 to +65°. 70 μm thick Kapton foil was mounted in front of the Be windows to protect them from coating during the deposition. Both Be and Kapton have a low absorption in the X-ray regime, which is crucial for the *in situ* experiments. The pumping system, pressure control system and sample manipulator systems are mounted on various flanges at the middle and top part:

The pumping system consists of a membrane pump (Vacuubrand) and a turbo pump (Pfeiffer Vacuum, HighPace300). The base pressure of the system was in the order of 10^{-7} Pa after bake-out.

The chamber is equipped with two systems for pressure measurement: a cold cathode for wide range pressure measurement (Atmion, VACOM), and a baratron for pressures larger than 0.01 Pa during deposition.

The bottom flange with a sample storage for 5 sample holders was used, allowing the

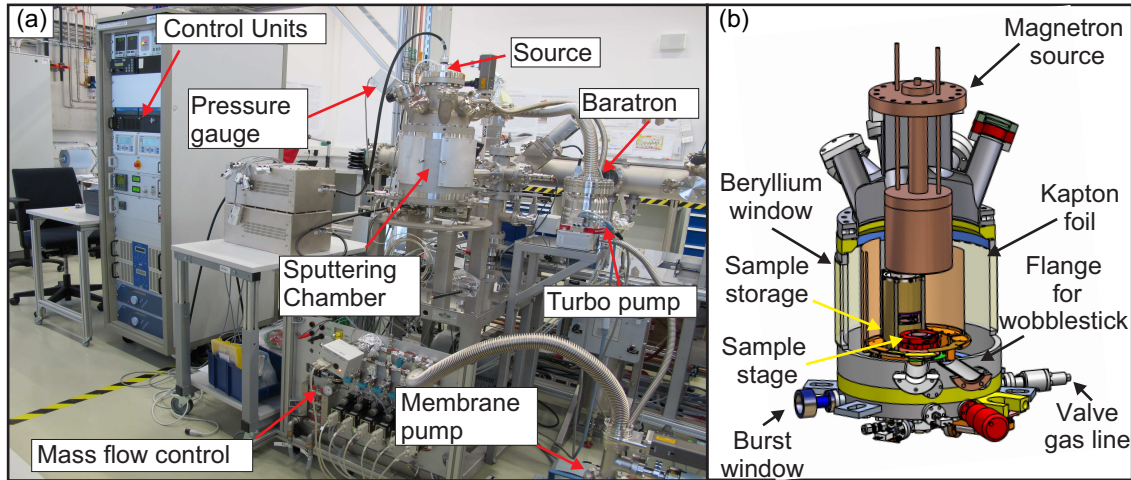


Figure 5.1: (a) The sputtering chamber system installed at the UHV Analysis Laboratory at ANKA highlighting important parts. (b) Scheme of configuration of the sputter chamber used in this work.

exchange of 5 samples during an *in situ* experiment without breaking the vacuum.

The distance between target and substrate was 12 cm.

As sputter gas Argon 6.0 was used with a purity of 99.9999 vol. %. The flow of the sputter gas Argon into the chamber was controlled via two mass flow controllers (MKS) with flow ranges of 0-10 sccm (low flux) and 0-50 sccm (high flux). The latter was used for the high Ar flux needed in the beginning of the deposition for plasma ignition. To ensure the purity of the gas in the gasline, the latter was flushed several times with Ar before the deposition.

The whole deposition was controlled by a software developed by Diener automation GmbH & Co. KG [Die14]. All important deposition parameters, e.g. the applied power and the pressure, are logged with a data acquisition frequency of 1 s. This offers the possibility to relate the *in situ* X-ray data with the growth parameters of the sputtering process for the analysis.

5.2 Sample preparation

The $\text{VC}_{1-x}/\text{a-C}$ thin films were deposited on silicon by DC magnetron sputtering. The silicon substrates with (100)-orientation had a lateral size of $20 \times 20 \text{ mm}^2$ and a height of 0.5 mm. The substrates were covered by a natural oxide layer with an average thickness of approximately 2.5 nm, which was verified by XRR and TEM measurements.

The substrates were mounted on molybdenum sample holders with clamps made out of tantalum foil. The silicon substrates were ultrasonically cleaned in acetone before being

Sample	DC Power	Pressure (initial)	Pressure	Deposition Time
	[W]	[Pa]	[Pa]	[s]
VC_{1-x}/a-C Samples				
LP-a(3.5)	200	3.5	0.2	650
LP-b(3.5)	200	3.5	0.2	650
LP-c(3.5)	200	3.5	0.2	650
LP-a(1.5)	200	1.5	0.2	650
LP-a(2.5)	200	2.5	0.2	10 × 200
HP-a	200	3.5	4	650
HP-b	200	3.5	4	650
P-step	50 → 200 with $\Delta P=25$ W (250 s)	2.5	0.2	2900
gas-ML	200	3	10 × (3 → 0.2)	2560
Reference Samples (using V 1'' -target)				
LP-EPMA	200	3.5	0.2	3600(V) + 6640(V-C)
V-XPS	200	3.5	0.2	2700

Table 5.1: Overview of all samples presented in this work. → indicates, that the growth parameter is not constant over the entire deposition time.

transferred to the sputtering chamber. Before deposition, the substrates were heated to 200°C to remove e.g. remains of water and hydrocarbon.

Several samples were grown under identical deposition conditions to ensure reproducibility. The samples discussed in detail in this work are presented in in Tab. 5.1. Their growth details are described in the following.

All thin films presented in this work were grown at room temperature. No additional heating was applied. Due to the large target-substrate distance, no significant heating due to the plasma is expected. No bias was applied. All samples were grounded.

The development of the DC Power (red curve) and the pressure in the chamber (blue curve) of the first series of samples is presented in Fig. 5.2 (a).

A high Ar flux up to 10 sccm was required for the plasma ignition at a DC power of 50 W. The high flux lead to an increase in the initial chamber pressure up form p=1.5 Pa to 4 Pa. After 10 s, the Ar flux was reduced to 0.4 sccm. The working gas pressure decreased to p=0.2 Pa. Simultaneously, the power was ramped to the final value of 200 W within 20 s, to avoid cracking of the target. The conditions were kept constant for the desired deposition time. Then the DC Power was ramped down to 50 W, before the growth was stopped.

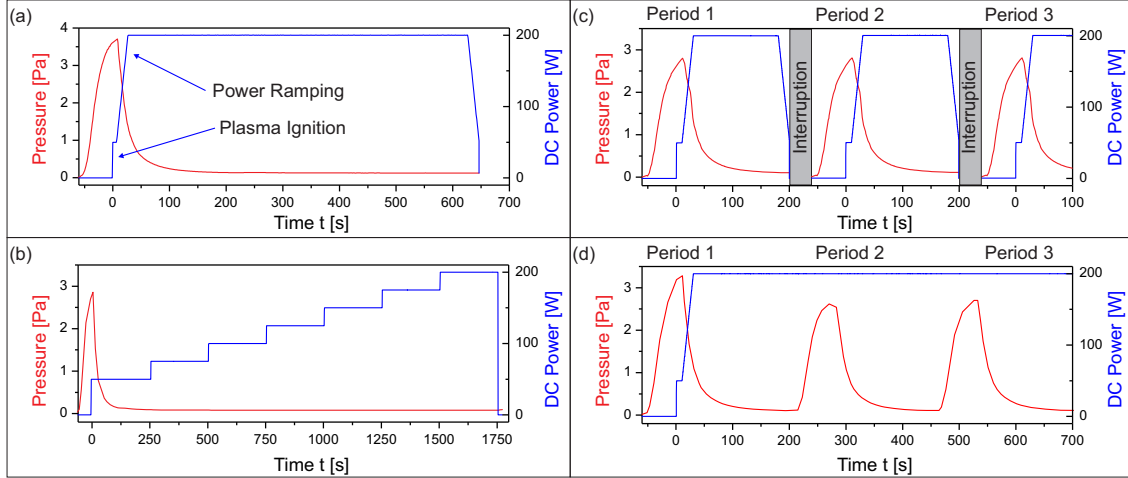


Figure 5.2: Time-dependent development of DC Power (red) and pressure in the chamber (blue) logged during the growth of (a) *LP-a(3.5)*, (b) *P-step*, during the multilayer growth (c) by interrupted deposition (*LP-a(2.5)*) and (d) by tuning the gas flow (*gas-ML*). Please note, that for *LP-a(2.5)* the different periods were put after each other. The interruption is indicated by gray boxes.

Samples grown under these conditions are abbreviated by *LP(p)*, where *p* corresponds to the initial pressure. For the comparison of different *in situ* measurement types (Chap. 7), two samples were deposited under the same growth conditions. To distinguish the two samples (*LP-a(3.5)* and *LP-b(3.5)*) an additional letter (*a,b*) is included in the nomenclature.

For the investigation of the influence of the initial growth, samples were deposited at different initial pressure at plasma ignition. As representatives, the samples *LP-a(1.5)*, *LP-a(2.5)*, *LP-a(3)*, *LP-a(3.5)*, and *LP-a(4)* - grown at the initial pressures of 1.5 Pa, 2 Pa, 3 Pa, 3.5 Pa and 4 Pa - are presented in Chap. 11.

For the investigation of the influence of the pressure on the thin film formation (Chap.10), the sample *HP-a* was grown at a constant pressure of $p = 4$ Pa. The total deposition time including ramping was $t = 650$ s.

For complementary measurements (X-ray Diffraction and X-ray Photoemission Spectroscopy) *LP-c(3.5)* and *HP-b* were deposited under the same growth conditions as *LP-a(3.5)* and *HP-a*, respectively.

For the investigation of the influence of the DC power on the thin film formation, the sample *P-step* was grown (s. Chap. 9). The development of the DC Power (red curve) and the pressure in the chamber (blue curve) are presented in Fig. 5.2 (b)).

After the plasma ignition, the DC Power was increased stepwise every 250 s by $\Delta P = 25W$ from 50 W to 200 W.

For the growth of a multilayer structure, the deposition conditions of *LP-a(2.5)* were repeated 10 times (s. Fig. 5.2 (c)). The growth was interrupted after each deposi-

tion.(Chap.13). For comparison, *gas-ML* was grown without growth interruptions (s. Fig. 5.2 (d)).

In addition to those films, reference samples were grown.

To verify that compositional changes in the film are not related to C contamination from the chamber or gas system (s. Chap. 10), the sample *V-XPS* was grown using a V target. The growth conditions were identical to *LP-a(3.5)*.

The determination of the chemical composition was verified by EPMA measurements of *LP-EPMA*, performed by our collaboration partners at IAM-AWP, KIT. For a successful EPMA measurements, the thickness of the sample must exceed 1 μm . To achieve this thickness, a promoting layer of V having a film thickness of 100 nm was grown as a buffer layer. The growth conditions were kept identical to *LP-a(3.5)*. The total deposition time was increased to 5200 s.

5.3 Experimental setup for the synchrotron experiments

The *in situ* measurements were performed at the Max-Planck Beamline at the synchrotron facility ANKA. In this section, a short description of ANKA is given. The experimental setup of the *in situ* measurements at the Max-Planck Beamline is described. Details of the X-ray reflectivity measurements are presented.

5.3.1 Ångstromquelle Karlsruhe

The Ångstromquelle Karlsruhe (ANKA) is a synchrotron radiation facility at the Karlsruhe Institute for Technology (KIT), Karlsruhe. Around the synchrotron, several laboratories are located (s. Fig. 5.3).

The ANKA accelerator complex consists of a 500 MeV booster synchrotron and a 2.5 GeV storage ring with a circumference of 110 m. The storage ring has straight and curved section. The latter are equipped with dipole magnets, so called *bending magnets*. The magnetic field is generated via electric currents running through coils.

Bunches of relativistic electrons are injected into the storage ring. The electrons are deflected by the bending magnets on the circular orbit. Synchrotron radiation is emitted in tangential direction to their path way via the radial acceleration, resulting in a fan beam. The spectrum of the electromagnetic waves tangential to the path way varies from infra-red up to the hard X-ray regime. The latter is used for this work.

Experimental stations are build tangential to the storage ring. They are called beamlines. Compared to conventional laboratory X-ray sources, synchrotron radiation has a higher intensity over the entire spectrum. Using monochromator, one can choose the wavelength λ suitable for the experiment.

The experiments are performed in beamlines, which are build tangential to the storage ring. For this work, measurements were performed at the MPI Beamline at ANKA, which is dedicated to *in situ* experiments and will be described in more detail in the next section.

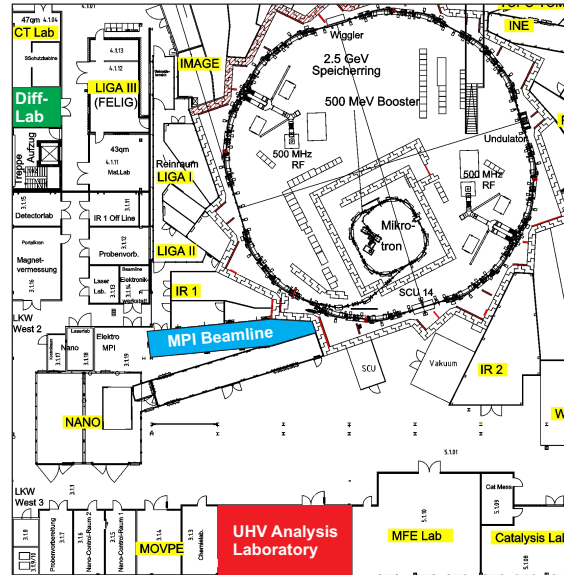


Figure 5.3: Map of part of the ANKA hall. The synchrotron experiments were performed at the MPI Beamline (highlighted in blue). Complementary measurements were performed at the UHV Analysis Lab (highlighted in red) and the DiffLab (highlighted in green).

For a detailed description of synchrotron radiation we refer to [Ulr04, AN11].

5.3.2 The Max-Planck Beamline at ANKA

The Max-Planck (MPI) Beamline is a bending magnet beamline located at ANKA. It is dedicated to the *in situ* investigation of interfaces and thin films [Sti04].

Fig. 5.4 shows the schematic beamline layout. In general a beamline consists of three rooms: The optical hutch, the experimental hutch and the control room.

In the optical hutch, the properties of the X-ray beam as size, energy and focus are tuned. The source has a divergence of 0.3 mrad in horizontal and 0.03 mrad in vertical direction. Two pairs of vacuum slits are used to define the horizontal and vertical beam size (Slit 1). Behind the primary slits, a Rh coated Si mirror is mounted for the suppression of higher harmonics. A Si (111) double crystal monochromator was used to monochromatize the beam to 10 keV. The beam was focused in vertical direction by the mirror, and in horizontal direction by the second crystal of the monochromator (sagittal crystal bender) to $300 \mu\text{m} \times 300 \mu\text{m}$ on the sample position.

The experimental hutch is equipped with a heavy duty HUBER 4+2 -Diffractometer. It can carry up to 300 kg (in the here used configuration). Therefore, it is possible to mount the sputter chamber weighting 60 kg.

In front of the diffractometer a flight tube is installed to reduce the air scattering. A slit

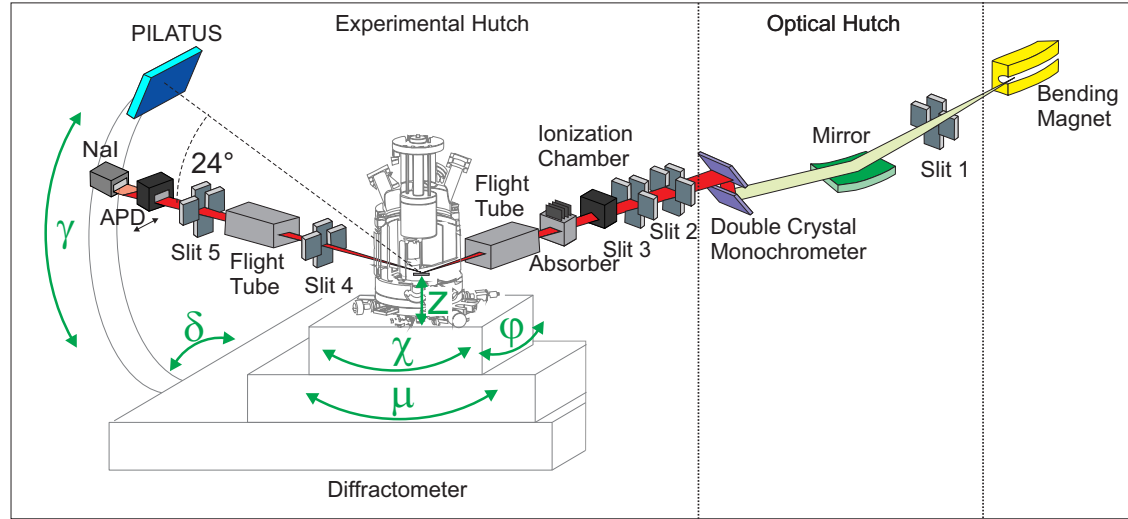


Figure 5.4: Schematic beamline layout of the Max-Planck-Beamline located at ANKA.

system (Slit 2 and 3) is installed allowing preselection of the beam size on the sample. Behind these slits an ionization chamber is installed to monitor the incident photon flux. The beam position is fixed. Therefore, the diffractometer was moved in lateral and vertical direction, to put the center of rotation of the sample at the beam position.

For the *in situ* experiments, the sputtering chamber was mounted on the diffractometer as shown in Fig. 5.5.

Various detector systems were attached to the detector arm. For this work, an avalanche photodiode (APD), a NaI scintillator, and a PILATUS 100K with an active area of 195×487 pixels and a pixel size of $172 \times 172 \mu\text{m}^2$ were used as detectors. The APD is mounted in front of the NaI detector and can be automatically retracted. Automatic absorbers were used in case of the NaI detector. In this way, the detector was protected from beam damage. Moreover, the linear operation of the scintillator was ensured. The PILATUS detector is installed on an additional part of the detector arm, 24° away from the other detectors. On the detector arm, two slit systems are mounted, which are used as guard slits and to reduce the diffuse scattering.

After the mounting of the sputter chamber, special care had to be taken to avoid collisions with the diffractometer and the detectors during movement. The diffractometer motors used for the experiments and their direction are schematically shown in Fig. 5.4. Soft limits of motor movements were set for protection of the setup.

The movement of the motors as well as the deposition process was remote-controlled from the control room of the beamline.

As a first step, the silicon substrates had to be aligned with respect to the direct beam ($\gamma = 0$ and $\delta = 0$). φ and χ -scans were used to align the surface normal to the direct beam. In addition, the substrate was moved in height to the position, where half of the

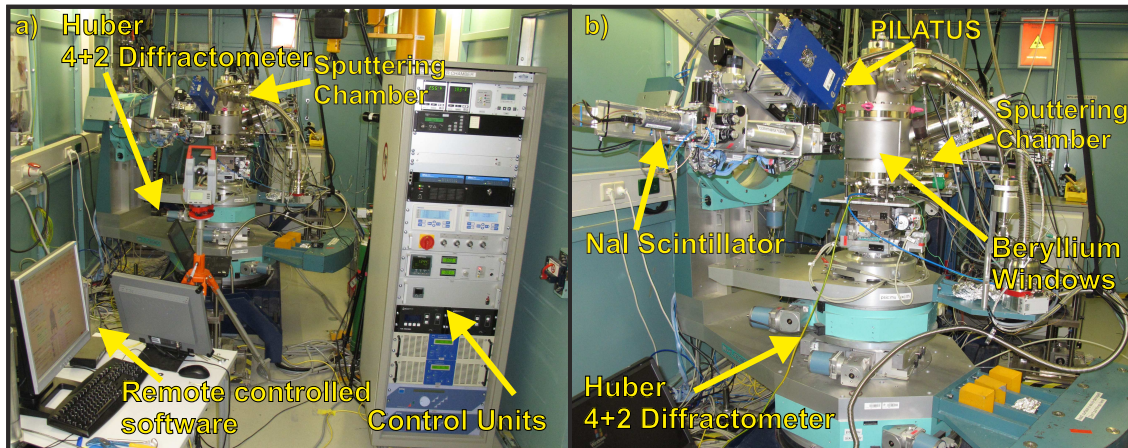


Figure 5.5: The sputtering chamber setup at the MPI Beamline in the experimental hutch. a) Overview showing the chamber mounted on the 4+2 circle diffractometer, the control unit and the PC for the automatically control of the deposition process. b) Closer look at the 4+2 circle diffractometer. The beryllium windows are shown without protection shielding. The three detectors (PILATUS, APD, and NaI scintillator) are fixed on the detector arm of the diffractometer.

intensity is cut (using the z -motor).

Rough alignment was performed in the direct beam using the APD. The diode can stand the high intensity of the direct beam.

Re-adjusting of the positions was performed on the reflectivity position. At this position, one is more sensitive to changes of the tilt.

Since the alignment for all Si wafers was similar, macros in SPEC were written for the automatized alignment of all substrates.

After alignment, the X-ray reflectivity measurements were performed, which are described in the following section.

5.4 X-ray reflectivity measurements

Two different types of X-ray reflectivity measurements were performed in this work: angle-dependent and stationary measurements. In the following, the experimental setup for both measurement types is outlined. The dataprocessing is described.

5.4.1 Angle-dependent XRR measurements

Angle-dependent XRR measurements were performed before, during and after the thin film deposition. For the measurements, the motors μ and γ were scanned simultaneously. For the scan, $\mu = \gamma$, where γ is the angle relative to the sample surface.

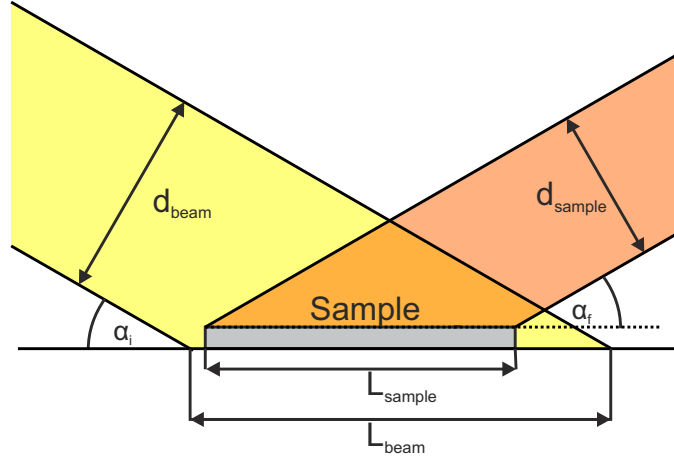


Figure 5.6: Scheme for the determination of the geometry factor showing the illumination of the sample at small incidence angles. After [Pie04].

A typical scan range of $0.1\text{--}4.1^\circ$ and an angular step size of $\Delta\alpha = 0.005^\circ$ was used. The measurements were performed using the NaI scintillator. For these scans the automatic absorbers were used.

For all measurements, the slit sizes were kept constant in horizontal and vertical: slit 3 at $5 \times 0.5 \text{ mm}^2$, slit 4 at $8 \times 1.5 \text{ mm}^2$, and slit 5 at $0.3 \times 1.5 \text{ mm}^2$.

During a measurement, besides the specular intensity additionally a part of the diffuse intensity is recorded. Hence offset scans were performed, measuring the diffuse scattering close to the specular rod. The offset scans are subtracted from the specular intensity before analysis.

Furthermore, geometrical effects need to be considered. The *footprint* d_{beam} is the projection of the X-ray beam on the sample. For small incidence angles α_i , the footprint of the beam is larger than the sample with the width d_{sample} (s. Fig. 5.6). In this case, the measured intensity depends on the ratio d_{beam}/d_{sample} . For $\alpha_i < \arcsin(\frac{d_{beam}}{L_{beam}})$, the measured intensity I_{meas} is corrected using

$$I_{corr} = \begin{cases} I_{meas} \sin(\alpha_i) & \text{for } \alpha_i < \arcsin(\frac{d_{beam}}{L_{beam}}) \\ I_{meas} & \text{for } \alpha_i \geq \arcsin(\frac{d_{beam}}{L_{beam}}) \end{cases}, \quad (5.1)$$

As a final step, the specular intensity was normalized to maximum intensity.

In addition to the synchrotron experiments, angle-dependent XRR measurements were performed at the DiffLab at ANKA. A Cu K_α X-ray source was used ($\lambda = 1.542 \text{ \AA}$) with a rotational anode. The measurements were performed in parallel beam geometry.

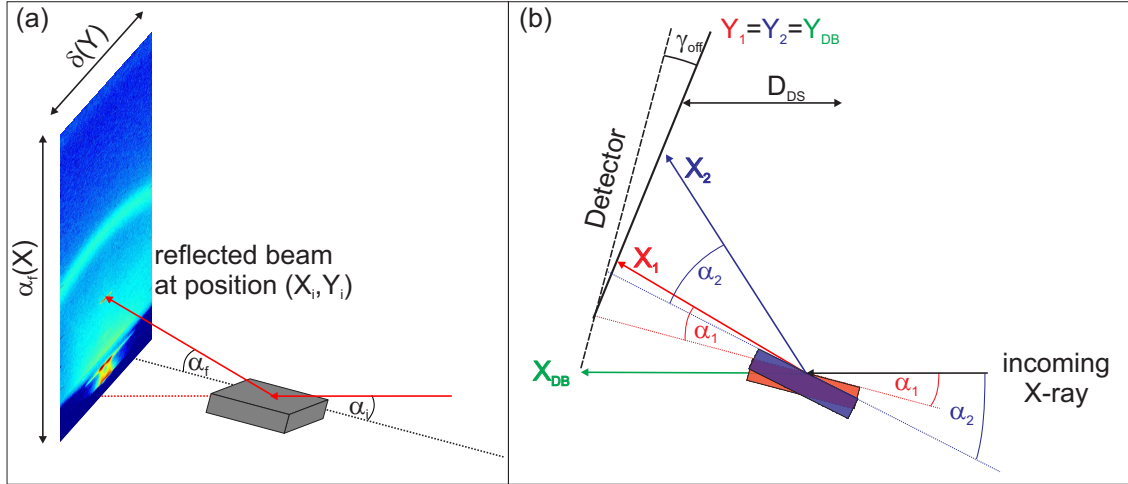


Figure 5.7: (a) Scheme of the scattering geometry setup at fixed angular position. (b) Schematic drawing of the different angle positions at the specular beam used for the conversion of pixel in angular range.

5.4.2 Stationary XRR measurements

Besides the angle-dependent XRR measurements, the specular intensity was recorded at a fixed angular position $\alpha_{fix} = 1.6^\circ$. This is schematically shown in Fig. 5.7 (a).

These measurements were performed using the PILATUS detector. The images were taken in time steps of 1.1 s, including the additional read-out time of the detector of 0.1 s. The slit system in front of the sputtering chamber was fully opened (15 mm) in horizontal direction, resulting in a higher intensity. The spotsize was similar compared to the closed slit.

As a first step of data processing, the pixel values needed to be converted into angular space. For that, the distance between detector and sample D_{DS} , and the angular range A , covered by one pixel had to be determined.

It was not possible to measure D_{DS} using, e.g., a measuring tape. First of all, the sample was mounted inside the chamber during the experiment. Secondly, the position of the detector chip inside the detector box is unknown. Therefore the following approach was used.

To avoid the exposition of the detector to the direct beam, an offset angle $\gamma_{off} = 1^\circ$ was chosen. The position of the direct beam (X_{DB}, Y_{DB}) is then given by *virtual* pixel numbers, since the pixels are out of the detector range.

Hence, after the alignment of the sample to the direct beam position (s. Sec. 5.3.2), the sample was tilted to two different positions in α_i ($\alpha_1 = 1^\circ$ and $\alpha_2 = 1.6^\circ$) as shown in Fig. 5.7 (a) and (b). In the PILATUS image, the corresponding pixel positions $(X_{1/2}, Y_{1/2})$ of the reflected beam at $2\alpha_1 = 2^\circ$ and $2\alpha_2 = 3.2^\circ$, respectively, were read out.

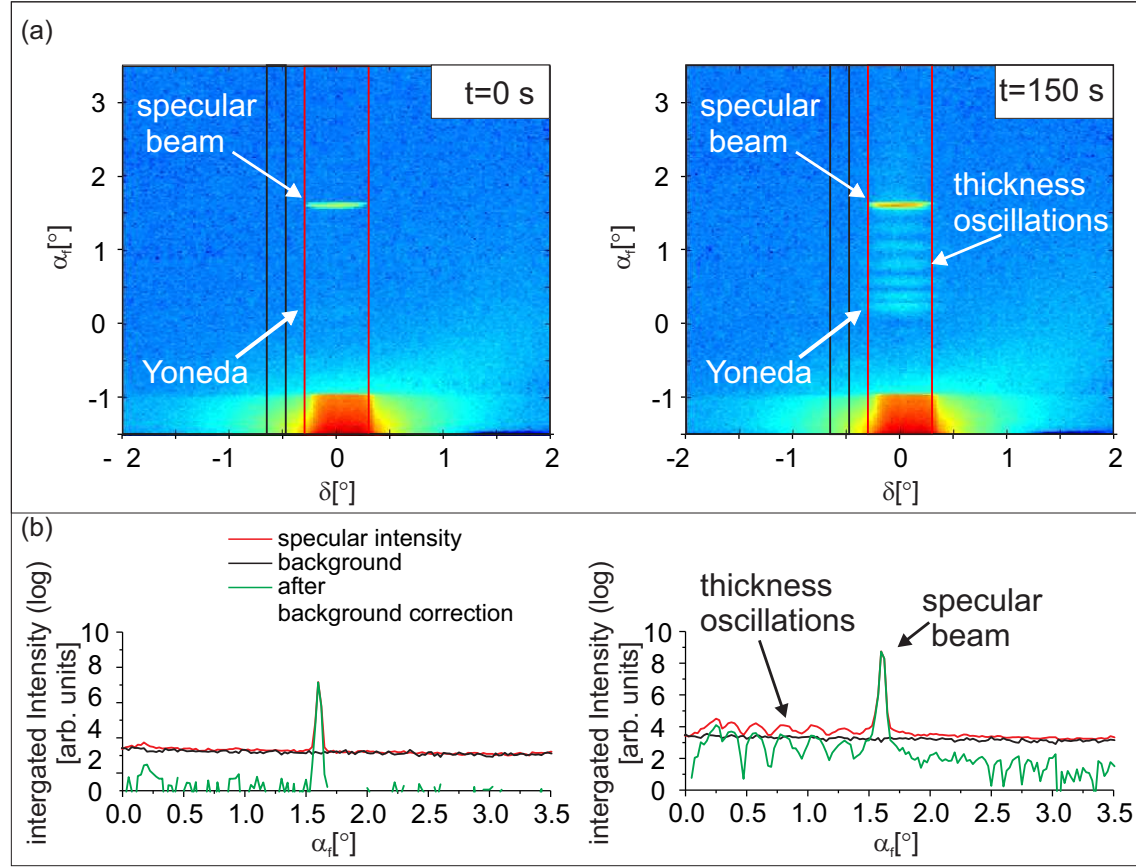


Figure 5.8: (a) Pilatus images before (left) and during deposition after 150 s (right). The images are already imported into MATLAB. The integration range for the specular beam is indicated with the red box, the region for the diffuse background subtraction is shown in black. Main features of the reflectivity are highlighted. (b) Integrated intensity around the specular beam (red lines) and the diffuse background (black lines), corresponding to the above-presented PILATUS images. Additionally the integrated intensity after background subtraction (green lines) is presented.

Since the chosen α_i are very small, the small-angle approximation is valid with $\sin(\alpha) \approx \alpha$. Hence, for the angular range A , the following relation is found:

$$A = (2 \alpha_2 - 2 \alpha_1)/(X_2 - X_1) = 0.025^\circ/\text{pixel} \quad (5.2)$$

Assuming small-angle approximation, the position of the direct beam (X_{DB}, Y_{DB}) was

determined by calculating the zero position via:

$$X_{DB} = X_1 - \frac{2 \alpha_1}{0.025^\circ} \quad (5.3)$$

and $Y_{DB}=Y_1$.

The detector-sample distance D_{DS} (s. Fig. 5.7 (b)) was evaluated via

$$D_{DS} = (X_1 - X_{DB}) \cdot L_{pixel} \cdot \tan(2\alpha_1), \quad (5.4)$$

where $L_{pixel} = 0.172$ mm correspond to the pixel size of the detector. The distance between sample and detector was found to be approximately 386 mm.

The angular position for each pixel were determined via:

$$\begin{aligned} \alpha_f(X_i) &= \alpha_f^* + \arctan \left[(X_i - X_{DB}) \frac{L_{pixel}}{D_{DB}} \right] \\ \delta(Y_i) &= \arctan \left[(Y_{DB} - Y_i) \frac{L_{pixel}}{D_{DB} \cos(\alpha_f[X])} \right], \end{aligned} \quad (5.5)$$

where $\alpha_f^* = \gamma_{off} - \alpha_i$, α_i where is the nominal settings of the instrument of the motors γ . Note that $\alpha_f[X]$ is calculated with respect to the surface of the sample, taking into account the offset of $\gamma_{off} = 1^\circ$.

All images were gridded. The distance of two grid points corresponds to the estimated angular step size per pixel from Eqn.5.2. The data were interpolated using the nearest neighbor interpolation. Here every interpolated pixel value corresponds to the value at the nearest sample grid point. This approach was chosen to avoid tampering the noise.

Fig. 5.8 shows two images (before and during the deposition) after the conversion of the pixel in the angular range. The intensity values are shown in logarithmic scale.

Besides the specular beam, the 2D detector additionally recorded the diffuse scattering. For the evaluation of the specular beam, the intensity was integrated over the width of the specular beam (red box), which is approximately 0.6° in δ direction (including the diffuse scattering close to the specular beam due to roughness). The integrated specular intensity is shown in Fig. 5.8 (b).

The scattering background of the sample environment was averaged (black box) and subtracted. The integrated diffuse scattering is presented in Fig. 5.8 (b). For all presented data, the error in specular intensity due to the diffuse scattering is smaller than 0.01% and can therefore be neglected.

This procedure was performed for all *in situ* scans at a fixed angular position.

5.5 X-ray Photoemission spectroscopy measurements at the UHV Analysis Laboratory

V-C oxidizes under ambient conditions. In addition the films will adsorb C. Especially the latter will drastically influence the results of the XPS measurements in the case of VC_{1-x} .

Measurements were performed at the UHV Analysis Lab at ANKA, which offers the great possibility to grow samples in the *in situ* chamber and transfer them directly into analysis chambers without bringing them in contact with air.

In the following, the UHV Analysis Lab is described. The details of the XPS measurements are presented.

5.5.1 The UHV Analysis Laboratory

The UHV Analysis Laboratory is located in the ANKA hall (s. Fig. 5.3).

Fig. 5.9 (a) shows schematically the ultra-high vacuum cluster at the UHV Analysis Laboratory. A transfer system connects several deposition chambers and analysis chambers. The parts of the cluster in the UHV Analysis Laboratory used in this work are highlighted in color. The sputtering chamber (green) was docked to the transfer system via the docking station (blue). New substrates were transferred into the cluster using the loadlock (yellow). After the growth of the thin films, they were moved using a trolley through the transfer system (orange) to the X-ray Photoemission (XPS) chamber (red). The samples were inserted in the XPS chamber via the linear transfer rods. The XPS chamber is shown in Fig. 5.9 (b). The experimental details of the XPS measurements are presented in the next section.

5.5.2 XPS measurements

For the measurements, a Phoibos 150 analyzer and an unmonochromatized XR-50 Mg K α X-ray source from SPECS were used. The angle between analyzer and X-ray source was 45° , the emitted electrons were detected along the surface normal of the sample. The energy scale was confirmed using the Cu2p_{1/2} XPS peak at 932.62 ± 0.05 eV and the Cu LVV Auger peak at 334.90 ± 0.05 eV. The base pressure of the XPS chamber was 1×10^{-10} mbar. No beam-induced changes of the spectra were detected. For the overview scans, an energy pass of 50 eV and energy steps of 0.5 eV were selected. For scans of defined regions, e.g. of single photoemission peaks, an energy pass of 20 eV and energy steps of 0.1 eV were used. The dwell time of 0.1 s was applied for all scans. For better statistics the scans were repeated several times. XPS measurements have been performed in the constant transmission mode. For verification of the constant transmission function $T(E_{kin})$ of the energy analyzer, an XPS spectrum of a silver sample was acquired. The silver sample was sputter cleaned to remove the oxide layer.

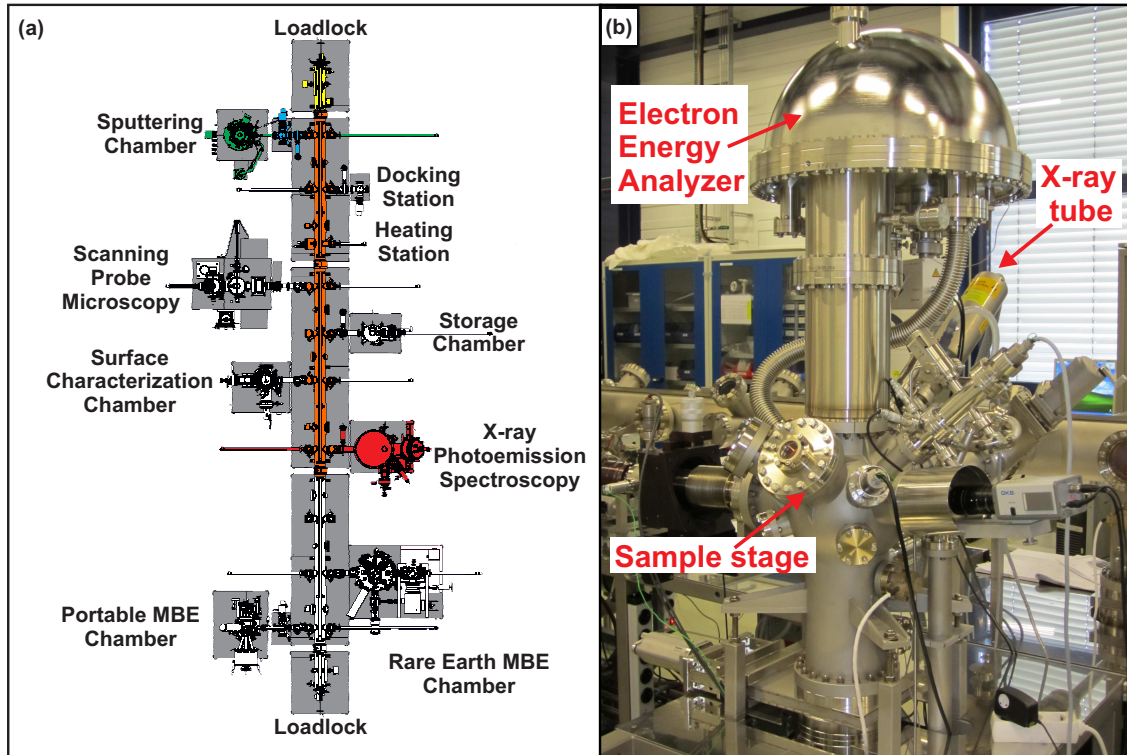


Figure 5.9: (a) Scheme of the UHV Cluster at the UHV Analysis Laboratory at ANKA. Highlighted with color: the sputtering chamber (green), the XPS Chamber (blue), docking station (red), loadlock (yellow) and used part of the transfer system (orange). Courtesy of CreaTec Fischer & Co. GmbH except image of AFM - Courtesy of Omicron Nano Technology GmbH. (b) The X-ray Photoemission Spectroscopy Chamber

The spectrum is compared with a reference spectra taken from [Sea90]. In this work the spectra was corrected in this way, that it is independent of the transmission function of the energy analyzer.

Fig. 5.10 shows the comparison of both spectra. For the here used interval of kinetic energy (highlighted by the blue box), the transmission function is equal unity. Hence, the transmission function is constant.

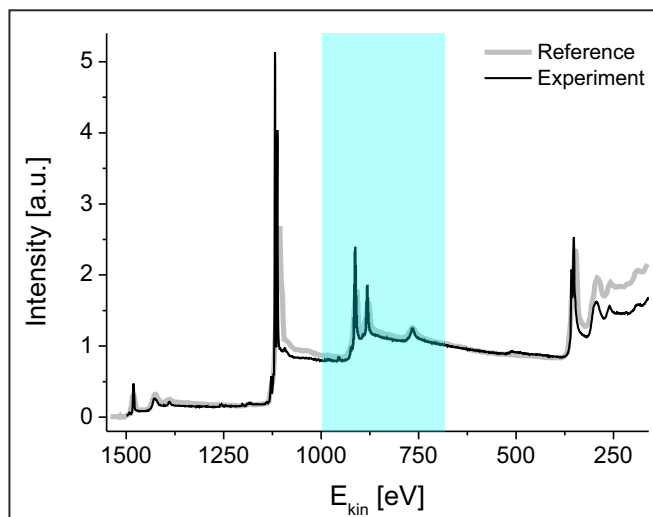


Figure 5.10: XPS spectrum of Ag reference sample (black) and reference curve (gray) taken from [Sea90].

5.6 Further complementary methods

Besides the above-mentioned analysis methods, further complementary methods were used for the investigation of the VC_{1-x} films. The here presented measurements were performed by collaboration partners.

High-resolution transmission electron microscopy (HRTEM) measurements were performed by Dagmar Gerthsen, Reinhard Schneider, Erich Müller, and Nadejda Firman, LEM, KIT.

For the investigation of the microstructure of the samples P -step, LP -a(3.5) and LP -a(2.5), C_s aberration-corrected HRTEM cross-section images were taken. For this, an FEI Titan³ 80-300 microscope operated at 300 keV accelerating voltage was used. The samples were prepared either by conventional preparation (P -step) or by FIB preparation (LP -a(3.5), LP -a(2.5)).

The chemical composition of the target and LP -EPMA was determined using Electron Probe Microanalyzer. The measurements were performed by Kolja Erbes, Michael Stüeber und Sven Ulrich, IAM-AWP, KIT.

For the texture analysis of LP -b(3.5) and HP -b, X-ray Diffraction (XRD) measurements were performed by Sunil Kotapati, IPS.

The scans along the surface normal in θ - 2θ geometry were conducted at the DiffLab at ANKA using the Rigaku SmartLab Diffractometer. A Cu K_α X-ray source was used (λ

= 1.542 Å). The measurements were performed in parallel beam geometry. A Ni filter was used to suppress the Cu K_{β} -lines.

6 Simulations of the sputter process

Simulations of the sputter process help to understand the thin film formation. However, sputtering from a compound target is difficult since it involves two elements with different properties. For the simulations, the sputter process is divided in two processes. The sputter process at the target position is calculated. The results of this simulations are then used as an input for calculations of the transport of the sputtered particles through the gas phase.

In this chapter, the different simulations are outlined. Assumptions for the sputter process are discussed.

6.1 The sputter process at the target position

For the investigation of the nascent energetic and angular distribution of the sputtered particles at the target, *TRIM* simulations (*TRansport Into Matter*) are performed. In general, the TRIM software is based on Monte-Carlo simulations and calculates the interaction of energetic ions with atoms in a solid. The collisions in the target are described using a quantum mechanical treatment of ion-atom collisions [Bie80, Zie85].

For the calculations, the energy of the ions, the surface binding energy *SBE* and the density ρ of the elements in the target have to be inserted as main input parameters.

For a compound target, these simulations are complex. Besides the sputter process, intermixing and variations in the target surface can occur due to the existence of more elements in the target. The *SBE* and the density ρ are usually unknown, since they strongly depend on the manufacturing process [Mra13, Nei08, Mah06a].

In case of sputtering from a compound target, two approaches for the simulations are available [Nei08, Mah06a].

1. The simulations are performed individually for all elements of the compound target, assuming single element targets [Mah06a]. The main advantage of this approach is the fact that *SBE* and ρ are much more reliable known for single elements. However, the sputtering process of a compound target is additionally influenced by dynamical processes as e.g. surface enrichment of one element. Hence the simulations of a single target describe the process only qualitatively.
2. The compound target is simulated by interpolating the values for *SBE* and ρ of the single elements according to their fraction in the target [Nei08, Mra13]. The simulations include additionally the intermixing and variations in the surface due to

the existence of more elements in the target. The calculations lack from the unknown parameters for compound targets, since SBE and ρ for a compound target strongly depend on the manufacturing process.

Besides the surface binding energy SBE and the density ρ of the elements in the target, the energy of the ions has to be inserted as a main input parameter. The energy of the Ar^+ ions depends on the applied DC voltage. [Cze91] calculated the relation of both parameters for the case of DC sputtering. They stated, that in most planar magnetron, the Ar^+ ions energy corresponds to 60% of the discharge voltage. Experimental studies, however, state that a more realistic values for the Ar^+ ions energy is found at 75% of the voltage [Dep08, Fil10].

Both approaches were performed for V-C using the software tools SRIM [Bie80, Zie85] and TRIDYN[Moe88]. For comparison, both approaches were followed using the same input parameters.

The Ar energy of 310 eV corresponds to 75% of the discharge voltage of 415 V at a DC Power of 200 W. 10^7 Ar ions were used for the simulations to ensure good statistics.

Tab. 6.1 presents the material-specific input parameters. For the TRIDYN simulations, the values for SBE and ρ of the V and C are interpolated according to their fraction in the target of V:C=50:50.

The results of the simulation for both approaches are presented in Tab. 6.2.

In case of the single-target-approach, the V atoms are almost four times as energetic than the C atoms. The TRIDYN simulations show a different behavior. Here, the C atoms have a higher energy. The E_{sp} s of both elements differs only by approximately 30%. Furthermore, huge differences in the total sputter yield Y_{tot} are found. Y_{tot} is almost a factor 4 higher for V than for C, while the sputter yield is almost equal in case of TRIDYN simulations.

The angular distribution of both elements is presented in Fig. 9.3.

In case of the single element approach, the emission flux of C is almost restricted to the direction perpendicular to the target surface (s. Fig. 9.3 (a), filled magenta circles). The angular distribution differs significantly from the expected cosine distribution (s. Sec. 1.1.2). The ideal spherical cosine distribution is indicated by a black line. For comparison of the emission flux of C with V, the axis is shown here in logarithmic scale for better visibility. The angular distribution of V, presented as filled blue squares, is much broader. The angular distribution of both elements, resulting from the TRIDYN simulations is presented in Fig. 9.3 (b). Compared to the results of SRIM, the angular distribution of C is broader (filled magenta circles) and more close to the ideal cosine distribution (black line). The distribution of V is under-cosine (filled blue squares). This so-called *heart-shaped* distribution is often reported for metallic targets, e.g. by [Mah06a, Yam95]. Both simulations show qualitative similarities. In both cases, an enhancement of the C flux for emission angles $< 30^\circ$ is visible, while V is sputtered in a much broader distribu-

Element	SBE [eV]	ρ [g/cm ³]
SRIM		
V	5.33	5.96
C	7.41	2.25
TRIDYN		
V-C	6.37	4.11

Table 6.1: Table presenting the input parameters (electron density and SBE) for SRIM and TRIDYN simulations

Element	E_{sp} (SRIM) [eV]	E_{sp} (TRIDYN) [eV]	Y_{tot} (SRIM)	Y_{tot} (TRIDYN)
V	29.52	8.23	0.50	0.103
C	7.12	12.40	0.06	0.113

Table 6.2: Table presenting the results of the SRIM and TRIDYN simulations for the average energy E_{sp} and the total sputtering yield Y_{tot} of the sputtered particles.

tion.

However, in the case of the SRIM simulations, the results are striking. Y_{tot} and E_{sp} differ strongly for the elements. This is not expected for compound targets [Nei08]. Moreover, the simulated angular distribution of C deviates significant from the expected near-cosine distribution.

The here presented results are similar to findings of [Nei08]. They compared simulations of the sputter process at the target position from a Ti-B compound target using the above-mentioned approaches. In case of single-element targets, large differences of Y_{tot} and E_{sp} was additionally found for this system. A narrow distribution of B atoms along the target normal was found. The results of the TRIDYN simulations showed however more realistic angular distribution.

The differences in the simulation results are explained by the fact that TRIDYN covers the dynamic processes at the target surface. The collision process at a compound target involves three atoms with different masses, which is only covered by the TRIDYN simulations. Although the TRIM simulations have the advantage of reliable input parameter, the simulated angular distribution of C is not realistic. [Mra13] investigated sputtering from a Cr-Al-C compound target. They found out, that by using unknown SBE the result is less error-prone compared to simulations, which neglect the interaction of atoms with differences in mass.

Therefore, all simulations of the sputter process at the target position, which are pre-

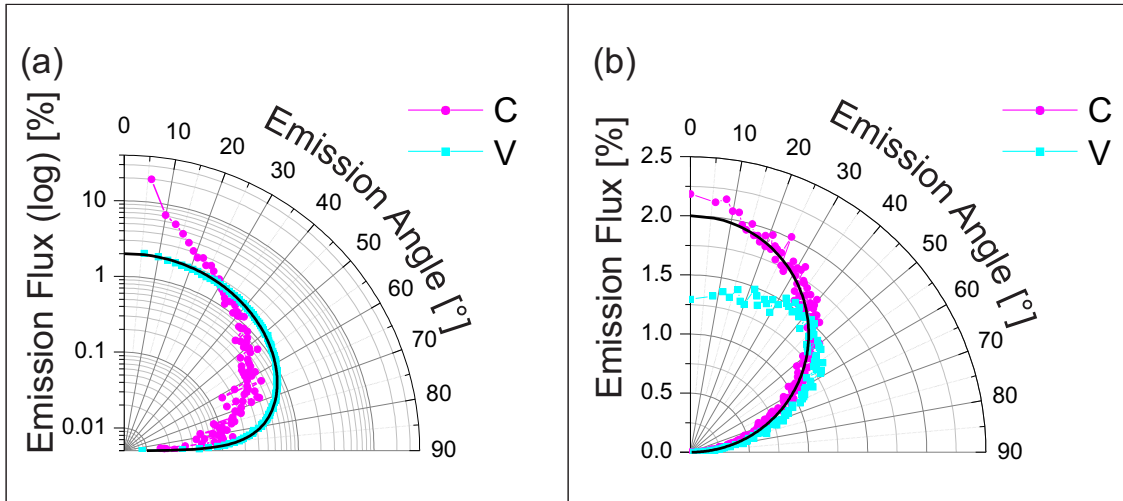


Figure 6.1: Emission Flux of C and V atoms depending on the emission angle from (a) SRIM simulation (Note the logarithmic scale) and (b) TRIDYN simulation. 0 ° correspond sputtering along the normal direction of the target

sented in the following chapters, will be performed using the software TRIDYN. In Chap. 9, the thin film formation at different DC powers is investigated. Simulation of the sputter process at the target were performed for different Ar^+ ions energies. Furthermore, the results of the simulations at a DC Power of 200 W are used as an input parameter for calculations of the gas transport. These calculations will be outlined in the next section.

6.2 Travel of the particles through the gas phase

The particles, sputtered from the target position, travel through the gas phase to the substrate. Their motion is influenced by collisions with the gas atoms.

The simulations of the motion of the particles through the gas phase were performed based on the equations presented in section 1.1.3 using the software tool SIMTRA [Aek08]. The program is based on Monte-Carlo simulations.

As input, the results of the TRIDYN simulations are used. However, SIMTRA is optimized for SRIM output files. This was overcome, by adapting the TRIDYN output file to the syntax of the SRIM output file.

For a realistic description of the sputter process, it is essential to include the sputter chamber geometry. The flux of the sputtered atoms is e.g. influenced by the walls of the vacuum vessel [Aek08].

Fig. 6.2 (a) represents the chamber design used for the simulations. A substrate with radius of 20 mm at a target-substrate distance of 12 cm was used as an input parameter.

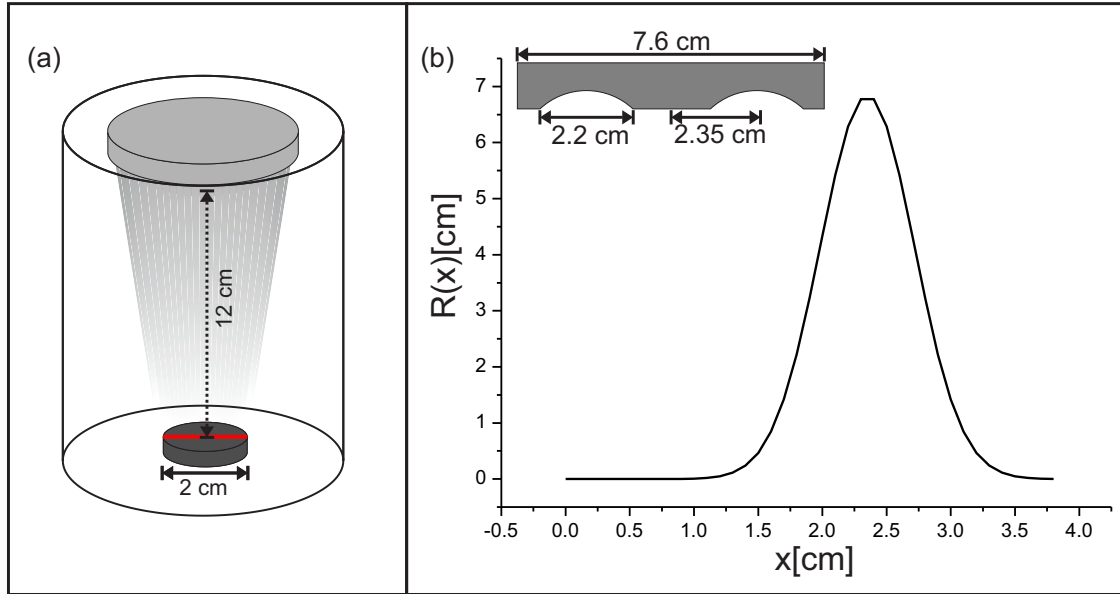


Figure 6.2: (a) Scheme of sputtering chamber used for the SIMTRA simulations. (b) Race track approximated by Gaussian function. $x=0$ corresponds to the center of the target.

As presented in Chap. 1, a racetrack is generated due to the secondary electrons trapped in the magnetic field. Hence the particles are mainly sputtered in this region. The race track $R(x)$ of the target was calculated using Eqn. 1.2 with $\mu = 2.35$ cm and $\sigma_G = 0.36$ cm. $R(x)$ is presented in Fig. 6.2 (b), where $x=0$ corresponds to the center of the target.

A further input parameter for the simulations is the amount N_0 of sputtered particles leaving the target. N_0 needs to be sufficiently high to ensure good statistics. In addition, N_0 should be small due to the high computational effort.

Due to the geometry of the sputter chamber, only a part N of the sputtered particles N_0 will arrive at the substrate. In the following, N is roughly estimated for the case, that no collisions in the gas phase occur.

The probability of the particles to arrive in the middle of the substrate is influenced by their emission angle at the target position. This is schematically shown in Fig. 6.3 (a).

If the particles do not collide in the gas phase, only the particles with in the angular distribution $\Delta\beta$ of 6-16 ° will arrive at the substrate. This area is shaded in gray in Fig. 6.3 (b). Hence only $\approx 10\%$ of the particles sputtered at the target position fulfill this condition. However, this is an overestimated. For the simulations, SIMTRA chooses randomly for each simulated particle a certain emission angle β (from the TRYDIN results). A particle, leaving the target at point A in Fig. 6.3 with β_{min} will not arrive in the middle of the substrate.

In general, for each particle leaving the target, only a $\Delta\beta$ of around 5-7 ° exists for which

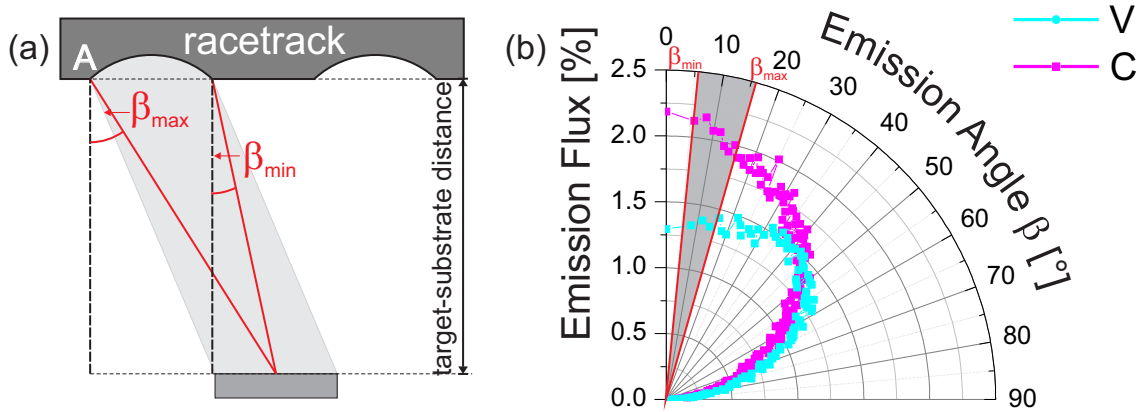


Figure 6.3: (a) Scheme of the sputter process, showing the maximum and minimum emission angle β_{max} and β_{min} . (b) Emission Flux of C and V atoms depending on the emission angle from TRIDYN simulation (s. Chapter 9). The angular range given by β_{max} and β_{min} is indicated.

it can arrive at the substrate. Consequently, only around 4% of the particles will have a high probability to reach the substrate.

Additionally SIMTRA chooses for each simulated particle a position x on the target. The probability, if the particle leaves the target is given by $R(x)$. This reduces further the amount of arriving particles to around 1-2%. Therefore N_0 was set to 10^7 sputtered particles to ensure good statistics.

The simulations were performed independently for C and V. This approximation is valid, since the sputtered atoms collide mostly with the Ar atoms. As stated in Sec. 1.1.3, collisions between sputtered particles are negligible small.

SIMTRA calculations were performed for the two working gas pressures $p=0.2$ Pa (LP) and $p=4$ Pa (HP). The results are presented in Chaps. 9 and 10.

6.3 Summary

Simulations of the sputter process from a compound target can be performed by splitting the entire process in two separate simulations.

Calculations at the target position are strongly influenced by dynamical interactions at the target surface. Although important input parameters are not reliably known, the process is dominated by the interaction of different constituents with varying mass. Therefore, the nascent angular distribution, the average energy of the sputtered particles and their total sputter yield were simulated using the software tool TRIDYN.

The results were used as input for calculations of the gas transport of C and V using the software tool SIMTRA. SIMTRA calculates the collisions of the sputtered particles in the

gas phase. Moreover, it covers geometrical effects, since the sputter chamber geometry is a necessary input parameter.

By combining those two tools, a realistic simulation of the sputter process can be performed. The results of the simulations are presented and discussed in Chaps. 9 and 10.

Part III

Monitoring the film formation

7 Optimization of the *in situ* XRR measurement

For a standard X-ray reflectivity (XRR) measurement after thin film deposition, the incident angle α_i is scanned while simultaneously changing the exit angle of the outgoing beam α_f with respect to the sample surface (s. Sec. 3). The specular reflected beam with $\alpha_f = \alpha_i$ is measured.

Two measurement types were successfully performed to monitor the specular beam during the growth:

(1) *Scanning* measurements:

A *standard* XRR measurement is performed. The incident angle α_i is scanned. The specularly reflected beam with $\alpha_f = \alpha_i$ is measured. The z-component of the scattering vector \mathbf{q} is changing with angle and time. The scan is repeated until e.g. the deposition of a film is finished [Chi97].

(2) *Stationary* measurements at a fixed angular position:

The specular intensity is monitored at a fixed angular position $\alpha_{fix} = \alpha_i = \alpha_f$, i.e. q_z is constant during the measurement. [Lou94, Pev05, Lee08].

For magnetron sputtered polycrystalline coating materials such as VC_{1-x}/a-C, several challenges have to be overcome during such an *in situ* measurement. For industrial applications, film thicknesses of hard coatings in the micrometer regime are desired, leading to sputtering processes with high deposition rates (nm/s) and long deposition times (up to hours). The roughness of the thin film can vary significantly with time in the Angstrom to nanometer regime [May06].

Furthermore, interruptions of the growth process should be avoided, since they can lead to microstructural changes due to diffusion process at high growth temperatures or renucleation processes at the following deposition [Wue11, Kag04].

Therefore, experimental data of both measurement types during sputter deposition were collected under identical growth conditions (s. Sec. 5.2). Fig. 7.1 (a) and (b) show experimental data of both *in situ* measurement types during the first 400 s of V-C deposition.

The *in situ scanning* measurement of the LP-b(3.5) is presented in Fig. 7.1 (a). The scan was performed from small to large q_z values. During the deposition, the coating thickness increases while scanning q_z towards larger values. The deposition process started at $q_z \approx 0.025 \text{ \AA}^{-1}$, marked by red line.

The curve exhibits the typical features of a standard XRR measurement. As shown in Sec. 3, three characteristic features namely the critical angle, oscillations and the slope of a *standard* XRR curve, provide information about thickness, roughness and density of

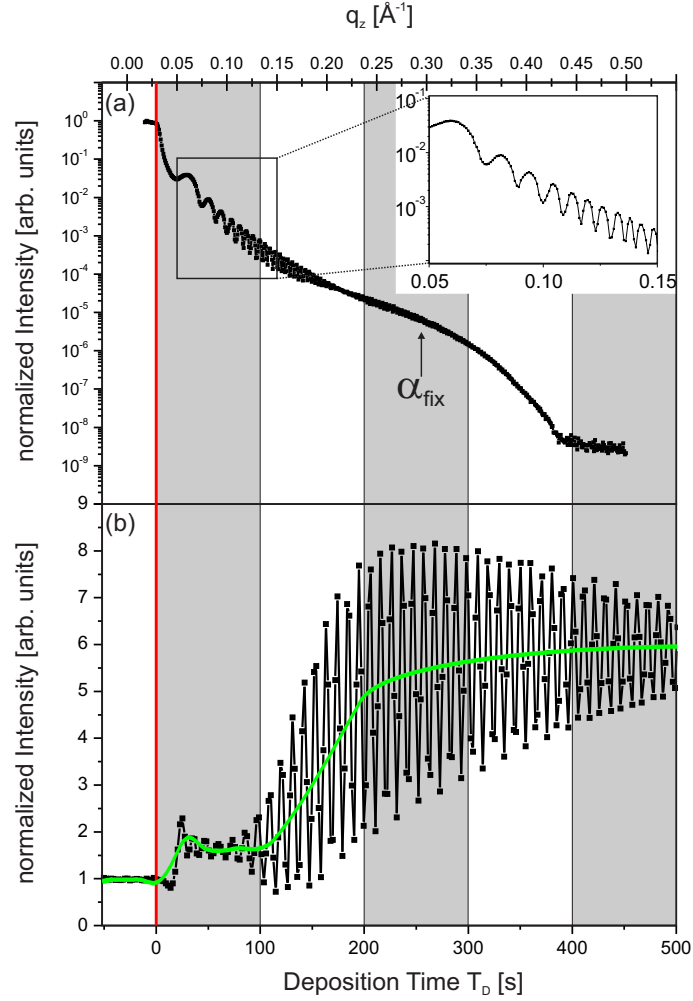


Figure 7.1: Measurements of two *in situ* XRR curves of VC_{1-x} on Si(100) for the first 400 seconds of deposition. The time axis corresponds to both curves. The gray boxes indicate time intervals of 100s. At $t=0$ s (red line) the plasma was ignited. (a): *Scanning* measurement. (b) *Stationary* measurement at the fixed angular position $\alpha_{fix} = 1.6^\circ$ (corresponding to $q_z(\alpha_{fix}) = 0.283 \text{ \AA}^{-1}$). The position of α_{fix} is denoted by an arrow in (a).

the thin film.

For $LP-b(3.5)$ the critical angle is located at $q_z \approx 0.031 \text{ \AA}^{-1}$. This is in good agreement with the expected value for the Si substrate since only a low amount of material was deposited at α_c .

As highlighted in Fig. 7.1 (b) (inset), the period of the Kiessig fringes decreases with increasing q_z , i.e. increasing film thickness. For larger film thicknesses, a shorter period

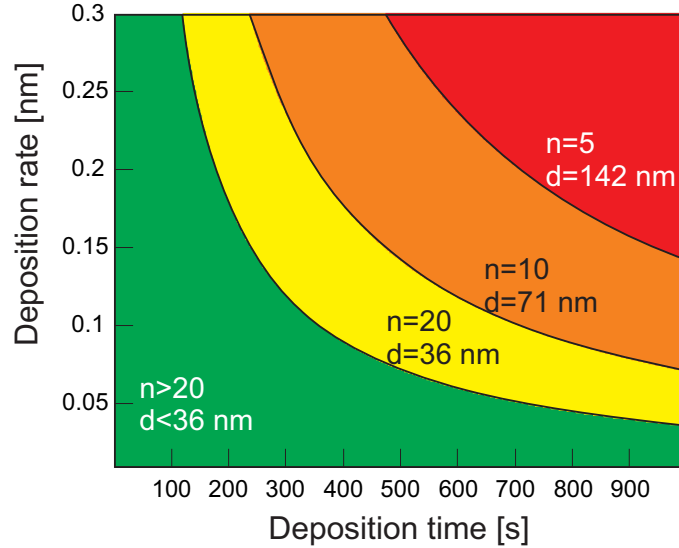


Figure 7.2: Number n of scanning points per Kiessig fringe at 10 keV X-ray energy and $\Delta\alpha = 0.005^\circ$ for different deposition rates and times. The lines correspond to fixed n values and their corresponding film thickness d . For more details s. text.

is expected from Eqn. 3.19 (s. Chap. 3).

Fig. 7.1 (b) shows the *stationary* measurement at a fixed angular position of $\alpha_{fix} = 1.6^\circ$ of *LP-a* (3.5). The corresponding q_z -value is indicated by an arrow in Fig. 7.1 (a). Growth oscillations are well resolved during the entire deposition time. The period varies only slightly, while the amplitude and the mean value of the intensity (green line) show significant time-dependent changes.

The main difference between both measurement types is the ability to resolve the growth oscillations, which is influenced by the high deposition rate and the long deposition time. As shown in Chap. 3, the thickness of the film is related to the period of the Kiessig fringes. For the *angle-dependent* XRR measurements in this work a constant angular step between subsequent data points was chosen ($\Delta\alpha = 0.005^\circ$). Taking $\Delta\alpha$ into account, the number n of scanning points per Kiessig fringes can be calculated.

In Fig. 7.2, n depending on the deposition time and rate is presented. Here the thickness of the film was calculated as the product of deposition rate and time.

For $n < 5$, the Kiessig fringe is under-sampled and hence the period can not be reliably determined. For $n > 5$, the period is well resolved in case of perfectly flat films.

However, by adapting $\Delta\alpha$ to lower values, the growth oscillations can be resolved even at larger thicknesses. For optimization of the *scanning in situ* measurements, the distance $\Delta\alpha$ of the data points needs to be constantly adapted to resolve the growth oscillations. This adaptations will be limited by the experimental precision of the diffractometer for very large thicknesses.

Moreover, sample properties will influence the choice of $\Delta\alpha$. Already a roughness of the film below 1 nm can lead to a damping of the Kiessig fringes. Hence, the period might be not well resolved even in case of $5 < n < 20$. For very rough films, this might even be the case for $n > 20$. Since roughness of the film leads to a decrease in the specular intensity, Δt has to be increased for large α_i to account for a sufficient intensity.

Those problems can be overcome by measuring at small α_i .

For *stationary* measurements, α_i is fixed. Here, the growth oscillations are well resolved, even for larger coating thicknesses and roughnesses. Hence, *stationary* measurements have advantages in case of polycrystalline thin films deposited with high deposition rates and long deposition times. Furthermore, there is no time loss due to motor movement.

In case of *stationary* measurements, Δt is restricted only by the detector read-out. The intensity of the specularly reflected beam is high. Therefore the smallest Δt can be chosen. However, since additionally the diffuse scattering was measured (s. Chap. 5), the lower limit of $\Delta t = 1$ s was chosen to measure a sufficient scattering signal.

For this Δt , the growth oscillation in the specular beam were measured with at least $n = 7$ data points. For this measurement type, a complete damping of the amplitudes occurs only for very high roughness of the film. Therefore, the choice of $\Delta t = 1$ s is adequate for the here investigated films.

For a detailed understanding of *stationary* measurements, simulations were performed. They will be discussed in the next chapter.

8 Simulation of the *in situ* XRR curves

For understanding the origins of the time-dependent changes of the *stationary* XRR measurements, simulations are performed.

In this work, the measured intensity is analyzed using the Parratt algorithm [Par54], which is applied to time-dependent thin film systems. Based on this algorithm, a rule of thumb is given for the determination of the thickness increase during growth. Furthermore, the influence of the experimental resolution is discussed.

8.1 Parratt algorithm for growing films

The *Parratt-Algorithm* is widely used for the simulation and fitting of *scanning* XRR curves of thin films after the deposition [Par54]. It is an recursive algorithm which gives the exact description of the specular XRR curve.

The thin film is described by an electron density depth profile $\rho_e(z)$. For applying the Parratt-Algorithm, $\rho_e(z)$ is sliced into a stack of $j = 0, 1, \dots, N$ layers. This is schematically shown in Fig. 8.1. Each layer has a mean electron density $\langle \rho_e \rangle(z_j)$, where z_j is the distance of the layer j to the sample surface at $z_0 = 0$. $j = 0$ corresponds to the layer above the sample surface.

During the *in situ* experiment, the electron density profile $\rho_e(z, t)$ of the growing film changes with deposition time. $n_j(t)$ is the time-dependent refractive index of the layer j , which is directly proportional to the mean electron density $\langle \rho_e \rangle(z_j)$ of the layer.

Therefore, the z-component of the wavevector

$$k_j^z(\alpha, t) = k \cdot \sqrt{n_j(t)^2 - \cos^2(\alpha)}. \quad (8.1)$$

is also time-dependent.

Please note that in case of *scanning measurements* α is changing in time, too.

$r_{j,j+1}(\alpha, t)$ and $t_{j,j+1}(\alpha, t)$ are the time-dependent Fresnel coefficients:

$$\begin{aligned} r_{j,j+1}(\alpha, t) &= \frac{k_j^z(\alpha, t) - k_{j+1}^z(\alpha, t)}{k_j^z(\alpha, t) + k_{j+1}^z(\alpha, t)} \quad \text{and} \\ t_{j,j+1}(\alpha, t) &= \frac{2 k_j^z(\alpha, t)}{k_j^z(\alpha, t) + k_{j+1}^z(\alpha, t)}. \end{aligned} \quad (8.2)$$

Hence during growth of the sample, the amplitude of the reflected $E_{r,j+1}(\alpha, t)$ and transmitted X-ray $E_{t,j+1}(\alpha, t)$ for each interface at z_j change with time.

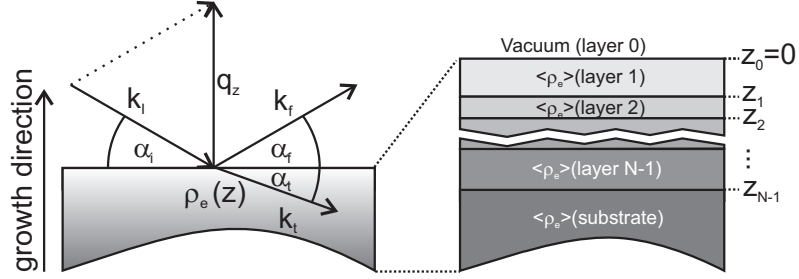


Figure 8.1: The sample is sliced into a virtual stack of layers j with height z_j . This virtual stack is used for the calculation of the XRR curve. More details s. text.

The ratio $X_j(\alpha, t) = E_{r,j}(\alpha, t)/E_{t,j}(\alpha, t)$ is derived recursively for each layer by

$$X_j(\alpha, t) = e^{-2i k_j^z(\alpha, t) z_j} \frac{r_{j,j+1}(\alpha, t) + X_{j+1}(\alpha, t) e^{-2i k_{j+1}^z(\alpha, t) z_j(t)}}{1 + X_{j+1}(\alpha, t) r_{j,j+1}(\alpha, t) e^{-2i k_{j+1}^z(t)(\alpha, t) z_j(t)}}. \quad (8.3)$$

Since the substrate is assumed to be semi-infinite, no X-ray is reflected at the bottom of the sample, i.e. $R_N = 0$ and $X_N = 0$. The specular intensity I is calculated by

$$I(\alpha, t) = |X_0(\alpha, t)|^2 \quad (8.4)$$

As shown in chapter 3, in case of rough films, the diffuse scattering from the sample leads to a decrease in the specular intensity I .

For small roughnesses, the effective time-dependent Fresnel coefficient \tilde{r}_j is used:

$$\tilde{r}_j(\alpha, t) = r_j(\alpha, t) \cdot \exp[-2i k_j^z(\alpha, t) k_{j+1}^z(\alpha, t) (\sigma_j(t))^2], \quad (8.5)$$

where $\sigma^j(t)$ is the time-dependent r.m.s.-roughness of the layer j .

These general formulas allow describing the *scanning* as well as *stationary* measurement types. In the following we focus on the *stationary* measurements for the already discussed reasons in chapter 7.

8.2 Calculation of the rate of the thickness increase

As presented in chapter 7 in Fig. 7.1, one characteristic feature of *stationary* measurements are growth oscillations. In this section, we show how the period of these oscillations is related to the rate of thickness increase F_D of the thin film.

For that, we assume a simple one layer system ($N=2$). A V-C thin film grows on top of a Si substrate with $z_1(t) = F_D t$. For simplicity, changes in roughness and electron

density with time are neglected. In this case, all z-components of the wave vectors k^z are constant. Eqn.8.3 simplifies to

$$X_0(\alpha, t) = \frac{r_{0,1}(\alpha) + r_{1,2}(\alpha) \cdot e^{-2ik_1^z(\alpha)z_1(t)}}{1 + r_{1,2}(\alpha) \cdot r_{0,1}(\alpha) \cdot e^{-2ik_1^z(\alpha)z_1(t)}}. \quad (8.6)$$

Only the exponent is time-dependent. The specular intensity I is calculated via Eqn. 8.4.

For $\alpha_{fix} \gg \alpha_c$, the amount of the Fresnel coefficients $|r_{1,2}(\alpha)| \approx |r_{0,1}(\alpha)| = |r|$ and $|r^2| \ll 1$. Therefore the intensity is can be approximatd by:

$$I \propto 4 \underbrace{|r|^2}_A \sin^2(|k_1^z(\alpha)| F_D t + \Phi) = \begin{cases} \frac{A}{2} (1 - \cos(\omega t)), & \Phi = 0 \text{ for } \rho_2 > \rho_1 \\ \frac{A}{2} (1 - \sin(\omega t)), & \Phi = \frac{\pi}{2} \text{ for } \rho_1 > \rho_2 \end{cases}, \quad (8.7)$$

where ρ_1 is the electron density of the film and ρ_2 the electron density of the substrate.

This means that the specular intensity oscillates during the deposition. Fig. 8.2 (a) shows the simulated *in situ* XRR curve for the here used model assuming a constant $F_D = 0.22$ nm/s. Regular oscillations with constant τ are visible.

The oscillation period $\tau(\alpha) = 2\pi/\omega$ can be easily determined from the experimental data. The frequency $\omega = 2 |k_1^z(\alpha)| F_D$ is only influenced by F_D , since $|k_1^z(\alpha)|$ is constant at a fixed angular position. F_D can be calculated from the oscillation period τ by:

$$F_D = \frac{\pi}{|k_1^z(\alpha)| \tau(\alpha)}. \quad (8.8)$$

Eqn. (8.8) is not only valid for the here discussed model system, but also for more complex systems. For $\alpha_{fix} \gg \alpha_c$, the oscillation period is nearly independent of roughness changes, as shown by the simulations in Fig. 8.2 (b). Here, the same model as in (a) was used, but a linear increase in roughness from 0 Å to 3 Å ($\sigma(t) = 0.005$ Å/s · t) was assumed. For a better comparison, the simulated *in situ* XRR curve based on model (a) is shown (gray dotted lines). No changes in τ are detected.

Even large density variations have only a slight influence on τ .

Furthermore, this formula can be used for multilayer systems, as long as only the topmost layer is changing.

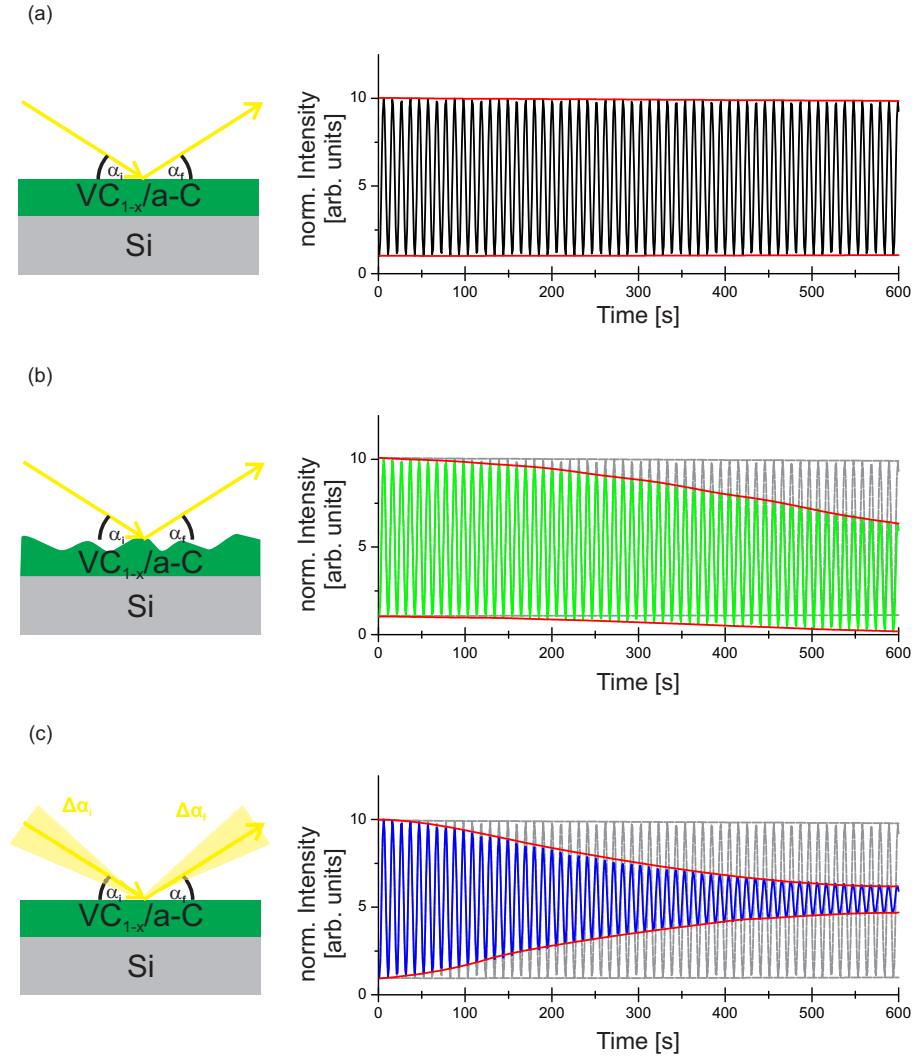


Figure 8.2: Simulation of *stationary* XRR curves at $\alpha_{fix} = 1.6^\circ$ for a deposition time $T_D = 600$ s with constant $F_D = 0.22$ nm of (a) a perfect flat V-C thin film ($(\sigma(t) = 0 \text{ \AA})$ and $\sigma_{q_z} = 0 \text{ \AA}^{-1}$), (b) a linear increase in roughness ($\sigma(t) = 0.005 \text{ \AA/s} \cdot t$) and $\sigma_{q_z} = 0 \text{ \AA}^{-1}$, and (c) including only a finite resolution ($\sigma_{q_z} = 0.002 \text{ \AA}^{-1}$, $\sigma = 0 \text{ \AA}$). The envelopes of all curves are highlighted by red curves. For better comparison, the *in situ* curve of model (a) is presented in (b) and (c) as gray dotted curve.

8.3 Influence of the experimental setup

In this section, we show how the experimental resolution influences the amplitude. The calculations in the previous sections assumed a parallel X-ray beam. In reality, the X-ray beam is divergent. σ_{q_z} is the so-called resolution element. It describes the area in reciprocal space which is illuminated by the X-ray beam and accepted by the detector [Pie04]. The smearing of a *standard* XRR curve with the specular intensity I_0 due to σ_{q_z} can be described by the resolution function R_{q_z} using a Gaussian function [Ped94]

$$R_{q_z}(q_{z0}, q_z) = \frac{1}{\sqrt{2\pi}\sigma_{q_z}} \cdot \exp\left(-\frac{1}{2} \cdot \frac{(q_{z0} - q_z)^2}{\sigma_{q_z}^2}\right) \quad (8.9)$$

where $q_z = 2 k^z$ is the z-component of the scattering vector of the reflectivity curve and q_{z0} the nominal setting of the instrument. The measured reflectivity I_{res} is given by

$$I_{res}(q_{z0}) = \int R_{q_z}(q_{z0}, q_z) I_0(q_z) dq_z. \quad (8.10)$$

Fig. 8.3 shows the calculated XRR curves for two deposition times $t = t_1$ and $t = t_2 \gg t_1$. The black dotted curves correspond to I_0 (no resolution element), the blue curves to I_{res} , considering a resolution element of $\sigma_{q_z} = 0.002 \text{ \AA}^{-1}$. The period of the Kiessig fringes at $t_2 > t_1$ is shorter due to the larger film thickness. Deviations from I_0 due to $\sigma_{q_z} = 0.002 \text{ \AA}^{-1}$ are larger for the film with larger thickness.

Fig. 8.2 presents two calculated *stationary* curves with (a) $\sigma_{q_z} = 0 \text{ \AA}^{-1}$, (b) including a linear increase in roughness from 0 \AA to 3 \AA ($\sigma(t) = 0.005 \text{ \AA/s} \cdot t$), and (c) including only a finite resolution ($\sigma_{q_z} = 0.002 \text{ \AA}^{-1}$, $\sigma(t) = 0 \text{ \AA}$). For comparison, the *stationary* curve of (a) is presented in (b) and (c) (gray-dotted line).

The envelope of (a) is almost constant. The roughness of the film leads to a slight decrease of the amplitude with time, while the resolution leads to a much stronger damping of the oscillations.

The reduction of the intensity I_0 due to the resolution element can be described by:

$$|I_0(t) - I_{res}(t)| \leq \xi \cdot |I_0(t) - \langle I_0(t) \rangle|, \quad (8.11)$$

where $\xi \ll 1$ is the parameter quantifying the tolerated deviation, and $\langle I_0(t) \rangle$ is the mean value of $I_0(t)$.

In the following, a rule of thumb is derived to estimate a certain critical thickness z_{crit} , at which the maximal deviation ξ is reached. Therefore, the simplified expression of I_0 (Eqn. (8.7)) for solving the integral in Eqn. (8.10). In case of the specular reflected beam, the frequency $\omega = 2 k_z F_D$ can be expressed by $\omega = q_z F_D$. For $\sigma_{q_z} \ll q_z$, the amplitude A is effectively small compared to $\cos(\omega t)$ in q_z . Hence the integration yields:

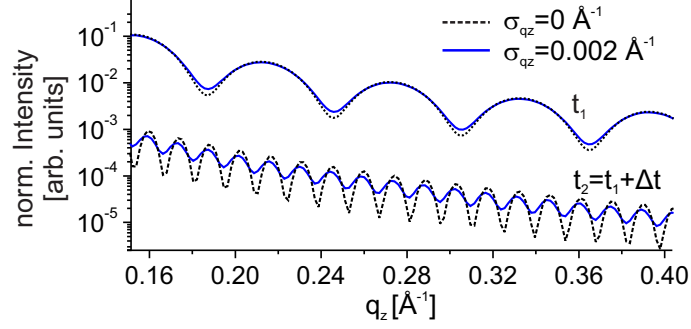


Figure 8.3: Simulation of *scanning* XRR curves after the deposition at $T_D = t_1$ and $T_D = t_2 \gg t_1$, using the resolution elements $\sigma_{q_z} = 0 \text{ \AA}^{-1}$ (dotted lines) and $\sigma_{q_z} = 0.002 \text{ \AA}^{-1}$ (continuous lines). The upper curve is shifted for a better comparison. At $t_2 = t_1 + \Delta t$, the influence due to σ_{q_z} increases.

$$\begin{aligned}
I_{res}(t) &= \int_{-\infty}^{\infty} \frac{A}{2} (1 - \cos(q'_z F_D t)) \cdot \frac{1}{\sqrt{2\pi}\sigma_{q_z}} \exp\left(-\frac{1}{2} \frac{(q_{z0} - q'_z)^2}{\sigma_{q_z}^2}\right) dq'_z \\
&= \frac{A}{2} \frac{1}{\sqrt{2\pi}\sigma_{q_z}} \cdot \left[\int_{-\infty}^{\infty} \exp\left(-\frac{1}{2} \frac{(q_{z0} - q'_z)^2}{\sigma_{q_z}^2}\right) dq'_z \right. \\
&\quad \left. - \int_{-\infty}^{\infty} \cos(q'_z F_D t) \cdot \exp\left(-\frac{1}{2} \frac{(q_{z0} - q'_z)^2}{\sigma_{q_z}^2}\right) dq'_z \right] \\
&= \frac{A}{2} \frac{1}{\sqrt{2\pi}\sigma_{q_z}} \cdot \left[\sqrt{2\pi} \sigma_{q_z} \right. \\
&\quad \left. - \frac{1}{2} \sqrt{2\pi}\sigma_{q_z} \cdot \left[e^{-\frac{1}{2} (F_D \sigma_{q_z} t)^2} \cdot \left(e^{iq_{z0} F_D t} - e^{-iq_{z0} F_D t} \right) \right] \right] \\
\Leftrightarrow I_{res}(t) &= \frac{A}{2} \left[1 - \cos(q_{z0} F_D t) e^{-\frac{1}{2} (F_D \sigma_{q_z} t)^2} \right] \tag{8.12}
\end{aligned}$$

The exponential function describes the modification of the envelope of the intensity due to the resolution. Inserting Eqn. (8.12) into Eqn. (8.11) yields

$$-2 \ln(1 - \xi) \leq (F_D t \sigma_{q_z})^2, \tag{8.13}$$

where $\langle I_0(t) \rangle = A/2$. Using $\ln(1 - \xi) \simeq \xi$ for $|\xi| \ll 1$, the following relation is found for

z_{crit} :

$$z_{crit} \leq \frac{\sqrt{2 \cdot \xi}}{\sigma_{qz}}. \quad (8.14)$$

Below z_{crit} , I_0 is a good approximation for the measured intensity. Above z_{crit} , the resolution has to be taken into account. For $z < z_{crit}$, variations in the envelope of the measured intensity can be directly related to microstructural changes of the sample. Above z_{crit} , only deviations larger than the resolution effect (s. Eqn. (8.12)) can be unequivocally attributed to the sample.

For our VC_{1-x}/a-C coatings, $\xi = 0.05$ is a reasonable value, taking into account the experimental error. With our experimental value of $\sigma_{qz} = 0.002 \text{ \AA}^{-1}$, the critical thickness is $z_{crit} \approx 16 \text{ nm}$. For a typical $F_D = 0.22 \text{ nm/s}$ this corresponds to a deposition time of $t = t_{res} = 68 \text{ s}$. Since the typical coating thickness for hard coating materials is of the order of micrometers, the intensity is significantly modified by the resolution nearly throughout the entire deposition time. Therefore we included resolution effects in the analysis of the *in situ* data as shown in the next chapters.

9 Influence of the DC power on the thin film formation

For sputter deposition, one main growth parameter is the applied DC power. It influences the nascent angular and energetic distribution of the sputtered particle. Furthermore, an enhancement of the DC power leads to a higher number of sputtered particles due to an enlarged number of ionized Ar [Wai78].

For single element targets, a linear relation between applied DC power and the thickness increase is reported [Wai78]. In this chapter, the influence of the DC power on the thin film formation of VC_{1-x}/a-C during the sputtering from a compound target is investigated.

Stationary *in situ* measurements were performed during the growth at different DC powers. From the period of the oscillation, the thickness increase at the different powers was calculated (s. Chap. 8).

Since the thickness increase is not only influenced by the deposition rate but additionally by e.g. porosity of the film, it is necessary to investigate the electron density changes at different DC powers. The analysis of the *in situ* data was supported by HRTEM image analysis and simulations of the sputtering process.

9.1 Stationary measurements

For the investigating the influence of the DC power on the thin film formation, most experimentalists follow this approach: Several films are deposited at different power. The thickness after film growth is measured e.g. by XRR measurements. From the thickness and the deposition time, the rate of thickness increase is determined [Wai78, Die05]. However, this approach is very time-consuming.

Monitoring the growth using *in situ* XRR gives the opportunity to reduce the number of samples. During the growth of the film, the *in situ* XRR oscillates. The period of the growth oscillation corresponds to the thickness increase (s. Chap. 8). Therefore, only one sample was grown, where the DC power was increased stepwise by $\Delta P = 25W$ every 250 s (s. Sec. 5.2).

Fig. 9.1(a) presents the integrated intensity of the reflected beam during the growth of $P - step$. For better visibility, the time intervals of 250 s with constant DC power are highlighted.

Except of the first oscillation, the period of the growth oscillations is constant for constant

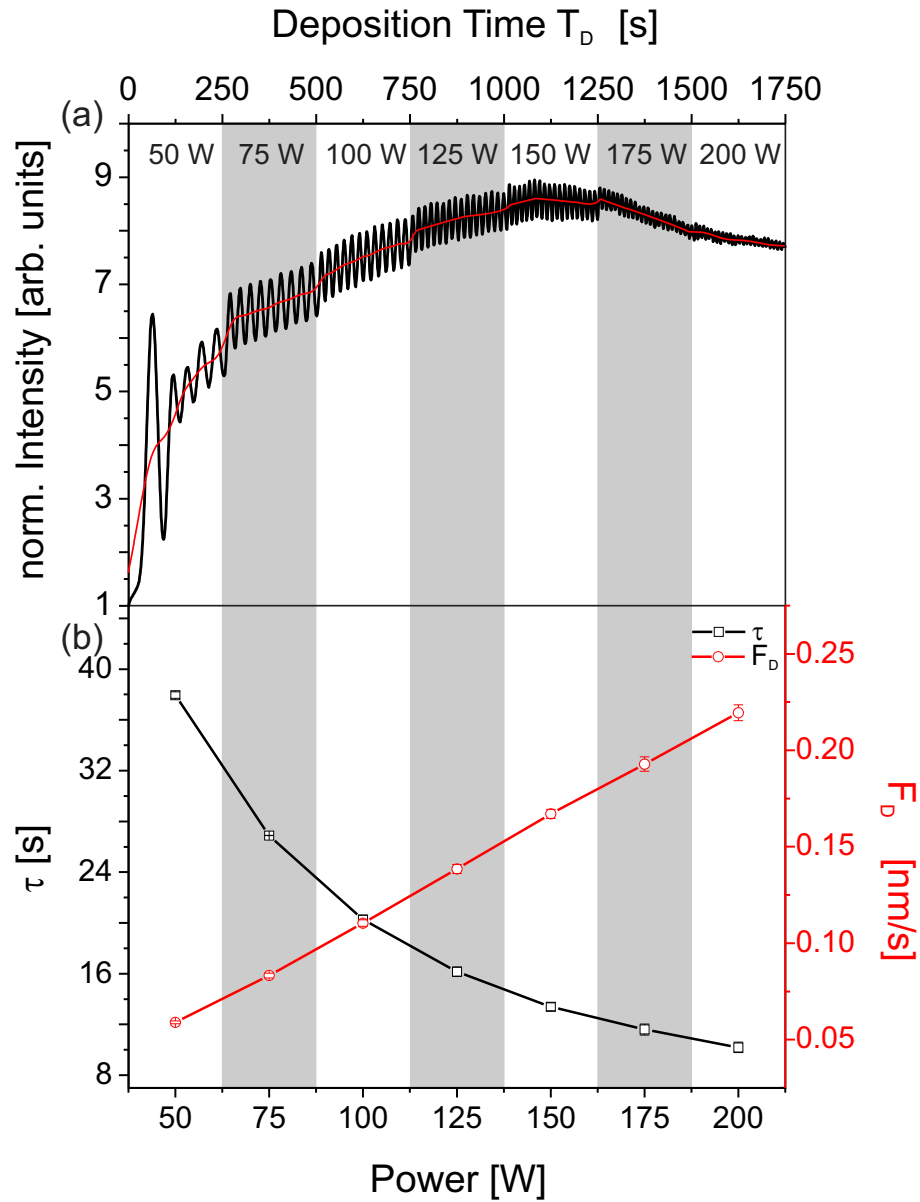


Figure 9.1: (a) *Stationary in situ* measurement during the growth of P – step. The mean intensity is marked by a red line. (b) Oscillation period T for different DC powers (black squares) and calculated F_D in nm/s from oscillation period (red circles).

DC power, but decreases with increasing power. For the first oscillation the growth is influenced by the pressure variations in the beginning of the sputter process. This more complex growth condition will be discussed in Chap. 11.

The mean value of the intensity is presented in Fig. 9 (a) by the red line. It represents

the mean from the upper and lower envelope of the curve. As can be seen, it increases up to $T_D < 1100$ s, afterward it decreases. In addition, slight jumps in intensity are visible when the power is increased.

For each power step the rate of the thickness increase F_D was calculated from the period of the growth oscillation, which will be described in the next section.

9.2 Determination of the rate of the thickness increase

Fig. 9.1 (b) summarizes the quantitative results for the period of the growth oscillations (black squares) and the calculated F_D (red circles) using Eqn. 8.8.

For the calculation of F_D , the period length needs to be determined.

Considering Eqn.8.7, it was shown, that the growth oscillations are proportional to a $\cos(\omega t)$ -function. To account for the intensity increase of the growth oscillations, the $\cos(\omega t)$ -function was weighted with the slope m of the mean value, resulting in following fit-function I_{fit} :

$$I_{fit} = I_{fit/0} + A \cdot \cos(\omega (t - t_c)) + m \cdot t, \quad (9.1)$$

where $I_{fit/0}$ is the axis intercept and A, t_c are the fit parameters for the $\cos(\omega t)$ -function. This procedure was used to fit all period lengths.

Fig. 9.2 shows the fit of the growth oscillations at $P=75$ W. The mean value is indicated by a green line. The fitting error of $\tau = 2\pi/\omega$ is smaller than 1%.

For the calculation, the electron density of the thin film is needed. For polycrystalline coatings, strong variations in ρ_e are possible due to porosity of the films (s. Chap. 2). However, for large angles $\alpha_{fix} \gg \alpha_c$, this influence of variations in ρ is negligible (s. Chap. 8). Therefore, for a constant value of $\rho_e = 5.1 \text{ g/cm}^3$ was used for the calculations. As can be seen in Fig. 9.1 (b), F_D is proportional to the applied DC power. This is the expected behavior, if the flux of the sputtered particles is proportional to the applied power. However, the thickness increase of the thin film is not necessarily equivalent to the deposition rate. At the same deposition rate, a porous film is growing faster in thickness than a film without voids. Therefore, it is necessary to investigate the effect of the DC power on the microstructure, which will be discussed in the next section.

9.3 Microstructural changes at different DC power

Changes in the electron density can be seen directly in the temporal changes of the amplitude of the *in situ* XRR measurement. However, they can be superposed by roughness changes as well as the resolution, as discussed in chapter 8.

The influence of the latter results in a continuous damping of the amplitude as shown in section 8.3. This counteracts to the observed constant amplitude at constant power

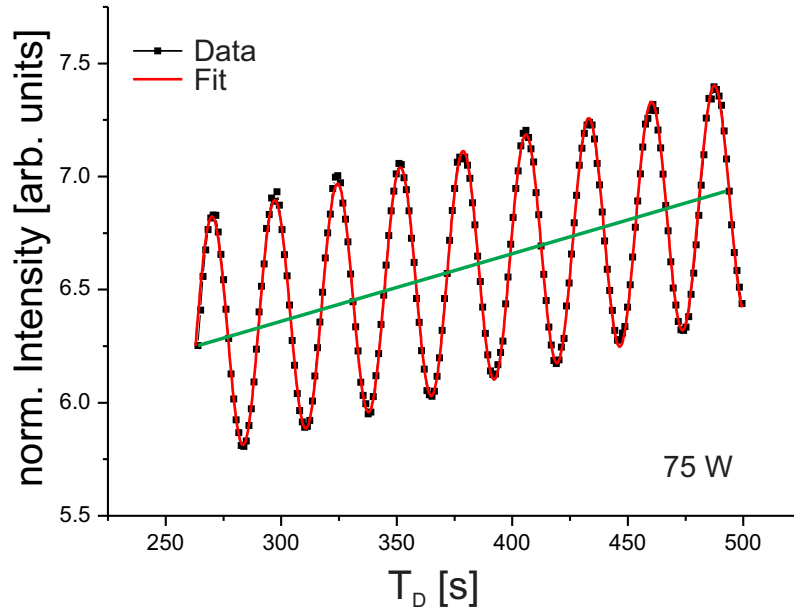


Figure 9.2: Fitting of the growth oscillation at 75 W. The mean value of the intensity is marked by the green line.

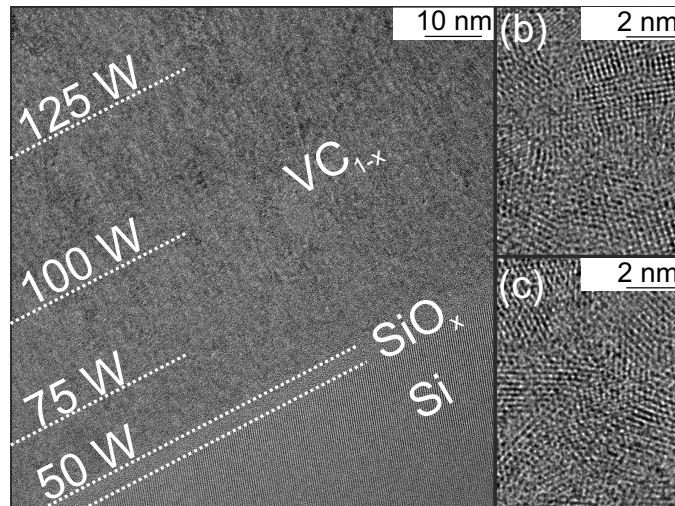


Figure 9.3: (a) HRTEM cross-section image of the thin film. Regions at DC power of 50 W (b) and 200 W (c) are highlighted for better comparison.

after the first growth oscillations and for $T_D < 1100$ s. For $T_D > 1100$ s the influence of the resolution is observed. However, the jumps in the amplitude, when the power is changed, are abrupt variations in the intensity and are hence due to microstructural or morphological changes.

In case of the jumps, simulations based on the Parratt-Formalism were performed, assuming only electron density variations (Chap. 8). An increase by 10 % in electron density per power-step was needed for achieving a satisfying agreement with the experimental data. This would result in a difference in electron density of 60% between the layers grown at 50 W and 200 W.

Such a large difference is not consistent with the HRTEM images of the film presented in Fig. 9.3 (a). Highlighted regions of the thin film at 50 W (b) and 200 W (c) show no major changes in the microstructure. Hence large density variations can be excluded. Therefore, the observed jumps in intensity have to be related to a smoothing of the film.

The observed increase of the mean value $T_D < 1100$ s is comparable with the abrupt intensity increase during the jumps. Hence the observed increase in the mean intensity for $T_D < 1100$ s must be dominated by a smoothing of the coating. The roughness decreases continuously at constant power up to $T_D < 1100$ s, and increases afterward. The increase of the mean value $T_D < 1100$ s is comparable with the abrupt intensity increase during the jumps. Hence the observed increase in the mean intensity for $T_D < 1100$ s must be dominated by a smoothing of the coating. The roughness decreases continuously at constant power up to $T_D < 1100$ s, and increases afterward. The sudden changes of the amplitude, when the power is increased, are related to a nearly instant reduction of the roughness of the film.

Since no significant changes in electron density were found, F_D is dominated by the increasing deposition rate due to higher DC power, and not by microstructural changes.

This result is in good agreement with the linear behavior of deposition rate and DC power found for single element targets. For a better understanding of the influence of the DC power during the sputtering from a compound target, simulations were performed. The results are presented in the next section.

9.4 Simulations of the sputtering process at different DC powers

The *in situ* measurements covered the range of DC power from 50 W to 200 W. The applied DC current influences the amount of Ar^+ ions impinging on the target surface, whereas the DC Voltage mainly influences the nascent angular and energetic distribution [Wai78].

Fig. 9.4 presents the experimental values for the current and the voltage at the different DC powers. As can be seen, both increase simultaneously.

For the investigation of the influence of the different applied voltage, simulations of the sputtering process at the target position were performed (s. Chap. 6). In this section, the results of the TRIDYN simulations for the maximum DC power of 200 W (Ar^+ energy of 310 eV) are compared to the calculations for the minimum DC power of 50 W (Ar^+ energy of 280 eV). The element-specific differences of the elements C and V in the nascent

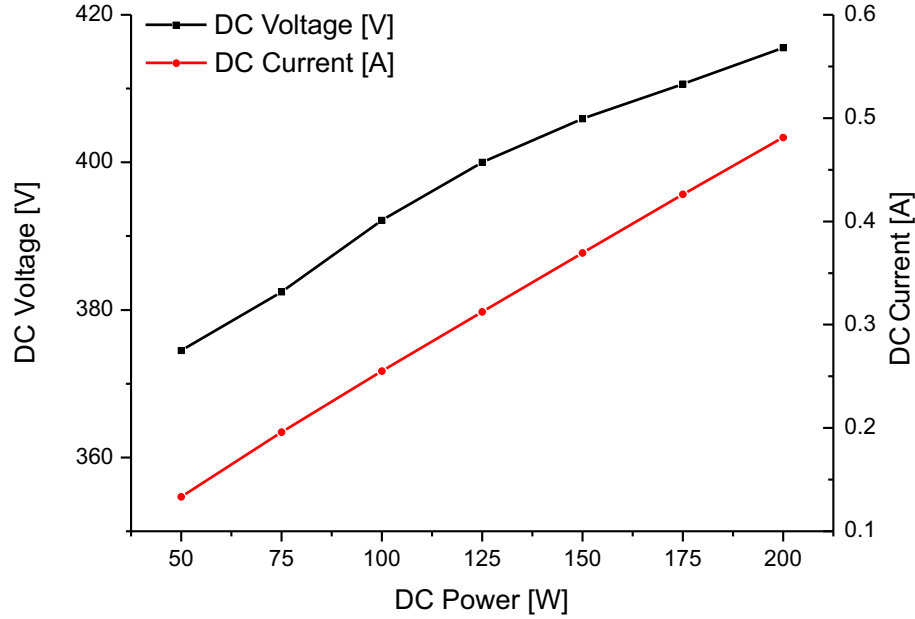


Figure 9.4: DC current and DC voltage at the different DC powers.

Element	E_{sp} (50 W) [eV]	E_{sp} (200 W) [eV]	Y_{tot} (50 W)	Y_{tot} (200 W)
V	7.83	8.23	0.090	0.103
C	11.66	12.40	0.099	0.113

Table 9.1: Table presenting the resulting average energy E_{sp} and the sputter yield Y of the sputtered particles at the DC power of 50 W and 200 W.

distribution will be discussed in more detail in Chap. 10.

Fig. 9.5 shows the simulated nascent angular and energetic distribution of the sputtered particles at the different DC power. Only negligibly small variations are visible for both elements.

Tab. 9.1 shows the result for Y_{tot} and E_{sp} at different DC power for C and V. For both elements, the parameters increase for higher DC power.

The E_{sp} of both elements is around 5 % higher at 200 W. The enhancement of 15% of the total sputter yield Y_{tot} seems significant. However, due to the geometry of the sputter chamber, only the particles with emission angles 6-16 ° have a high probability to arrive at the substrate (s. Chap. 6). Considering only this relevant angular region, the energy of the sputtered particles is only 1 % higher at 200 W, while the sputter yield is enhanced only by 3%. Both deviation are too small to account for significant changes in the electron density.

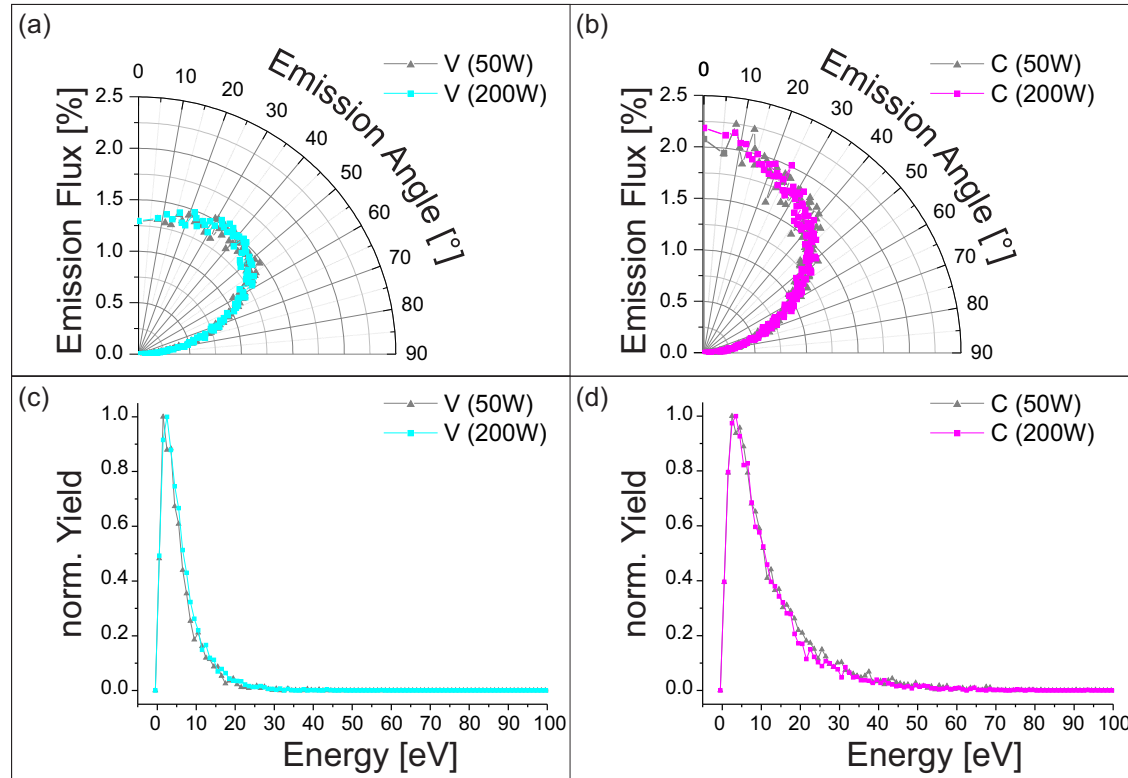


Figure 9.5: Nascent angular distribution of (a) V and (b) C at the DC power of 50 W and 200 W.

The TRIDYN results showed that the nascent angular and energetic distribution is only slightly influenced by the increase of the applied voltage. However, by increasing the DC power additionally the amount of Ar^+ ions impinging on the target is enhanced. This leads to an increase in the amount of the particles sputtered from the target. Besides the sputtering at the target, the transport of the particles in the gas phase has to be considered. Collisions of the particles in the gas phase influence the amount of arriving particles.

Therefore, simulations of the transport were performed using the software tool SIMTRA (s. Chap. 6). Due to the similarity of the results from TRIDYN, the calculations were restricted for the DC power of 200 W.

Simulations were performed with $N_0 = 10^7$ particles sputtered from the target. The working gas pressure $p = 0.2$ Pa was used as input parameter.

In Tab. 9.2 the results of the SIMTRA simulations are presented. In addition, the calculated energy-dependent mean-free path (MFP) for both elements using the results from TRIDYN (s. Sec. 1.1.3) is shown.

The average final energy, E_{final} , of particles arriving on the substrate deviates only slightly

Element	N/N_0	$E_{final}(N_0)$ [eV]	MFP [cm]
V	0.0142	8.02	18.44
C	0.0155	11.51	20.11

Table 9.2: Results of the SIMTRA simulations: Fraction of the sputtered particles arriving on the substrate N/N_0 for $N_0 = 10^7$ sputtered particles from the target and the average final energy E_{final} . The energy dependent mean free path at $p = 0.2$ Pa was calculated using the average energy E_{sp} of the sputtered particles, determined by TRIDYN simulations.

from the initial energy of the particles leaving the target. For both elements, N/N_0 is around 1 %.

The calculated (MFP) for both elements is larger than the target-substrate distance. Therefore almost no collisions are expected.

This explains well the results of the SIMTRA simulations: The final energy E_{final} is only slightly decreased, since the particles don't lose energy in collisions. In Chap. 6, the fraction N/N_0 for the given sputter chamber geometry was estimated. In case that the sputtered particles do not collide on their way in the gasphase, approximately 1% of the particles arrive on the substrate. This is in good agreement with the results of the simulations.

The simulations show that an enhancement of the DC voltage leads only to slight variations in the nascent distribution. An increase in DC current enhances the amount of impinging Ar^+ ions on the target and consequently the amount of sputtered particles at the target position. Due to the large MFP at the low pressure, no collisions take place. Therefore, the amount of particles arriving at the substrate is proportional to the amount of sputtered particles. The dominating process when changing the DC power is hence the increase of Ar^+ ions impinging on the target. This explains well the observed linear relation between the deposition rate and the applied power.

9.5 Discussion & summary

In this chapter, the influence of the DC power during the sputter deposition from a compound target was investigated.

For the investigation a fast and successful approach to determine the thickness increase was presented: Since the rate of the thickness increase can be directly extracted from the *in situ* data, the growth of only one sample was monitored and the thickness increase was directly extracted.

The observed jumps in intensity are dominated by a instant reduction of the roughness of the film, when the power is increased. These sudden changes are only accessible during *in situ* experiments.

The *in situ* measurements showed that a stepwise increase in ΔP leads to a stepwise

decrease in the oscillation period τ . From τ , the thickness increase F_D for the different DC powers was calculated. A linear dependency of ΔP and F_D was found.

No significant microstructural changes due to the power change were observed by HRTEM. The observed increase in the mean intensity of the *in situ* XRR curve must be dominated by a smoothening of the coating. The roughness decreases continuously at constant power up to $T_D < 1100$ s, and increases afterward. For higher thicknesses, this increase in roughness expected [Tho77, Sha10]. However, the smoothening of the film for the first power steps is contrary to this statement. This finding will be discussed in more detail in the next chapter.

Since no significant changes in electron density were found, F_D is dominated by the increasing deposition rate due to higher DC power, and not by microstructural changes.

This is in good agreement with the simulations of the sputter process. By increasing the DC power, the sputter process is mostly influenced by the enhanced DC current. This leads to a higher amount of Ar^+ ions and hence to more sputtered particles from the target with similar energetic and angular distribution. This is in accordance with the linear increase of the deposition rate with the DC power.

A similar finding has been reported by [Die05]. Here, a linear increase in deposition rate with increasing DC power during the sputtering from a $\text{Ge}_2\text{Sb}_2\text{Te}_5$ target was found. No changes in the microstructure were revealed by XRR measurements after growth.

[Pau02] investigated the influence of the DC power during the sputtering from a Cr_3C_2 compound target. The deposition rate was determined by SEM measurements. Here the deposition rate increased linearly with the DC power. Here the applied DC power influenced mostly the morphology, while the microstructure of the films was similar.

Furthermore, this result is in good agreement with the linear relation between power and deposition rate found for single element targets [Wai78].

10 Influence of the Pressure on the Thin Film Formation

The working gas pressure influences the mean free path (MFP) of the sputtered particles. Hence, the angular and energetic distribution of the sputtered particles depends also on their transport through the gas phase. Therefore, a simple way to influence the microstructure formation is the variation of the working gas pressure.

For this investigation two samples were deposited. For one sample, the working gas pressure was kept low to strongly reduce the collision rate. For the other sample, the pressure was set to a high value resulting in a high collision rate of the sputtered particles with the gas atoms.

The differences in the microstructure evolution were followed by *in situ* XRR measurements. Angle-dependent XRR measurements before and after growth are presented. Simulations based on the Parratt-Algorithm were performed to gain a quantitative understanding.

To understand the differences in the thin film formation at the different pressure, simulations of the sputter process were performed. The simulation show a change in the chemical composition. To verify this, XPS measurements were performed and analyzed. Furthermore, by using XRD, it was possible to gain insight in the pressure-induced differences in texture.

10.1 *In situ* XRR measurements at different working gas pressures

In this section, the thin film formation is monitored at *steady growth* conditions, where the pressure as well as the DC power are constant. The more complex plasma ignition period will be discussed in Chap. 11.

For the investigation of the influence of the working gas pressure, two samples were deposited.

For one sample, *LP-a* (3.5), the working gas pressure was reduced to $p = 0.2$ Pa. As shown in Chap. 9, for this pressure condition almost no collisions of the particles in the gas phase are expected. Since the sample is representative for all samples grown at this low pressure conditions, in the following the abbreviation *LP* is chosen.

The growth of *LP* is compared to the microstructure formation of the sample *HP-a* (in the following: *HP*). Here the working gas pressure was kept constant at $p = 4$ Pa, resulting in several collisions of the sputtered particles in the gas phase. The detailed sample description can be found in Chap. 5.

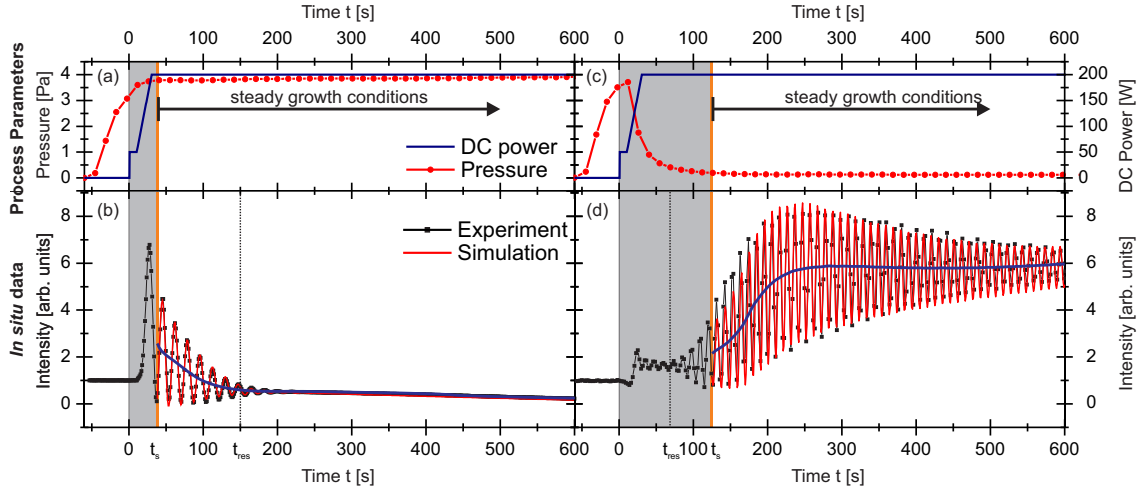


Figure 10.1: Selected process parameters ((a) and (c)) and *stationary in situ* measurements ((c) and (d), black dotted lines) at high and low working gas pressure, respectively. The mean value of the intensity is marked by a purple line. Simulations are presented with red lines. The orange line marks the begin of steady growth conditions.

Fig. 10.1 presents the *in situ* X-ray measurements, their simulations, and selected process parameters for both samples. The left column corresponds to *HP*, the right column to *LP*. The process parameters of both samples are presented in the upper row [(a) and (c)], the *in situ* X-ray measurements and their simulations in the lower row [(b) and (d)]. The main process parameters are the DC power (blue line) and the working gas pressure (red dots). In case of *HP*, the pressure is still slightly increasing after plasma ignition at $t = 0$ s. *Steady growth conditions* are reached at $t_s \approx 37$ s, marked by an orange line. For *LP*, the pressure is decreasing after plasma ignition, and *steady growth conditions* are reached at $t_s \approx 122$ s. The initial growth region with $t < t_s$ is shaded in gray. The experimental X-ray data are represented by black dotted lines, the mean intensity by purple lines. Their simulations (red lines) are shown for the steady growth region. Both *in situ* measurements show the typical growth oscillations, but it is instantly visible that the pressure has a strong influence on the structure formation.

In the *steady growth regime*, both *in situ* curves oscillate with constant period. At high pressure, $F_D = 0.132 \pm 0.003$ nm/s was estimated using equation (8.8). At low pressure, the estimated $F_D = 0.215 \pm 0.003$ nm/s is by nearly factor 2 larger than at high pressure. This difference is related to a higher collision rate at higher pressure, which will be discussed later.

As shown in Fig. 10.1, the envelope of the growth oscillations is very sensitive to pressure-induced changes of the microstructure. At high pressure, the amplitude decreases and is completely damped at $t > 200$ s. At low pressure, the amplitude increases up to $t = 200$ s,

then decreases slowly. For *HP*, z_{crit} is reached at $t_{res} \approx 150$ s, assuming a constant F_D in the initial growth phase. Therefore the damping of the growth oscillations for $t < t_{res}$ must be related to roughness changes. For *LP*, z_{crit} is reached at $t_{res}=68$ s. Since $t_s \approx 122$ s $> t_{res}$, i.e. the damping of the amplitude in the later growth region is strongly influenced by resolution effects even if roughness effects cannot be excluded.

10.2 Angle-dependent XRR measurements before and after growth

For the analysis of the *in situ* data, it is important to characterize the Si substrate, which are covered by a natural oxide layer. For the characterization, angle-dependent XRR measurements before growth were conducted.

Fig. 10.2 (a) shows the reflectivity measurement after data processing for the two Si substrates (colored lines). For fitting the data, a two layer system was assumed. On top of the Si substrate a 2.5 nm thick natural oxide layer was used as an input parameter. The roughness of the Si substrate and the oxide are around 0.4 ± 0.03 nm.

The fits, presented as black curves, are in good agreement with the experimental data.

The δ -profiles resulting from the fitting procedure are presented in Fig. 10.2 (b). The Si substrate and the oxide layer are indicated by gray boxes.

The measurements for both samples were performed at the DiffLab using an X-ray energy of 8.05 keV (Cu- K_α). The experimental data are presented in Fig. 10.2 (c), color.

Differences in both XRR curves are directly observed. The critical angle for the XRR curve at high pressure is located at lower angles compared to the measurement at low pressure. This indicates that the film, grown at high pressure has a lower electron density. Kissieg fringes are not observed for HP, but for LP. Additionally, the slope of HP decreases fast. Both indicates a strong roughness of the film, deposited at high pressure. The best fits of the curves are presented in Fig. 10.2 (c), black lines.

Since the samples were put in ambient conditions, besides the deposited VC_{1-x} thin film, a V_2O_3 layer ($\rho = 4.87 \text{ g/cm}^3$) was taken into account to achieve a good agreement with the experimental data.

In case of *HP*, a 80 nm thick layer with an electron density of $\rho_e = 3.8 \text{ g/cm}^3$ and a roughness of $\sigma = 2.5$ nm was used.

For *LP*, it was not possible to fit the curve assuming only one single layer. An interface layer was needed for achieving a good agreement with the experimental data. This interface layer is a result of the nucleation behavior and will be discussed in more detail in Chap. 11.

For the here discussed *steady growth conditions*, only the top most layer is relevant. For the fit, a 120 nm thick film with $\rho_e = 5.1 \text{ g/cm}^3$ and $\sigma = 0.4$ nm was used.

The resulting δ -profiles are presented in Fig. 10.2 (d). The oxide layer is denoted by a black arrow. Please note that the δ -values correspond to the X-ray energy of 8.05 keV.

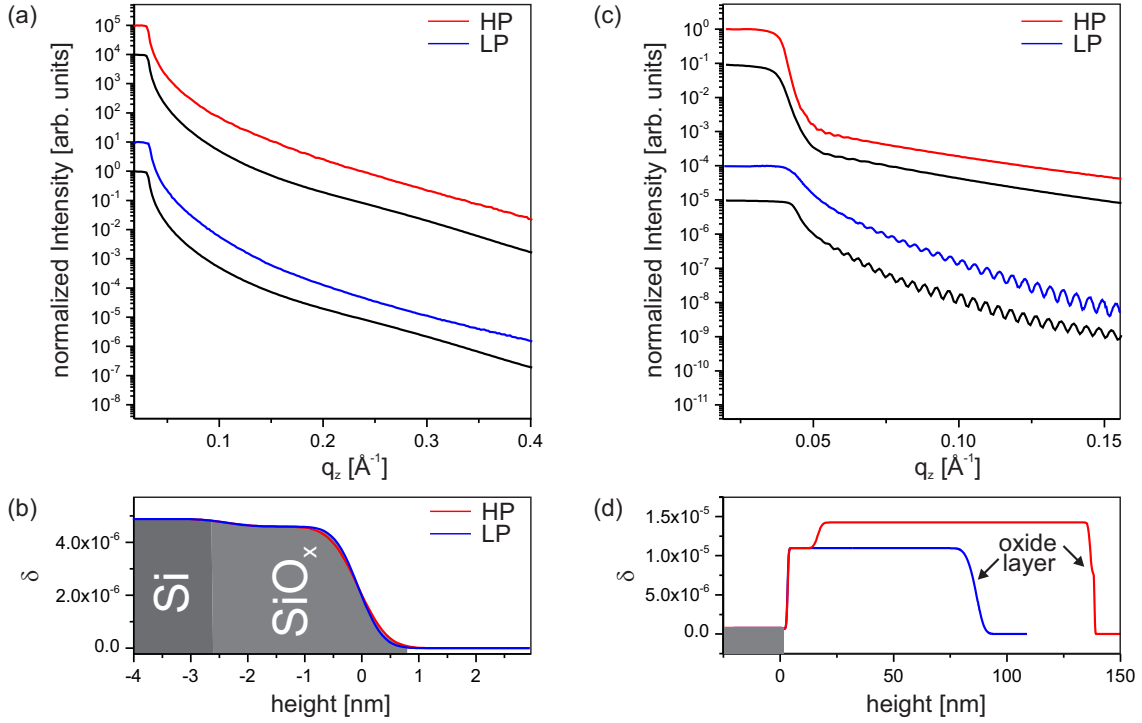


Figure 10.2: (a) XRR measurements (color) and the fits (black lines) of the Si substrates (using the X-ray energy of 10 keV). (b) δ -profile resulting from the fit. (c) XRR measurements (color) and the fits (black lines) of the samples after growth (using the X-ray energy of 8.05 keV (Cu-K α)). (d) δ -profile resulting from the fit. The gray box indicates the Si substrate with its natural oxide layer.

The XRR measurements of the Si substrate showed similar properties. The XRR curves after growth differ strongly for the two pressure conditions. The film at high pressure is a factor of two thinner, much rougher, and less dense than the film deposited at low pressure.

The here determined values of δ , σ and D are used as start and end values for the simulations of the *in situ* measurements. The latter are presented in the next section.

10.3 Simulations of the *in situ* XRR measurements

The details of the time-dependent microstructure formation were determined by fitting a simple model to the experimental data. The coating was assumed to be a layer with increasing thickness $D(t)$, where time-dependent variations in roughness $\sigma(t)$ and electron density $\rho(t)$ only happen at the growth front. In the following, time-dependent variations in electron density are described using $\delta(t)$.

For the simulation of the *in situ* XRR curves, the Parratt-formalism for growing films

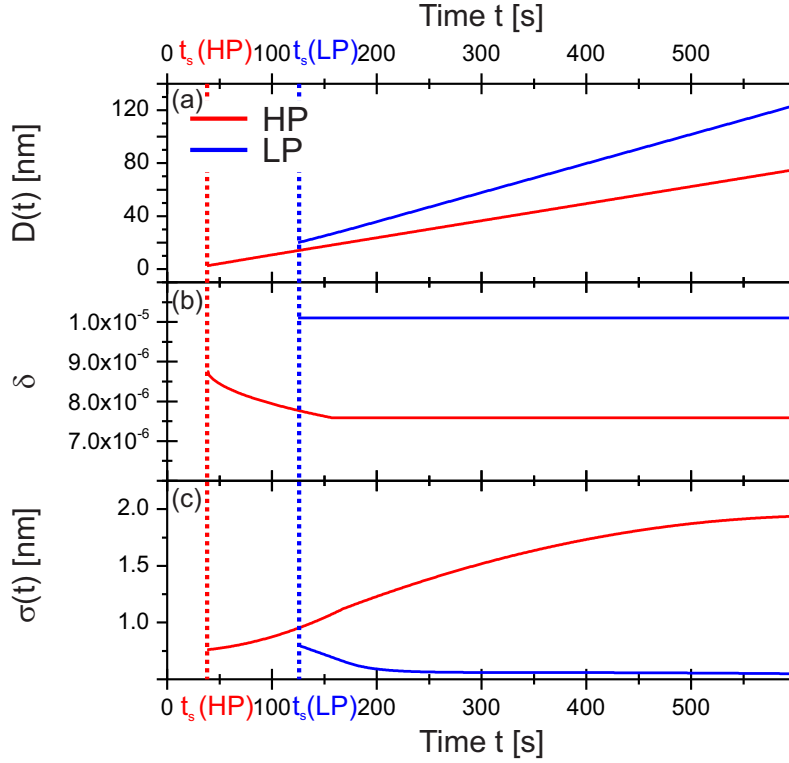


Figure 10.3: Simulation input for the stationary measurements: (a) thickness $D(t)$, (b) $\delta(t)$, (c) $\sigma(t)$. The point in time, t_s , when the *steady growth conditions* are reached, is indicated by dotted lines for both samples.

was used (s. Chap. 8). As start values for the fit procedure, the estimated $F_D(t)$, the average δ and σ determined from the XRR measurements before and after growth were used. $F_D(t)$, $\delta(t)$ and $\sigma(t)$ were optimized to fit the simulation to the experimental data. Within the model, both, $\delta(t)$ and $\sigma(t)$ influence the amplitude and the mean value of the intensity in a characteristic way. In our case, $\delta(t)$ and $\sigma(t)$ are continuous and vary only slowly compared to the oscillation period. Changes in $\delta(t)$, $\sigma(t)$ and $D(t)$ larger than 1% lead to deviation of the simulated data from the experiment. Since the results of the XRR measurements before and after growth were used as start points for the simulation, the values of $\delta(t)$, $\sigma(t)$ and $D(t)$ can be determined with an estimated precision of around 1%. The results are presented in Fig. 10.3.

As estimated, the thickness $D(t)$ of both films is increasing almost linearly with time. However, the slight decrease of 5% of $F_D(t)$ at high pressure could only be revealed by the fitting.

For LP, the expected decrease in $\sigma(t)$ of the film up to $t = 200$ s was confirmed. Although the amplitude for $t > 200$ s is mainly influenced by the resolution, a further

Element	E_{sp}	MFP	MFP	N/N_0	N/N_0
	[eV]	[cm]	[cm]	[%]	[%]
		(LP)	(HP)	(LP)	(HP)
V	8.23	18.44	0.92	0.0142	0.0027
C	12.40	20.11	1.01	0.0155	0.0026

Table 10.1: The average energy E_{sp} of the sputtered particles was determined by TRI-DYN simulations. From this, the energy dependent mean free path at $p = 0.2$ Pa and $p = 4$ Pa was calculated. Values for mass and radii are taken from the SIMTRA program. The fraction of the sputtered particles arriving on the substrate N/N_0 was simulated using SIMTRA.

slight smoothening process was determined by the fitting. For HP, a strong increase in roughness was found even after the complete damping of the oscillations.

For HP the fitting revealed a decrease in the mean electron density in the first 130 s of deposition. This might be related to the influence of the substrate on the nucleation behavior. At a certain coating thickness, this influence can be neglected. Consistent with this the mean electron density for LP was only determined at high coating thicknesses and is constant, as expected. To understand these differences in thin film formation at the different working gas pressures, simulations of the sputtering process were performed (s. Sec. 1). The results are presented in the following.

10.4 Simulations of the sputtering process at different gas pressures

In this section, the simulations of the sputter process at the different working gas pressure are presented. For that, the results of the SIMTRA simulations at $p=0.2$ Pa (s. Chap. 9) are compared with calculations at $p=4$ Pa. For both simulations, the amount of sputtered particles at the target position was set to $N_0 = 10^7$.

The results of the SIMTRA simulations are presented in Tab. 10.1. The calculated flux N/N_0 decreases with increasing pressure for both elements. Furthermore, the simulations predict a change in chemical composition from a C/V ratio of 0.9 at low pressure to $C/V = 1.1$ at high pressure.

The decrease in the calculated flux N/N_0 can be explained, considering the MFP. Tab. 10.1 presents the calculated energy-dependent MFP for both pressures using the results from TRIDYN (s. Sec. 1.1.3). As already stated in Chap. 9, the MFP at low pressure exceeds the target-to-substrate distance. Hence no collisions of the sputtered particles with the Ar atoms are expected. At high pressure, the MFP is strongly reduced and more particles are scattered to the side [Aba09].

The prediction of changes in the chemical composition are more striking. One might expect that the stoichiometry of the target is mirrored in the film composition.

For experimental verification of the change in chemical composition, XPS measurements

were performed on *LP-c(3.5)* and *HP-b*, which will be presented in the next section.

10.5 X-ray spectroscopy measurements

10.5.1 Qualitative analysis of the XPS spectra

For the analysis of the chemical composition, XPS measurements were performed in the UHV Analysis Lab. The experimental details can be found in chapter 5.5. Fig. 10.4 shows (a) the overview scan and (b) the region scans around the V2p and (c) C1s peaks for the sample grown at low (black) and high pressure (red). The photo emission peaks of the detected elements are highlighted in blue in Fig. 10.4 (a). The most intense peaks in the overview scan can be attributed to the V2p peak at 520 eV and to the C1s peak at 284 eV [Mou92].

Detailed region scans were performed (s. Fig. 10.4 b),c)) for both elements. The V2p_{1/2} peak position is found at 521.6 ± 0.5 eV, the V2p_{3/2} at 514.1 ± 0.5 eV.

The carbon peak is split into two peaks due to different chemical bonding: The peak at 284.5 ± 0.5 eV can be attributed to C-C bonding, the one at 282.9 ± 0.5 eV is connected to the V-C bonding. In case of the low pressure sample, the intensities of the peaks corresponding to C-C and C-V are comparable. For the high pressure sample, the V-C peak is approximately twice as intense as the C-C peak.

The peak positions both for V and C are in good agreement with values found in the literature for V-C. The V2p_{1/2} peak position was found e.g. at 521.3 eV for single crystal [Bra75], at 520.7 eV for VC thin films deposited by pulsed-laser deposition [Teg09] and 520.9 ± 0.2 eV for V-C films prepared by carburization of V₂O₅ [Cho99]. The V2p_{3/2} peak was reported at the following positions: 513.8 eV [Bra75], at 513.1 eV for V-C thin film prepared by RF-sputtering [Lia05] and 513.8 eV [Teg09]. The C peak, connected to the V-C bonding was found at 282.2 ± 0.2 eV [Cho99], at 282.5 eV [Lia05], at 283.1 eV [Teg09]. The C peak, connected to C-C bonding, was reported at e.g. 284.5 eV [Lia05], 284.3 eV [Cho99].

Besides the main elements V and C, traces of other elements are detected. Ti impurities are detected around a binding energy of 461 eV (Ti2p_{3/2}) and 455 eV (Ti2p_{1/2}) [EM10b]. The peaks at 242 eV and 244 eV can be attributed to Ar2p_{1/2} and Ar2p_{3/2}. Additionally a peak due to nitrogen impurities can be found at 397.3 eV. The peak at 531.2 eV can be related to the oxygen O1s peak. [Mou92].

The metallic impurities can be attributed to the small contamination of the target. The impurities of the gas might be related to a small contamination of the gas lines or to a certain oxygen content in the target.

10.5.2 Quantitative analysis of the XPS spectra

For the quantitative analysis of the XPS spectra, the software *CasaXPS* was used [Fai05]. After identifying the photo emission peaks of the elements in the overview scans (s. Fig.

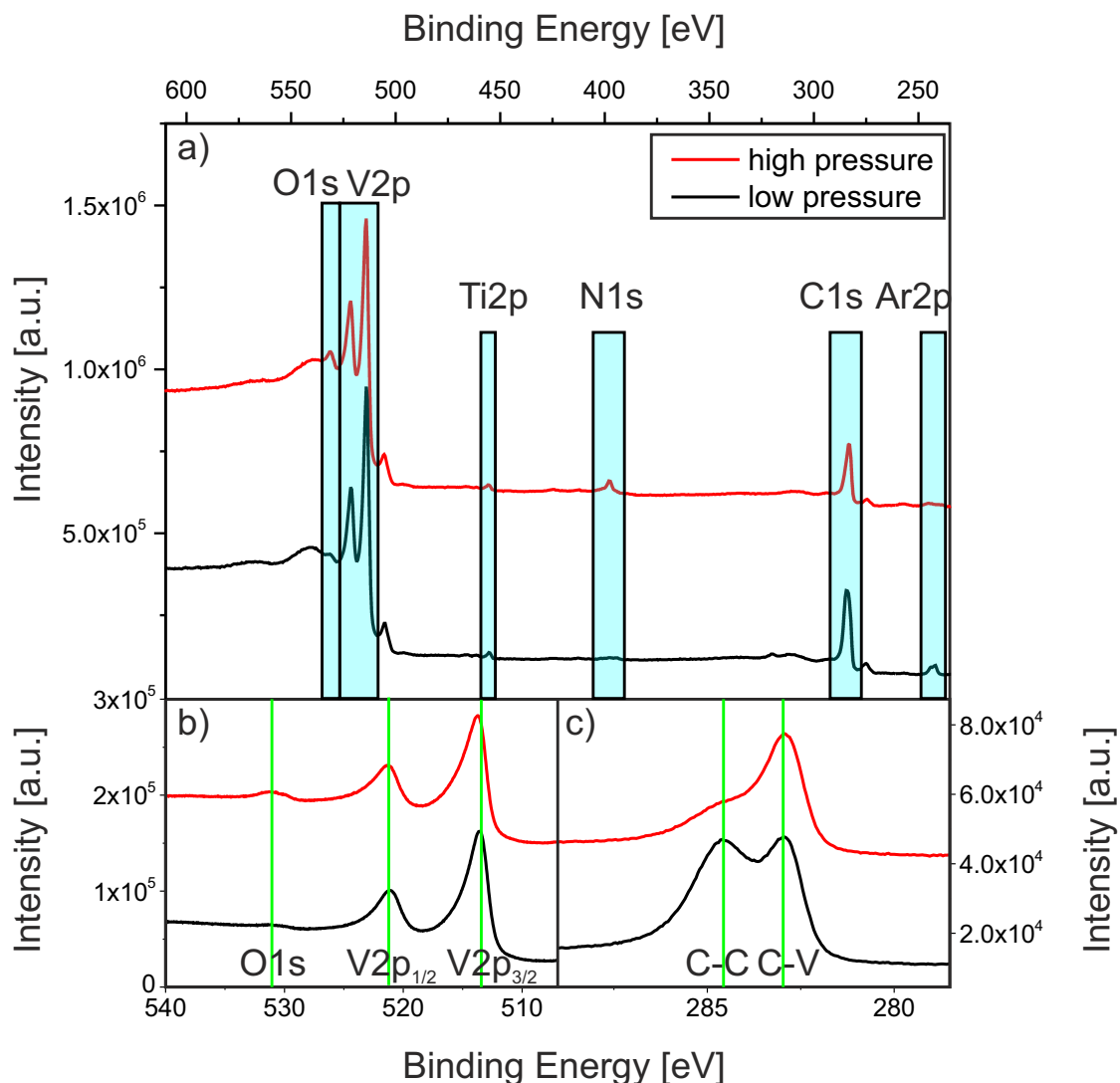


Figure 10.4: (a) Overview scans of the samples grown at low (black) and high (red) pressure. The photo emission peaks of the detected elements are highlighted by blue boxes. (b) Detailed region scans for V2p and O1s. (c) Detailed region scan for the C1s revealing the splitting of the peak due to different chemical bonding.

10.4 a)), regions were defined around the main peaks of the elements. The peak area was determined after background correction. The Shirley background was used for all elements except for the metal components. In this case, the background was subtracted according to Tougaard (s. Chap. 4). The R.S.F.s were taken from the CASA XPS software. Tab. 10.2 summarizes the used photo emission peaks, background subtraction

Element	Transition	Background	R.S.F.
C	1s	Shirley	1.00
V	2p	Tougaard	6.92
N	1s	Shirley	1.59
Ar	2p	Shirley	3.90
O	1s	Shirley	2.31
Ti	2p	Tougaard	6.6

Table 10.2: Background subtraction method and relative sensitivity factors (R.S.F.) used for the determination of the chemical composition of the VC samples.

Element	low pressure (EPMA) [at. %]	low pressure (XPS) [at. %]	high pressure (XPS) [at. %]
C	56.19	56.6	42.2
V	40.35	38.9	47.1
N	0.9	1.6	5.5
Ar	0.65	1.9	1.1
Ti	1.06	0.7	0.7
O	-	0.1	3.4
Ta	0.47	-	-
W	0.37	-	-
C/V	1.39	1.45	0.90

Table 10.3: Results for the chemical composition of the VC_{1-x} thin films grown at a Ar pressure of 0.2 Pa by XPS and EPMA, and Ar pressure of 2 Pa by XPS

method and R.S.F.s for each detected element.

The atomic percentages were determined according to Eqn. 4.2 in Chapter 4. The results of both samples are presented in Tab. 10.3.

In case of *LP*, XPS revealed a higher C content compared to V. In case of *HP*, the C content is smaller than the V content. For *LP* the C/V ratio is approximately 1.4. The C/V ratio of the high pressure sample is 0.9, as can be seen in Tab. 10.3.

Besides C and V, XPS detected traces of N, Ar, Ti and O. As expected, the content of those impurities in the film is low.

As shown in Chap. 4, different background subtraction and R.S.F.s lead to different results for the chemical composition. For the XPS analysis the systematic error is therefore in the range of 4-5 % due to the background and R.S.F.s.

For the verification of our parameters, additional EPMA measurements on the sample *LP-EPMA* were performed by our collaboration partners at IAM-AWP (Tab. 10.3). The

error for the chemical composition in case of EPMA is around 0.5 %.

The results of the XPS analysis and EMPA are in very good agreement. EPMA confirmed the C/V-ratio of 1.45 at low pressure.

Besides the main elements C and V, EPMA detected additionally traces of W and Ta, which can be attributed to contamination in the target.

The determined C/V ratios are in good agreement with the result of the SIMTRA simulations. In the next section, the reason for the different chemical composition at low and high pressure is discussed.

10.6 Discussion: Pressure-induced variations of the chemical composition

In case of low pressure, the chemical composition was determined using XPS and EMPA. For both methods, an excess of C in the film was detected. This is in good agreement with the results of SIMTRA.

However, to exclude that the excess of C is not due to contamination of the sputtering chamber and its components, a pure vanadium metal film was investigated. The sample description can be found in Chap. 5.

The sample was transferred into the XPS via the transfer systems without exposure to ambient conditions. Fig. 10.5 (a) shows the overview scans of the Vanadium thin film. For comparison a typical overview scan of a VC sample is presented. In Fig. 10.5 (b) the normalized C1s peaks of both samples are represented.

As can be clearly seen, the C1s of the VC sample is much higher compared to the low intense C1s peak of the metallic sample. For the Vanadium sample, almost no C is detected.

The blue boxes correspond peak positions of the C1s peak depending on the binding of the carbon [Mou92]. No indication for C-V binding was found for the metal film.

As a final conclusion, the carbon excess in the VC_{1-x} thin films is not due to external contamination in the chamber and has to be result of the sputter process.

Therefore in the following, the sputtering process at the different pressure conditions is discussed based on the results of the simulations.

Considering the results of the TRIDYN simulations (s. Chap. 6), the angular distribution of both elements varies. The TRIDYN calculation investigates only local processes. However, the sputter process at the target is influenced by the geometry of the target and its racetrack.

If the particles do not collide in the gas phase, only the particles with in the angular distribution of 6-16 ° will arrive at the substrate. In this angular range, the emission flux for the C atoms is almost enhanced by a factor of 2 compared to V.

The reason for this enhancement can be understood qualitatively [And88, Ols79]: The compound target consists of two elements which vary significantly in their mass, while

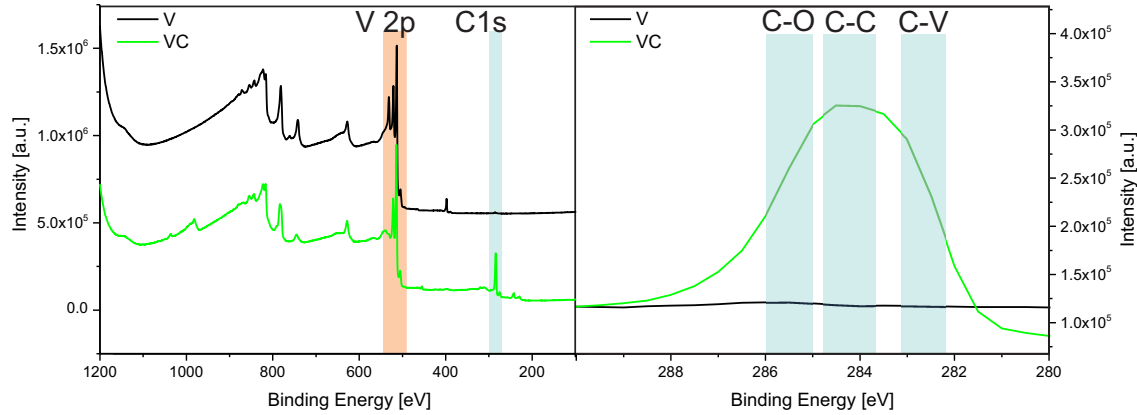


Figure 10.5: (a) Overview scans of the V thin film. For comparison, a typical overview scan of a VC thin film is presented. The V2p photoemission peaks are indicated by orange boxes. The C1s peak position is highlighted by a blue box. The curves are shifted for a better comparison. (b) Normalized C1s peaks of the three samples. Expected peak position of C1s peaks are indicated by blue boxes [Mou92].

the mass of the Ar^+ ions impinging on the target lies in-between.

The mass of C is smaller than the mass of the Ar^+ ions. Therefore, under ion impact the sputtered particle might be reflected from the underlying atoms. The light C atoms are emitted after only few collisions and leave the target preferably along the target normal. The heavier V atoms, however, are emitted by the collision cascades. Therefore, the V atoms undergo much more collisions along their path to the target surface and hence are sputtered off axis with a higher probability. This mechanism tends to increase the yield at oblique emission and thus leads to the observed heart-shaped angular distribution [Yam95].

The preferential sputtering of lighter constituents was first shown experimentally by [Ols79]. However, it was stated that this explanation is only valid for low-energy Ar^+ ions up to 300 eV, which is in good accordance with our experimental setup. A similar result for the nascent angular distribution was found by [Nei08] for Ti-B thin films. Here, the emission flux along the target normal was enhanced for the lighter element B compared to Ti.

Considering the MFP of the elements at low pressure, no collisions are expected in the gas phase. Therefore, the chemical composition is mainly influenced by the sputter process at the target. This explains well the C excess in the thin films at low pressure.

[Mra13] investigated the effect on the chemical composition of the film depending on the angular position of the substrate in respect to the target axis. Comparison of the results is challenging, since the chemical composition of the films is strongly dependent on the chamber geometry. However, the change in chemical composition seems to depend on the relation of MFP and the target-to-substrate-distance.

The films were prepared by sputtering from a Cr-Al-C compound target. For low pressure

conditions, the MFP exceeded the target-to-substrate distance. In this case, the thin film had an excess in C, if the substrate was mounted directly opposite of the target. However, the metallic content in the film increases for higher angles. This is in good agreement with the above-mentioned argument.

At high pressure, the MFP is strongly reduced, resulting in several collisions of the sputtered particles. Since the C atoms are much lighter compared to V, they are sputtered off-axis in collisions with the Ar atoms with a higher probability [Aba09, Nei08, Mra13]. Therefore, less C atoms arrive at the substrate and the composition of the film is closer to the target composition.

In summary, the change in chemical composition is a result of the sputter process from a compound target, where the constituents vary significant in their mass. This leads to element-specific variations of the nascent angular and energetic distribution at the target position. Furthermore, the elements behave differently in the collisions in the gas phase. Similar results have been reported by [Nei08] for Ti-B, by [Mra13] for Cr-Al-C, by [Ekl07] for Ti_3SiC_2 or by [Zha13] for VC-C-Co systems. All found an deviation of the chemical composition in the film from the target composition. At low pressure conditions, if the MFP is larger than the target-to-substrate-distance, an enhancement of the light element was found. At high pressure, the composition of the film changed in favor of the heavier element.

The observed changes in the chemical composition can influence the texture formation in the films. For that, XRD measurements after growth were performed, which are presented in the next chapter.

10.7 Texture investigations

XRD measurements were performed to investigate the influence of the working gas pressure on the texture formation (s. Sec. 5).

Fig. 10.6 shows the radial scan along the sample normal for both samples. The Si(004) peak from the substrate is indicated by an arrow. The main peaks of the coatings are indicated by gray boxes. All coating reflections with the Miller indices (111),(200),(220) and (222) can be attributed to the expected typical rock salt structure.

For *LP*, the (200) peaks is more intense compared to the (111) peak. This is usually found for powder-like samples [Lia05, Sam12]. For *HP*, the (111)-peak is the most intense peak. Hence, *HP-b* exhibits a strong (111)-texture [Zha14].

As shown in Chapter 2, changes in the coating structure have been found for monocarbides of transition metals depending on the C content. Hence the texture might be related to the pressure-dependent chemical composition.

[Sam12] investigated the microstructure of Ti-C systems using reactive sputtering from a metal Ti target. For all films containing C, a NaCl structure was observed. For films with $C/V > 1$, the X-ray pattern show broader and less intense (111) and (200) peaks with increasing C content. SEM cross section shows a featureless microstructure. For films

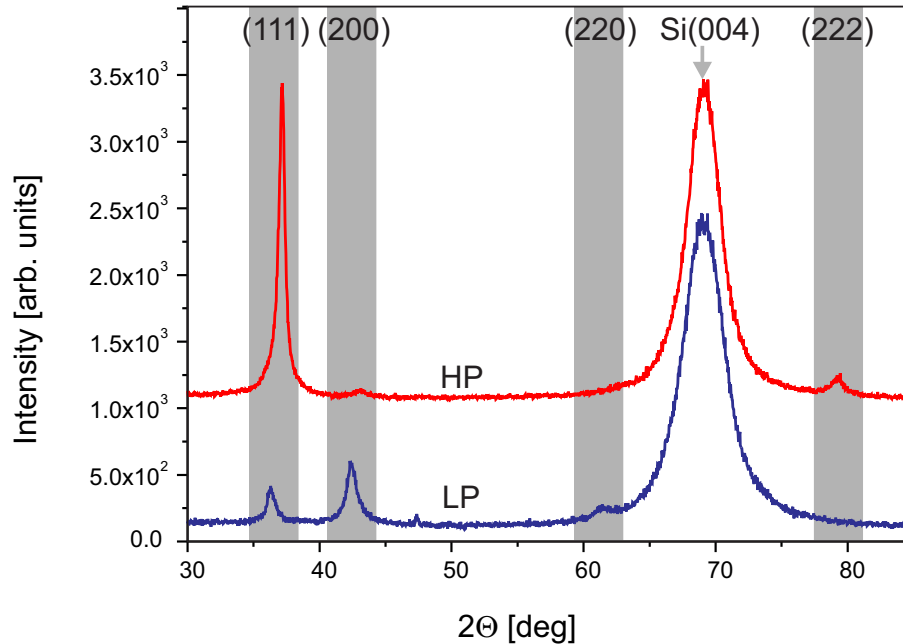


Figure 10.6: $\theta - 2\theta$ scans performed after deposition of the sample grown at high pressure (upper curve) and low pressure (lower curve). The curves are vertically shifted for better comparison. The main peaks are indicated by gray boxes.

with $C/V < 1$, the intensity of the (111) peaks exceeds the (200) peak. The corresponding SEM cross section images of the samples show a columnar microstructure with a rough surface.

[MM09] investigated additionally the microstructure of Ti-C systems. The films were deposited using two single targets of C and Ti. The C content was changed by the variation of the applied power. Cross-section SEM images show the same evolution as [Sam12]. A marked columnar structure vanishes with increasing C content.

[Zha14] prepared Nb-C thin films by reactive sputtering from a Nb target. Also in this work, the XRD measurements showed a transition of power-like to strongly (111)-textured film with decreasing C content.

Independent of the deposition technique and the used transition metals, films with a higher C content were found to be powder-like, while a low amount of C leads to a fiber texture. This is in good agreement with our results.

The differences in the texture explain well the variations in the roughness with time. At high pressure a fiber texture is evolving. This leads typically to a higher roughness of the films due to the strong faceting [Zha05, MM09, Sam12, Zha14].

10.8 Summary & conclusion

In this chapter, the growth of VC_{1-x} thin at different pressure conditions was monitored. The *in situ* measurements are very sensitive to the pressure-induced changes in the microstructure.

At low pressure, the thickness of the film increases almost twice as fast as at high pressure. Simulations of the *in situ* measurements allow the quantitative analysis of the data. At low pressure, the film is smoothening with time. At high pressure, a fast increase in roughness is observed. Moreover, a slight decrease in the mean electron density was found in the beginning, which might be related to the nucleation behavior.

For a better understanding of the sputter process at different pressures, simulations were performed. They indicated a variation in the C/V-ratio for the different pressures. XPS confirmed, that films grown at low pressure have a C excess ($C/V = 1.4$), while at high pressure the metallic content is larger ($C/V=0.9$). The change in chemical composition is due to the sputter process from a compound target, which consists of two elements with significant mass difference.

Moreover, pressure-induced changes in the texture were found, which can be explained by the variations of the chemical composition.

Considering those results, the following growth model is proposed:

At high pressure, the MFP of the sputtered particles is strongly reduced. The particles undergo more collisions leading to a lower thickness increase of the film during the growth. Due to the significant different mass of V and C, less C atoms reach the substrate. This leads to a lower C content in the film and the phase separation is not as enhanced as in case of *LP*. A fiber texture is evolving, which leads to the growth of a rough film.

At low pressure, the MFP of C and V is longer than the target-to-substrate distance indicating almost no collisions of the particles with the Ar atoms.

This leads to a fast increase of thickness, which was shown by *in situ* XRR measurements. Furthermore, the chemical composition of the film is dominated by the element-specific angular distribution at the target position. The growing film exhibits C excess, leading to a phase separation. C-induced re-nucleation leads to the growth of small crystallites and hence to the growth of a smooth film. This is in good agreement with the quantitative analysis of the *in situ* data. At low pressure, the film is rougher in the beginning of the deposition, which can be related to the initial high pressure. However, with time, the content of a-C increases. Due to C-induced re-nucleation, a nanocomposite film grows with small grains, thus resulting in a smooth film.

11 Initial growth of a VC thin film

In the beginning of a sputtering process, the growth conditions, e.g. pressure and power, can change fast due to the special conditions needed for plasma ignition. Those variations in the deposition conditions might influence the microstructure formation.

To avoid deposition during this initial phase, shutter systems are used. The shutters are positioned above the substrate or below the target. They are retracted when the growth conditions are stable.

However, not all sputter systems used in research and industry are equipped with such shutter systems. Hence it is of great interest to investigate the influence of the variations in the deposition conditions on the initial growth. Moreover these investigations might give insight in the growth of samples with a gradient microstructure.

Therefore, *in situ* XRR measurements were performed at different initial pressures. The Si substrate were characterized by angle-dependent XRR measurements. Changes in the microstructure due to the different initial pressures were investigated additionally by post-growth XRR and HRTEM measurements.

11.1 Characterization of the Si substrates

In this chapter, the initial growth of VC_{1-x} thin films is investigated. The choice of the substrate, however, influences the microstructure in the initial growth regime. The used Si substrates are manufactured by the same company, but are taken from different wafers. This might lead to different thickness, electron density and roughness of the SiO_x layer. Therefore, XRR measurements of all Si substrate were performed before growth. All Si substrates showed similar properties. As already shown already in Chap. 10, the XRR measurements could be fitted assuming on top of the Si substrate a 2.5 ± 0.2 nm thick natural oxide layer. The roughness of the interface and the surface were around 0.4 ± 0.03 nm.

The similarity of the Si wafers simplifies the interpretation of the *in situ* XRR data, which are presented in the next section.

11.2 *In situ* measurements of the specular reflectivity

Fig. 11.1 show measured *in situ* XRR curves and their calculated mean value (red line) at the fixed angular position $\alpha_{fix} = 1.6^\circ$ for different initial pressure conditions. The development of the pressure in the chamber is shown by blue lines. The plasma ignition at $t=0$ s is marked by green lines.

In Fig. 11.1 (a) the experimental data for the sample *HP-a* (s. Chapter 10) deposited at constant pressure are presented for comparison.

Fig. 11.1 (b)-(f) present *in situ* measurements, where the pressure condition p_0 at plasma ignition was varied from 4 Pa to 1.5 Pa.

For all deposition conditions except for $p_0=1.5$ Pa, it was verified that the measurements are reproducible (at the same p_0).

Depending on the initial pressure, the growth oscillations of the *in situ* XRR curves show significant differences in the period as well as the amplitude. However, due to the similar characteristics of the *in situ* measurements in certain pressure regimes, the samples can be classified in three groups based on the temporal evolution of the amplitude of the growth oscillations:

1. *high* initial pressure of $p_0=3.5-4$ Pa [Fig. 11.1 (b),(c)]:
The amplitude of the growth oscillations is strongly damped. For $t > 50$ s, the intensity increases significantly.
2. *medium* initial pressure of $p_0=2.5-3$ Pa [Fig. 11.1 (d),(e)]:
The damping of the amplitude is not as strong as at high pressure. The intensity increases with time.
3. *low* initial pressure below $p_0=2$ Pa [Fig. 11.1 (f)]:
The amplitude is not continuously damped, but shows strong variations which are not visible in case of higher initial pressures.

Moreover, for all depositions, during the first 20 s the intensity differs only slightly from the specular intensity before growth. However, for *high* initial pressures a slight decrease is visible. This is not the case for the other samples.

Besides the differences in the amplitude, the mean intensity and the period show variations depending on the initial pressure.

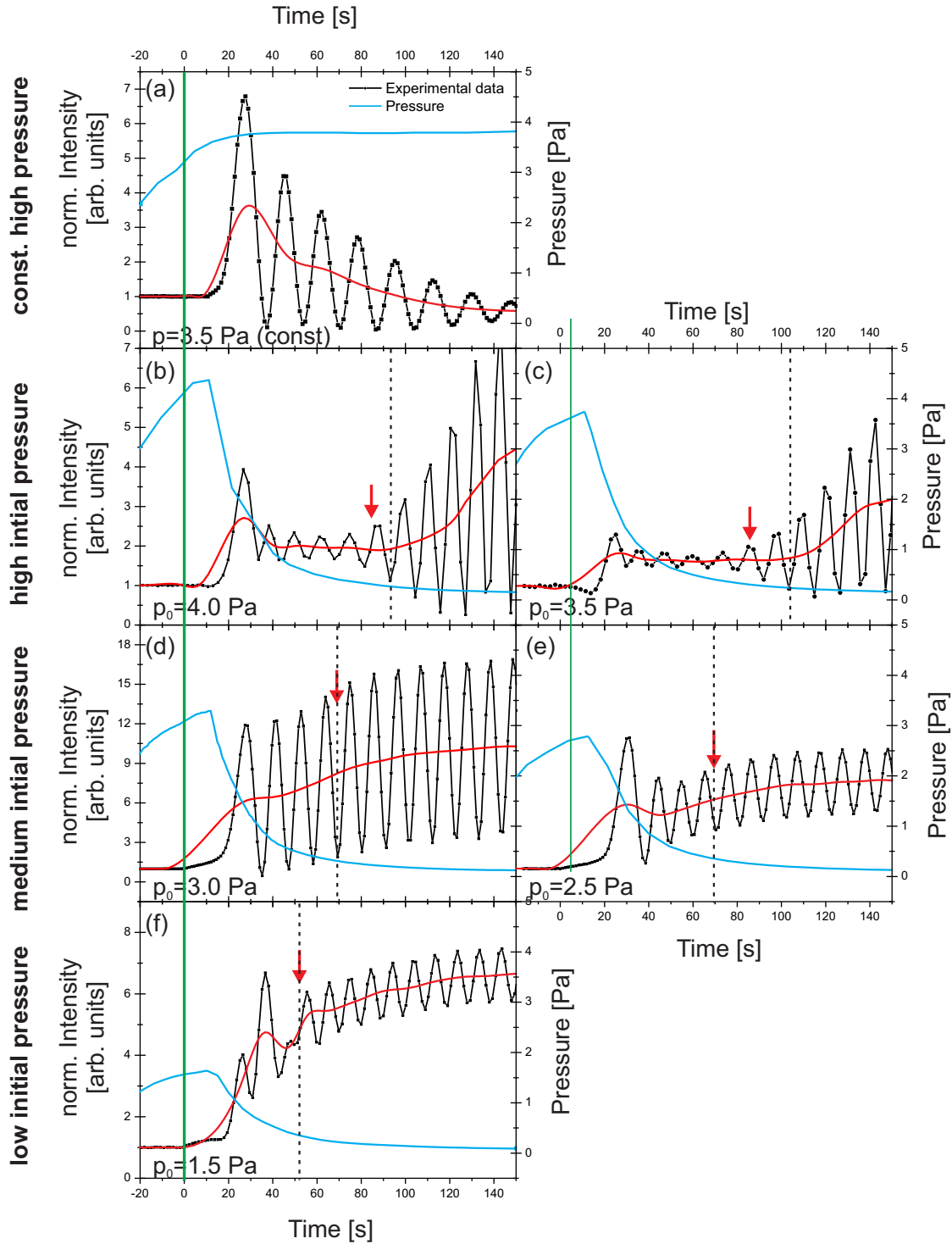


Figure 11.1: *In situ* XRR measurements (black dotted lines) for the different pressure conditions. The pressure development is presented as blue line. At $t = 0$ s the plasma was ignited (marked by a green line). In case of (a), the pressure was kept constant. (b)-(f) present the experimental data at different initial pressures, where the Ar flux was reduced after plasma ignition. *In situ* measurements which show similar characteristics are plotted in the same row.

For all *in situ* curves, the mean intensity has a peak at $t \approx 30$ s. For $t > 60$ s, the mean value behaves differently depending on the pressure conditions: At *high* constant pressure, the mean value decreases. For the other samples, an increase of the mean value with increasing p_0 is visible.

Changes in the oscillation period τ with time and decreasing pressure can be observed in case of *low* initial pressure. Here the first three oscillation differ in their period τ from each other.

When extracting the period length of the single growth oscillations for every p_0 , the same behavior is found for all samples. However, for all samples, after a certain deposition time, the period stays constant at $\tau \approx 10$ s (denoted by dotted line in Fig. 11.1).

τ is related to the rate of thickness increase, F_D , (s. Chap. 8). It was shown that the DC power as well as the working gas pressure have a strong influence on F_D (Chap. 9 and 10). During the initial growth, power and pressure vary fast, which in turn leads to a temporal changing deposition rate.

In Chap. 9, the linear relation between DC power and deposition rate was shown. The changes in the deposition rate depending on the pressure can be calculated using the Keller-Simmons formula (s. Chap. 1). Combing this, the following time-, pressure- and power-dependent growth rate $F(t)$ is found:

$$F(t) = \underbrace{F_0}_{f_0 \cdot F_{power}(t)} \cdot \underbrace{\frac{\lambda(E_{sp}, p(t))}{d_{TS}} \left(1 - \exp\left(-\frac{d_{TS}}{\lambda(E_{sp}, p(t))}\right) \right)}_{f_{KS}}, \quad (11.1)$$

where f is a normalization factor. $F_{power}(t)$ is the time-dependent deposition rate due to the ramping of the power, depending on the power $P(t)$:

$$F_{power}(t) = F_D(200W) \cdot \frac{P(t)}{200W} t \quad (11.2)$$

where $F_D(200W) = 0.215$ nm/s is the experimental determined values at the DC power 200 W, respectively (s. Chap. 9). $F_{ramp}(t)$ is presented in Fig. 11.2, black curve.

For the calculation of Keller-Simmons Equation f_{KS} , the energy-, pressure- and time-dependent MFP is needed. In the following, the calculations are performed for the case of *high* initial pressure. For the other pressure conditions, the calculations are performed in the same manner.

Since the sputter process involves two elements, two independent MFPs $\lambda(E_{sp}, p(t))$ are calculated. The results are presented in Fig. 11.2(b) for C (black curve) and V (green

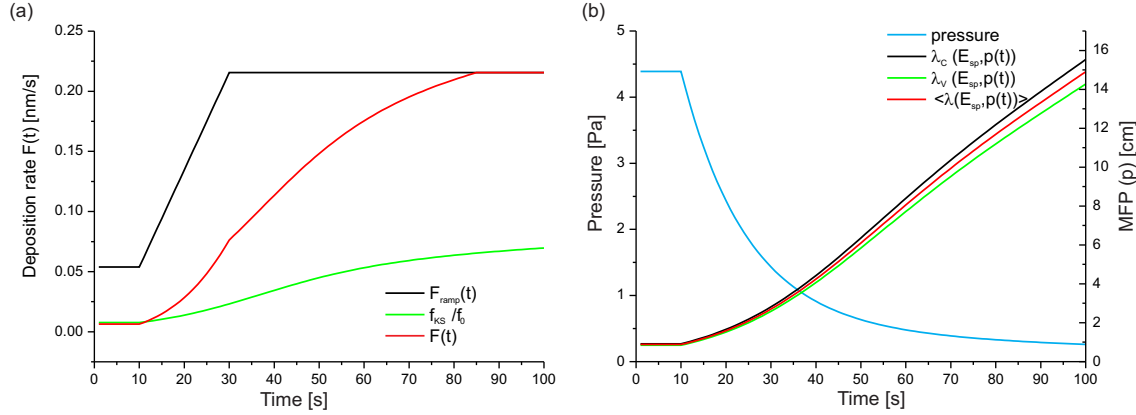


Figure 11.2: (a) Dependence of F on the experimental parameters DC power and pressure. For details s. text. (b) Development of the pressure at *high* initial pressure, the calculated element-specific MFP, and its mean values $\langle \lambda(E_{sp}, p(t)) \rangle$.

curve). With increasing time the pressure decreases. In turn, the mean free path of both elements increases and saturates for small pressures.

For simplicity, the arithmetic mean of the MFP of both elements $\langle \lambda(E_{sp}, p(t)) \rangle$ is chosen (red line in Fig.11.2 (b)).

For the determination of f , the following considerations are taken into account:

From the experiments, the deposition rate of $F_D = 0.215$ nm/s at a constant low pressure of $p=0.2$ Pa was determined. For this pressure, no collisions in the gas phase are expected.

$\langle \lambda(E_{sp}, p(t)) \rangle$ exceeds the substrate-to-target distance for $t > t = 81$ s for the here presented pressure condition. This coincides with pressure values $p < 0.3$ Pa (s. Fig. 11.2 (a)).

This indicates that for this pressure regime, collisions in the gas phase are negligible and a maximum deposition rate at $P=200$ W is found at 0.215 nm/s. Therefore, $F(t)$ was normalized to $f_{KS}(p = 0.3 \text{ Pa}, t(p = 0.3 \text{ Pa}))$.

The resulting $F(t)$ for high pressure is shown in Fig. 11.2 (a), red curve. For the first 10 s, the deposition rate is strongly reduced. Afterwards it increases with time and decreasing pressure.

Fig. 11.3 presents the calculated $F(t, p_0)$ for the different p_0 . With increasing initial pressure p_0 , F_D increases slower with time. The moment, when F_D is constant, is delayed. This leads to different time-dependent changes in the deposition rate for each sample.

At *low* and *medium* initial pressure, the period of the oscillations is constant for $p < 0.3$ Pa (marked by a red arrow in Fig. 11.1). This indicates that at this point in time the

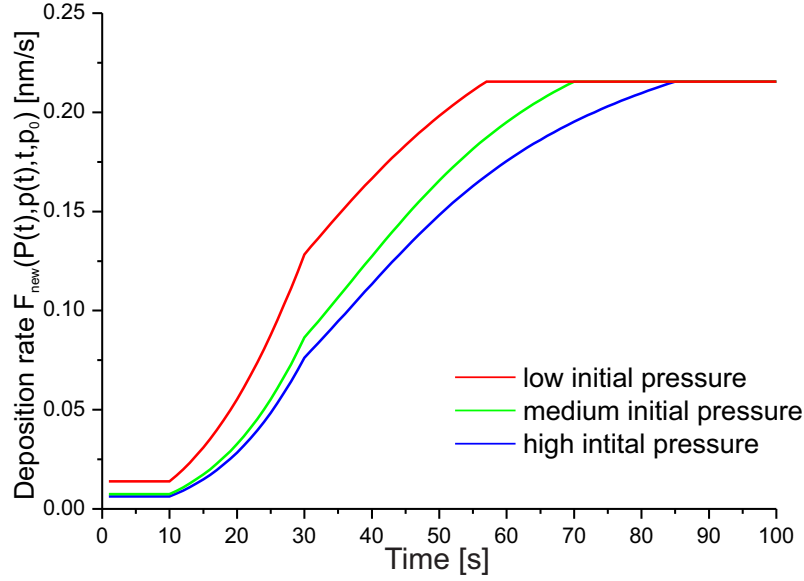


Figure 11.3: $F_{new}(p,P,t)$ for the three different pressure conditions.

growth process is comparable to the film formation at *steady growth conditions*. Here only changes at the growth front were assumed.

However, the time-dependent deposition rate cannot explain all changes of the period.

In case of *low* initial pressure, the deposition rate increases continuously. However, the period length varies strongly if the pressure is higher than 0.3 Pa. At *high* initial pressure, oscillation with constant periods are visible, when the pressure dropped below $p < 0.2$ Pa. By changing the deposition rate, additionally the diffusion length $L_{diff} \propto \sqrt{\frac{1}{F_D}}$ is influenced (s. Chap. 1)[Mah09]. This might influence the microstructure formation in the initial growth regime. Therefore, angle-dependent reflectivity measurements performed after the deposition, which will be discussed in the next chapter.

11.3 X-ray reflectivity after growth for different initial pressure

For a better understanding of the influence of the pressure on the initial growth of the VC_{1-x}/a-C thin films, angle-dependent XRR measurements were performed directly after the deposition *in vacuo*.

In Fig. 11.4 (a), the experimental data of one sample deposited at *high*, *medium* and *low* initial pressure are presented in colored lines. The total deposition time was 600 s in the case of $p_0=1.5$ Pa and $p_0=3.5$ Pa. For $p_0=2.5$ Pa, the growth was stopped after 200 s. The best fits are presented as black lines. The curves are shifted for better comparison. Fig. 11.4 (b) and (c) show highlighted regions of the XRR measurements and their fits for the films grown at low and high pressure. As can be seen, the simulations are in good

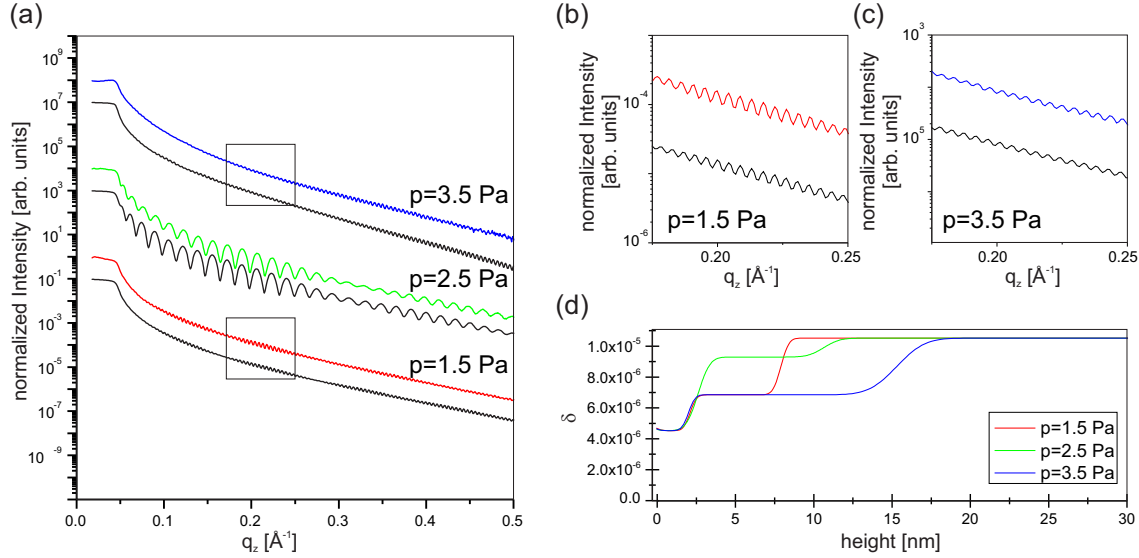


Figure 11.4: (a) Angle-dependent XRR measurements (colored lines) for different initial pressures after growth. The best fits (always shown in black) is shifted for better comparison. (b) and (c) present highlighted regions of the XRR measurements at high and low initial pressure. (d) δ -profiles around layer I resulting from the input parameters for the fit.

agreement with the experimental data.

The critical angle for all samples is located at $\alpha_c = 0.25^\circ$ ($q_z = 0.044 \text{ \AA}^{-1}$). This corresponds to a electron density of 5.1 g/cm^2 , which is 88% of the theoretical bulk density of V-C (s. Chap. 10). It was not possible to fit the curves assuming a single layer. An interface layer (in the following called layer I) was needed for achieving a good agreement with the experimental data. Without the additional layer, the beating in the XRR curve could not be simulated.

For the different initial pressures, the thickness D , roughness σ and electron density ρ_e of layer I were varied. The resulting δ -profiles around layer I are presented in Fig. 11.4 (d). The input parameters, additionally determined for $p_0 = 3$ Pa and $p_0 = 4$ Pa, are presented in Fig. 11.5.

The thickness D decreases with increasing initial pressure from 13 nm to 6 nm. For the low and high pressure, ρ_e of layer I was strongly reduced to 61% of the theoretical bulk density of V-C to achieve a good agreement with the data. The layer I at medium pressure is an exception. The electron density was reduced only to 81 % of the bulk value. At high pressure, the highest roughness value was needed for achieving a good agreement with the experimental data. At medium and low pressure, the value used for the roughness were much smaller.

The systematic change in the thickness D of the interface layer can be related to the variations in the period τ observed in the *in situ* measurements.

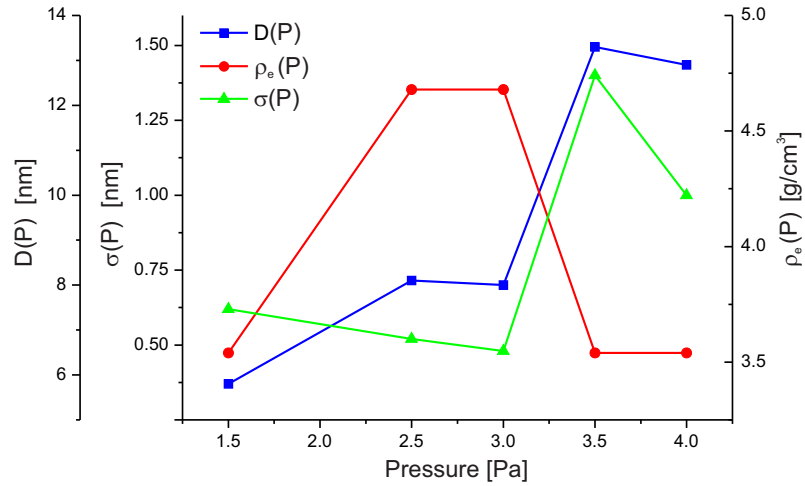


Figure 11.5: Thickness $D(P)$, roughness $\sigma(P)$ and electron density $\rho_e(P)$ for the different interface layer, used for the fit of the experimental data.

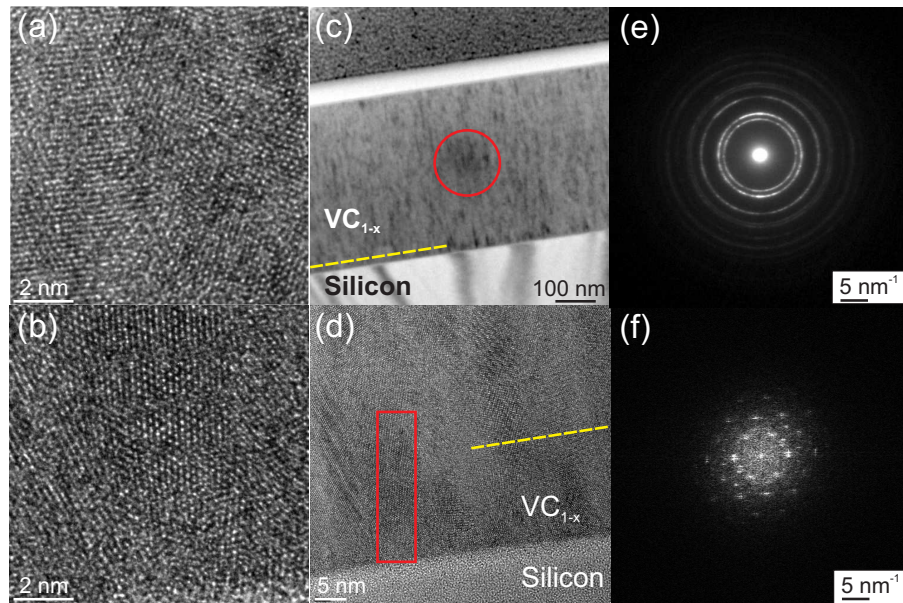


Figure 11.6: TEM analysis of samples deposited at *high* initial pressure. Highlighted regions at for the *steady* growth regime are presented in the upper row, regions close to the Si substrate are shown in the lower row. (a) and (b): HRTEM cross section images. In (c) and (d), the area surrounded by a red line presents the region chosen for the diffraction analysis. The corresponding diffraction pattern is presented in (e) and (f).

For example, at *low* initial pressure, a 6 nm thick interface layer was used for the fitting.

At the here used experimental conditions, during one oscillation period approximately 2.2 nm of the film are deposited. Hence, for the deposition of the interface layer, 3 growth oscillations should be observed.

In case of *low* initial pressure, the period τ of the first 3 growth oscillations varied. Afterward the period is constant. This indicates that the interface layer growth takes place, as long as no constant oscillation periods are recorded.

The same relation between interface layer thickness and the period τ is found for the other samples grown at the different p_0 . This strongly indicates that the two growth regimes can be directly identified during an *in situ* measurements.

The variations in the thickness are due to the influence of the pressure on the deposition rate. By increasing p_0 , the pressure decreases slower with time in the chamber. This in turn delays the moment, when *steady* growth conditions are reached. Hence the thickness D of layer I increases with p_0 .

Moreover, the roughness values determined by the fit are in good agreement with the expectations from the *in situ* measurements:

At *high* initial pressure the amplitudes of the *in situ* curve are strongly damped - indicating a high roughness of the layer I (s. Chap. 10). This was confirmed by the fit of the angle-dependent XRR curve after growth.

At *low* and *medium* initial pressure no strong damping of the amplitude was visible - indicating the formation of a smooth interface layer. This is again in good agreement with the fit parameters of the XRR measurement.

The XRR measurements directly after growth could only be fitted by introducing a second layer. The fit results agree well with the analysis of the *in situ* data. For a further investigation, if the initial growth regime varies from the steady growth conditions, HRTEM images of the sample grown at *high* initial pressure are presented in the next section.

11.4 Transmission electron microscopy

Fig. 11.6 shows the HRTEM analysis of the sample deposited at *high* initial pressure ($p_0=4$ Pa). The upper row shows highlighted regions at for the *steady* growth regime. The lower row presents images taken of the area close to the Si substrates.

(a) and (b) present the HRTEM cross-section images of regions $10\text{nm} \times 10\text{nm}$. Both regions show large nanocrystallites which are elongated along the growth direction.

In (c) a dark field image of the entire film is presented. The height of the interface layer determined from the XRR fit is indicated as a yellow dotted line. Darker spots are visible in the region of the interface layer. However, in the HRTEM cross-section image close to the Si substrate presented in Fig. 11.6 (d), a clear and interface layer - as determined by the XRR measurements - is not visible.

Additionally electron diffraction was performed. The illuminated region for the later growth regime is depicted by a red box in Fig. 11.6 (c). Here a large area of the film was illuminated. The corresponding diffraction pattern is shown in Fig. 11.6 (e). Rings are visible in the diffraction pattern. This implies, that the film exists of more nanocrystallites.

For the initial growth regime, digital diffraction analysis has been performed. For that, the Fourier-transform of the region indicated by the red box in Fig. 11.6 (d) was calculated. For this very restricted field of view, the diffraction pattern shows spots, indicating an almost single-crystalline region of the film.

The TEM analysis showed that the film consists of large nanocrystallites. However, a clear indication of the growth of a bilayer system is not given. In the next section, the experimental results of the *in situ* XRR measurements and the measurements after growth are summarized and discussed.

11.5 Summary & proposed growth models

In the previous sections, the influence of the fast varying deposition conditions in the initial growth regime on the microstructure was investigated.

Therefore the initial growth was monitored by *in situ* XRR. Depending on the initial pressure, different characteristic features of the *in situ* data were observed, in particular the period τ and the amplitudes of the growth oscillations showed significant differences. The XRR measurements after growth showed that in the later growth regime all films exhibit similar electron density. For the fitting of the XRR curve, interface layers were introduced, which differed in thickness, electron density and roughness depending on the initial pressure condition.

This layer could not be clearly identified by TEM analysis.

The results of the *in situ* measurements were compared with fit results of the angle-dependent XRR measurements after growth.

The thickness of the interface layer coincided with the estimated thickness increase during the deposition time, at which growth oscillations with a varying period are recorded. This indicates that the growth of the interface layer can be directly observed during the *in situ* measurement.

The temporal variations in the amplitude can be related to the roughness development of the film. For example, in case of *high* initial pressure, a strong damping of the amplitude was found - indicating a high roughness of the interface layer. This was confirmed by the fit results of the angle-dependent XRR measurements.

The variations in the microstructure formation in the initial growth regime are strongly

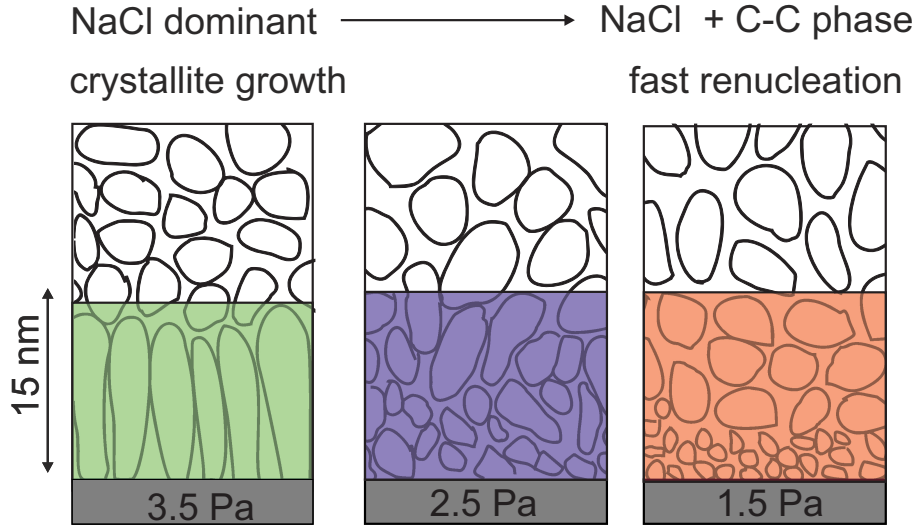


Figure 11.7: Proposed growth models for the different initial pressures.

related to the pressure conditions. The pressure influences the deposition rate and the chemical composition of the film (s. Chap. 10). It was shown that at the initial growth regime, with decreasing initial pressure, an increase in the deposition rate is expected. In turn the diffusion length decreases. Moreover, pressure-induced changes in the chemical composition are expected with time, since the pressure additionally varies with time. With decreasing pressure, the C content in the film increases. C-induced re-nucleation leads to a smoothening of the film with time.

Based on these results, growth models for different initial pressures p_0 are proposed, which are presented in Fig. 11.7.

At *high* pressure, the deposition rate is strongly reduced. In addition, due to the high pressure in the beginning, the C-content in the film is low. Both lead to a larger distance between two nuclei and hence to a formation of large islands [Mah09]. Moreover, due to the low C-content, a high roughness is expected as shown in Chap. 10.

This is in good agreement with the results of the sample grown at low pressure conditions (presented in Chap. 10). Here a smoothening of the film was observed. In literature usually a increase in roughness with film thickness is reported. This is not the case for this sample, since the interface layer has a high roughness.

At *medium* pressure, the diffusion length is shorter than at *high* pressure due to the enhanced deposition rate [Zha97]. Since the initial pressure is lower, the C content in the beginning is higher. Smaller islands are formed. When the pressure drops below

$p > 0.3$ Pa, the growth equals the deposition at the *steady growth regime*.

At *low* initial pressure, the deposition rate is high. In turn, the diffusion length is strongly reduced [Zha97]. Additionally the C content is high from the beginning. Small islands are formed. Due to the high C-content, fast re-nucleation happens. When $p < 0.3$ Pa, *steady growth conditions* are reached.

In this chapter, it was shown that the *in situ* measurements are very sensitive to changes during the microstructure formation in the initial growth regime. For gaining a fundamental understanding, how changes in the film formation influences the behavior of the *in situ* curve, simulations are performed in the following chapter.

12 Simulation of *in situ* X-ray reflectivity measurements

The *in situ* measurements during the initial state were strongly influenced by the film formation (s. Chap. 11). For gaining a better understanding, how the *in situ* XRR curves are related to the microstructure formation, simulations are performed. As the experimental results showed, the microstructure formation in the initial growth cannot be easily described as a layer system during the growth. Changes in the microstructure below the growth front e.g. due to diffusion processes are expected.

For a fundamental understanding of changes in the temporal specular intensity, simulations of the *in situ* data at the initial growth were performed. For this, an approach developed in framework of the bachelor thesis of Jochen Gemmler [Gem12], was followed. For the description of the initial microstructure formation, a growth model was developed, which serves as a basis for *in situ* XRR simulations.

Simulation parameters were changed systematically and set in relation to calculated *in situ* XRR curves. Finally, the results of the simulations were compared with the experimental data, presented in Chap. 11.

12.1 Growth model

For gaining a fundamental understanding of different growth behavior, a 2D growth model was used. TEM images indicated an elongated fiber structure. Therefore here the following model was used: islands grow on top of the Si substrate and increase in size with deposition time.

Half-ellipsoid shaped islands were chosen as presented in Fig. 12.1. This model simplifies the complex growth in the initial regime. However, it allows the investigation of e.g. temporal roughness changes.

For the analytical description of the model, the time-dependent axis $a(t)$ of the half-ellipse is directed perpendicular to the growth direction z , the axis $b(t)$ parallel to z .

In this case, the equation of an ellipse is given by:

$$\frac{z^2}{b^2} + \frac{x^2}{a^2} = 1 \tag{12.1}$$

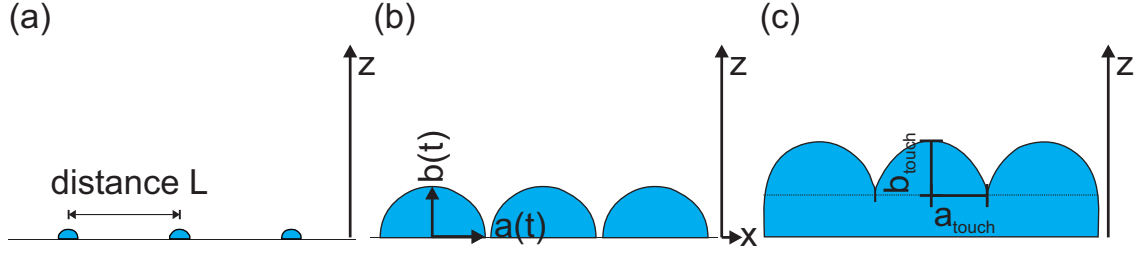


Figure 12.1: Scheme of the two-dimensional islands with an half-ellipsoid shape using $\varepsilon=0.2$ at different times. The major and minor axis of the ellipse are indicated in (b).

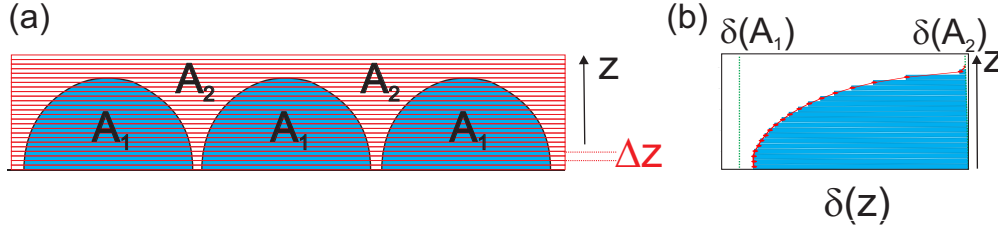


Figure 12.2: Scheme of the calculation of the density profile of the islands. (a) Slicing of the growth model into virtual slices. (b) Corresponding δ -profile.

The axes $a(t)$ and $b(t)$ are related by

$$b(t) = a(t)\gamma. \quad (12.2)$$

γ is defined by

$$\gamma = \begin{cases} \sqrt{1 - \varepsilon^2} & \text{for } b(t) > a(t) \\ \frac{1}{\sqrt{1 - \varepsilon^2}} & \text{for } a(t) > b(t), \end{cases} \quad (12.3)$$

where $0 < \varepsilon < 1$ is the eccentricity, which defines the deviation of the ellipse from a circle ($\varepsilon = 0$).

For $\gamma < 1$, the islands are larger in height than in width. For $\gamma > 1$, the opposite behavior is found.

The area $A(t)$ of the islands is time-dependent:

$$A(t) = 1/2 \pi a(t)^2 \gamma, \quad (12.4)$$

Up to a given point $t = t_{max}$, at each time $t = t_j$, the area of the islands increases by

$\Delta A(t)$, which is determined by the deposition rate F_D :

$$A(t_{j+1}) = A(t_j) + \Delta A(t_{j+1}). \quad (12.5)$$

The shape of the islands is determined by calculating $a(t)$:

$$a(t) = \sqrt{\frac{2 A(t)}{\pi \gamma}} \quad (12.6)$$

When the islands touch, which is the case for $a(t) = \frac{L}{2}$, the shape of the islands is kept unchanged. A closed layer is formed (s. Fig. 12.1 (c)).

In case of a constant area increase $A(t) = \Delta A t = F_D \frac{L}{2} t$, the following relation for t_{touch} using Eqn. 12.6 is found:

$$t_{touch} = \frac{\pi L}{4 F_D} \gamma \quad (12.7)$$

For $t \geq t_{touch}$, $a(t \geq t_{touch}) = \frac{L}{2}$ stays constant. $b(t \geq t_{touch})$ is given by:

$$b(t_{touch}) = \frac{L}{2} \gamma \quad (12.8)$$

For the calculation of the *in situ* XRR measurements, the geometric growth model needs to be converted into a time-dependent density profile. For that, at each chosen time-step t_j , the model is sliced in j virtual layers with the thickness Δz as shown in Fig. 12.2 (a). Each virtual layer contains the areas $A_1(j)$ of the material with the refractive index n_1 and $A_2(j)$ of vacuum with $n_2=1$. The average refractive index $\langle n \rangle_j$ of each virtual layer j is calculated by

$$\langle n \rangle_j = \frac{A_1(j)}{A_1(j) + A_2(j)} n_1 + \frac{A_2(j)}{A_1(j) + A_2(j)} n_2. \quad (12.9)$$

This results in a density profile as shown in Fig. 12.2 (b).

For the creation of the density profile, t_j and Δz were chosen such a way that a smooth δ -profile was achieved.

Due to the simplicity of the model, the maximum height $z_{max}(t)$, the rms-roughness $\sigma(t)$ and the surface coverage $S(t)$ can be described analytically, expressed by L , γ and F_D . This allows later the derivation of the scaling behavior depending on the distance L

and the shape γ of the islands.

For a simpler representation of the formulas, the above-mentioned properties are expressed by $a(t)$, which will be replaced in the following sections by Eqn. 12.6 for the determination of the scaling behavior.

Using Eqn. 12.1 the time-dependent height $z(t)$ is given by

$$z(x,t) = \begin{cases} \gamma a(t) \sqrt{1 - \left(\frac{x}{a(t)}\right)^2} \Theta(a(t) - x) & \text{for } t < t_{touch} \\ \frac{L}{2} \gamma \sqrt{1 - \left(\frac{2x}{L}\right)^2} + F_D \frac{L}{2} (t - t_{touch}) & \text{for } t \geq t_{touch}, \end{cases} \quad (12.10)$$

where Θ is the Heaviside function.

The maximum height $z_{max}(t)$ at each time step of the model is given by

$$z_{max}(t) = \begin{cases} \gamma a(t) & \text{for } t < t_{touch} \\ \frac{L}{2} \gamma + F_D \frac{L}{2} (t - t_{touch}) & \text{for } t \geq t_{touch}. \end{cases} \quad (12.11)$$

For the calculation of the mean height $\langle z(x,t) \rangle$, the integration range in x -direction was performed in the interval $[0, L/2]$ (s. App. 13.4).

The mean height $\langle z(x,t) \rangle$ is given by:

$$\langle z(x,t) \rangle = \begin{cases} \frac{\pi}{2} \frac{a(t)^2 \gamma t}{L} & \text{for } t < t_{touch} \\ \frac{\pi}{8} L \gamma + F_D \frac{L}{2} t & \text{for } t \geq t_{touch}. \end{cases} \quad (12.12)$$

Taking these results, the rms-roughness $\sigma(t)$ of the system can be calculated (s. Chap. 3):

$$\sigma(t) = \begin{cases} \sqrt{\frac{a(t)^3 \gamma^2}{\frac{L}{2}} \left(\frac{2}{3} - \left(\frac{\pi}{4}\right)^2 \frac{a(t)}{L} \right)} & \text{for } t < t_{touch} \\ \sqrt{\left(\frac{L}{2} \gamma\right)^2 \left(\frac{2}{3} - \left(\frac{\pi}{4}\right)^2 \right)} & \text{for } t \geq t_{touch}. \end{cases} \quad (12.13)$$

Another important characteristic which is discussed here is the surface coverage $S(t)$, which is given by

$$S(t) = \begin{cases} \frac{2 a(t)}{L} & \text{for } t < t_{touch} \\ 1 & \text{for } t \geq t_{touch} \end{cases}, \quad (12.14)$$

In the following, the influence of the distance L , the shape γ , and the growth rate F_D of the islands on the *in situ* measurements is investigated. The scaling behavior of these parameters is analyzed and related to calculated *in situ* XRR curves.

12.2 Influence of the distance L of the islands

In this section, the influence of different distances L of the islands on the *in situ* XRR curves is investigated. By changing the distance L the influence of different diffusion behavior is investigated [Zha97].

In the initial growth stage on a flat surface, the diffusion coefficient determines the average distance an ad-atom will have to travel before meeting another ad-atom and forming a new island.

For this investigation, the other simulation parameters are kept constant. The choice of $F_D = 0.215$ nm/s was adapted to the experimental determined values of Chap. 10.

For the shape of the islands $\gamma = 0.44$ was chosen.

Fig. 12.6 presents the distribution of the islands for different distances L .

Since the deposited material is distributed to all nucleation sites, the size of the islands increases with larger distance L . This in turn delays the moment t_{touch} . Taking Eqn.12.8 into account, $t_{touch} \propto L$.

In the following, the changes in $z_{max}(t)$, $\sigma(t)$, and $S(t)$ with time and distance L are presented.

Fig. 12.4 presents the simulated maximum height $z_{max}(t)$ for $L = 5, 30$, and 60 nm. The behavior of $z_{max}(t)$ is similar for all L . In the beginning, the height increases fast. Then, the slope decreases slightly up to $t = t_{touch}$. For $t \geq t_{touch}$, a linear increase is found. The slope of the curve is identical for all distances L . However with increasing L , the maximum thickness increases.

For the maximum height $z_{max}(t)$ the following scaling behavior with L is found:

$$z_{max}(t) \propto \begin{cases} L^{1/2} & \text{for } t < t_{touch} \\ const. & \text{for } t \geq t_{touch} \end{cases}, \quad (12.15)$$

Fig. 12.4 (b) shows the time-dependent roughness for the different island distances. When the islands start to growth, the roughness increases up to a maximal roughness. Then the roughness decreases, when the islands grow closer together. For $t > t_{touch}$, the roughness stays constant. With increasing L the film has a higher roughness.

Using Eqns. 12.13, the roughness $\sigma(t, L)$ can be expressed by:

$$\sigma(t) \propto \begin{cases} \sqrt{L^{3/2} - L} & \text{for } t < t_{touch} \\ L & \text{for } t \geq t_{touch} \end{cases}. \quad (12.16)$$

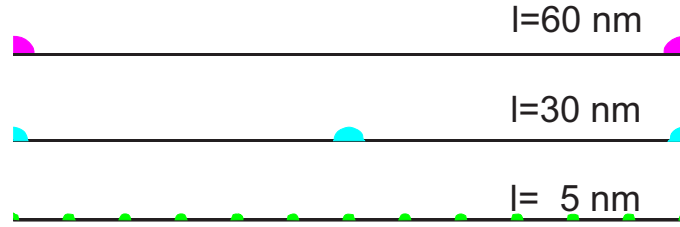


Figure 12.3: Distribution of the islands for different distances $L = 60$ nm, 30 nm and 5 nm. The size of the islands decrease with increasing L . $\gamma = 0.44$ is kept constant.

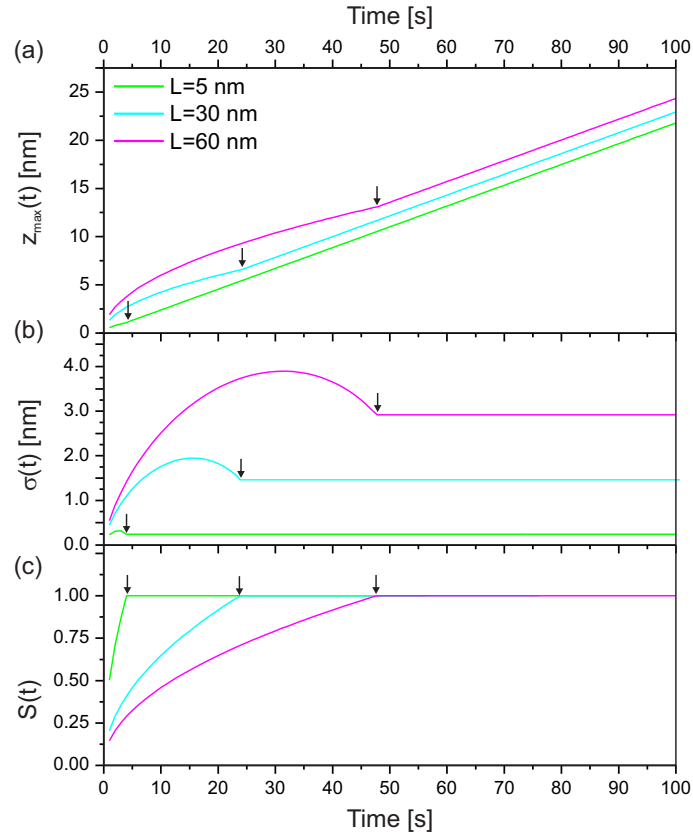


Figure 12.4: Time-development of (a) the maximum thickness $z_{max}(t)$, (b) roughness $\sigma(t)$ and (c) surface coverage $S(t)$ for $L = 60$ nm, 30 nm and 5 nm. The moment t_{touch} , when the islands touch is indicated by black arrows.

The behavior of $S(t)$ is presented in Fig. 12.4 (c) for $L = 5$, 30 , and 60 nm. With increasing L , the surface coverage is lower. Since for larger L , t_{touch} is delayed, a total

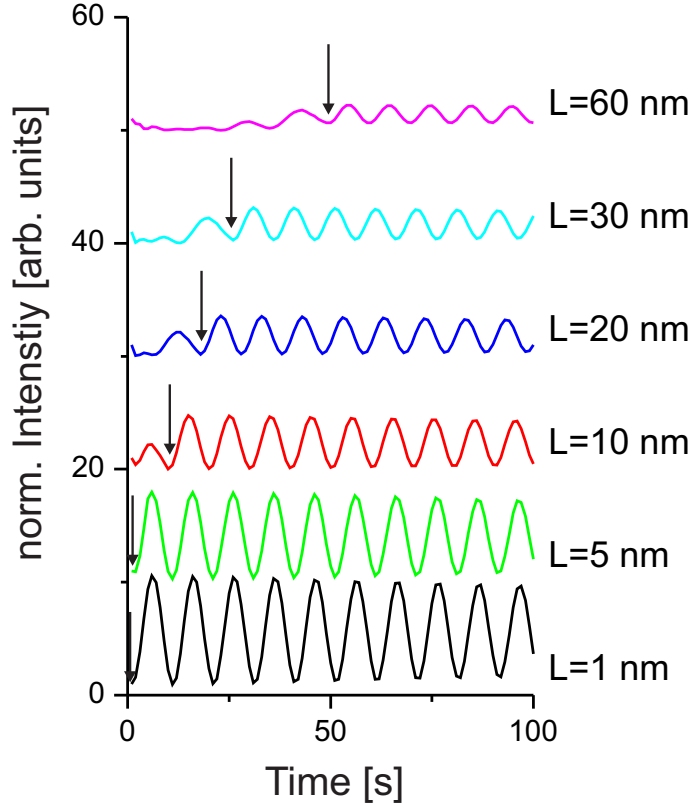


Figure 12.5: Calculated *in situ* XRR measurements of the growth models at fixed deposition rate $\Delta F=0.215$ nm/s and fixed shape ($\gamma = 0.44$) considering different distances L of the islands. The arrow denotes the moment t_{touch} , when the islands touch. The curves are all shifted by a constant value for better comparison.

coverage of the surface is delayed, too. The surface coverage $S(t)$ scales with L by:

$$S(t) \propto \begin{cases} L^{-1/2} & \text{for } t < t_{touch} \\ const. & \text{for } t \geq t_{touch} \end{cases}, \quad (12.17)$$

In situ XRR curves were calculated for the described layer model. The substrate was introduced by adding two additional layers, the Si substrate and the SiO_x layer. The values for thickness, roughness and mean electron density were taken from Chap. 10.

The results of the calculation are presented in Fig. 12.5.

Independent of the chosen distance L , regular oscillations with constant period and amplitude are visible for $t > t_{touch}$. t_{touch} is denoted by an arrow in Fig. 12.5.

Oscillations with first decreasing, then increasing period are visible. This can be understood by the behavior of $z_{max}(t)$ presented in Fig. 12.4 (a). First $z_{max}(t)$ increases fast.

This results in a high thickness increase and hence to long period lengths. Shortly before the islands touch, the slope of the maximum height is reduced. The thickness increase is slower, leading to shorter period lengths. For $t \geq t_{touch}$, $z_{max}(t)$ is a linear function. The film increases with constant growth rate. The period of the growth oscillations is constant.

Hence, the two growth regimes can be directly distinguished in the *in situ* data.

Additionally, the amplitude and the mean value of the *in situ* curve depends on the distance L .

For $L = 1$ nm and $L = 5$ nm, the intensity increases at the beginning. For larger L , the intensity decreases. In Chap. 8, it was shown that an intensity increase is expected if the film density has a higher optical density than the substrate. For the here discussed material system, this is the case for $S(t) > 0.5$.

This observed change in the simulated intensity is related to the surface coverage, which is larger than 50 % for $L < 5$ nm (s. Fig. 12.4 (c)).

Comparing the amplitudes, a systematic decrease in intensity is visible with increasing L . This corresponds to the increase in roughness with larger L (s. Eqn. 12.16).

By changing the distance L , the influence of the diffusion behavior on the *in situ* XRR was investigated. Changes in the period and the amplitude were related to the distance L . As a next step, the influence of the shape on the *in situ* XRR curves is investigated. This is presented in the next section.

12.3 Influence of the shape of the islands

For investigating the influence of different shapes on the *in situ* XRR curves, γ was systematically changed. The other parameters were kept constant. As distance L of the islands 30 nm was chosen.

In Fig. 12.6, islands with different shapes γ are presented: $\gamma = 0.44, \gamma = 0.87, \gamma = 1, \gamma = 1.15$, and $\gamma = 2.29$. As can be seen, the height/width ratio of the islands decreases from left to right. Hence with increasing γ , t_{touch} is delayed. For t_{touch} the following relation with γ is found: $t_{touch} \propto \gamma$ (s. Eqn. 12.8).

Fig. 12.7 presents the simulated maximum height $z_{max}(t)$, $\sigma(t)$ and $S(t)$ for $\gamma = 0.44$, $\gamma = 1$, and $\gamma = 2.29$.

Comparing Fig. 12.7 with Fig. 12.4, the general shape of the curves is as before. In case of $\gamma = 2.29$, the constant regime is not reached. This is related to the fact that t_{touch} is larger than the simulated time range.

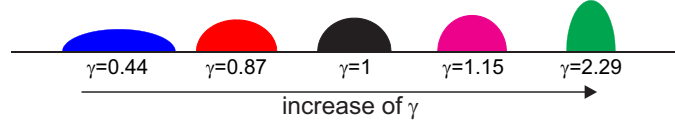


Figure 12.6: Islands with different shapes defined by $\gamma = 0.44, \gamma = 0.87, \gamma = 1, \gamma = 1.15,$ and $\gamma = 2.29$ at the same deposition time t . The distance $L = 30$ nm is kept constant.

The same scaling behavior for γ as for L is found:

$$z_{max}(t) \propto \begin{cases} \gamma^{1/2} & \text{for } t < t_{touch} \\ const. & \text{for } t \geq t_{touch}. \end{cases} \quad (12.18)$$

Hence with increasing γ , the maximum height increases.

Using Eqn. 12.13, the roughness $\sigma(t)$ can be expressed by

$$\sigma(t) \propto \begin{cases} \sqrt{\gamma^{3/2} - \gamma} & \text{for } t < t_{touch} \\ \gamma & \text{for } t \geq t_{touch}. \end{cases} \quad (12.19)$$

As in the case of different distances L , the roughness increases with increasing γ .

The surface coverage $S(t)$ is related to γ by

$$S(t) \propto \begin{cases} \gamma^{1/2} & \text{for } t < t_{touch} \\ const. & \text{for } t \geq t_{touch} \end{cases}. \quad (12.20)$$

With increasing γ , the surface coverage decreases. This is a result of the smaller widths of the islands for larger γ .

In Fig. 12.8, the calculated *in situ* XRR curves are presented.

The same behavior for the *in situ* simulations is found as in case of changing L . Independent of γ , regular oscillations with constant period and amplitude are visible for $t > t_{touch}$.

The period of the oscillation increases up to $t = t_{touch}$.

The calculation show, that the damping of the oscillations decreases with increased γ .

This is a result of the higher roughness of the film at lower γ .

For all *in situ* measurements, the intensity decreases in the beginning. This can be attributed to the low surface coverage for all islands at the constant $L = 30$ nm.

By changing either the shape γ or the distance L of the islands, the same scaling behavior is found. Hence the observed changes in the here presented *in situ* XRR curves are related to different shapes or distances of the islands.

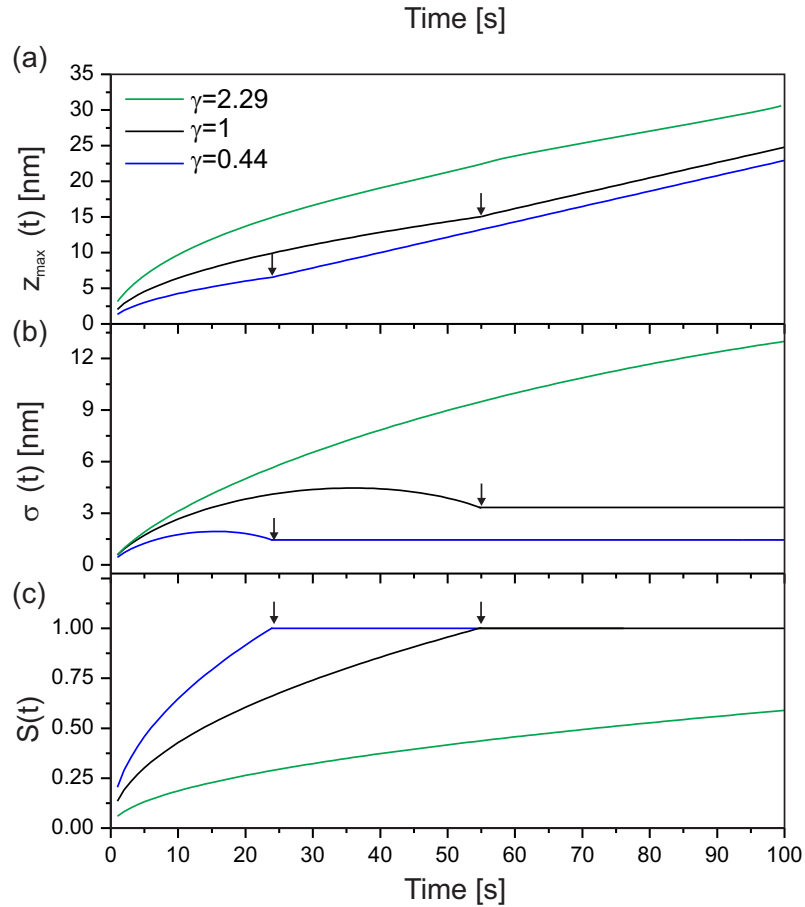


Figure 12.7: Time-development of (a) the maximum thickness $z_{max}(t)$, (b) roughness $\sigma(t)$ and (c) surface coverage $S(t)$ for $\gamma = 0.44$, $\gamma = 1$, and $\gamma = 2.29$ at a fixed distance $L = 30$ nm. The moment t_{touch} , when the islands touch is indicated by black arrows.

This indicates that for a clear statement in case of experimental data, the use of complementary methods is necessary.

As a next step, the influence of time-dependent deposition rate are investigated in the next section.

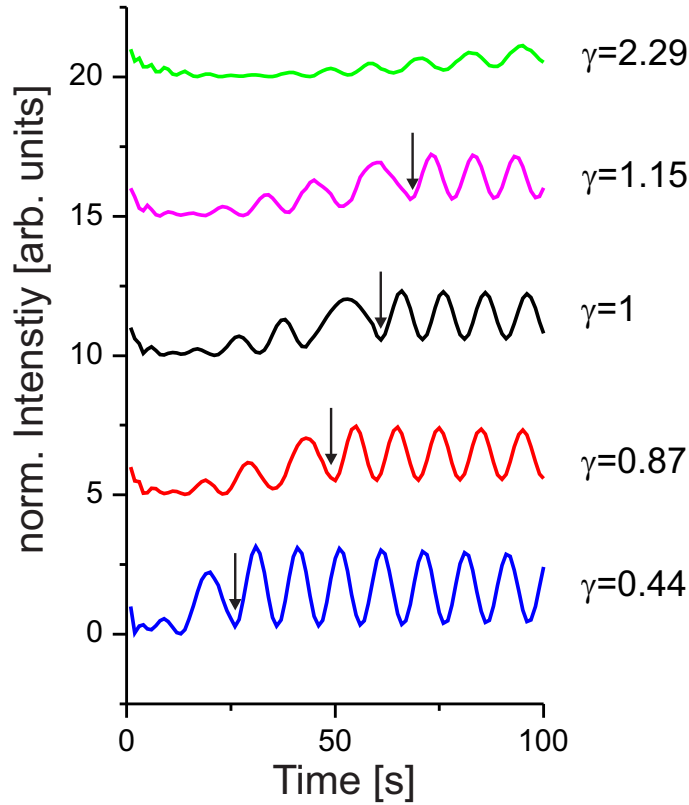


Figure 12.8: Calculated *in situ* XRR measurements of the growth models at fixed deposition rate $\Delta F=0.215$ nm/s and fixed distance $L = 30$ nm with different shape (defined by γ) of the islands. The curves are all shifted by a constant value for better comparison.

12.4 Influence of the deposition rate

In the two previous section, the influence of L and γ on the *in situ* data was presented. In both studies, the deposition rate was constant. $\Delta F = 0.215$ nm/s was chosen. This value corresponds to the deposition rate determined for VC_{1-x} for an applied power of 200 W and very low pressure conditions of $p=0.2$ Pa (s. Chaps. 9 and 10). The deposition rate however can change in time during the initial sputter deposition.

For the investigation, how a time-dependent deposition rate influences the *in situ* XRR curve, the power-, pressure- and time-dependent deposition rate $F(t,p_0)$ were used (s. Fig. 11.3).

The distance $L = 30$ nm and the shape $\gamma = 0.44$ were kept constant.

The calculated *in situ* XRR curves are presented in Fig. 12.9. For comparison, a simulated curve using a constant deposition rate is presented (black line).

At a constant deposition rate, the film forms a closed layer after $t > 50$ s. Due to the new applied deposition rate, this moment in time shifts with increasing pressure. The

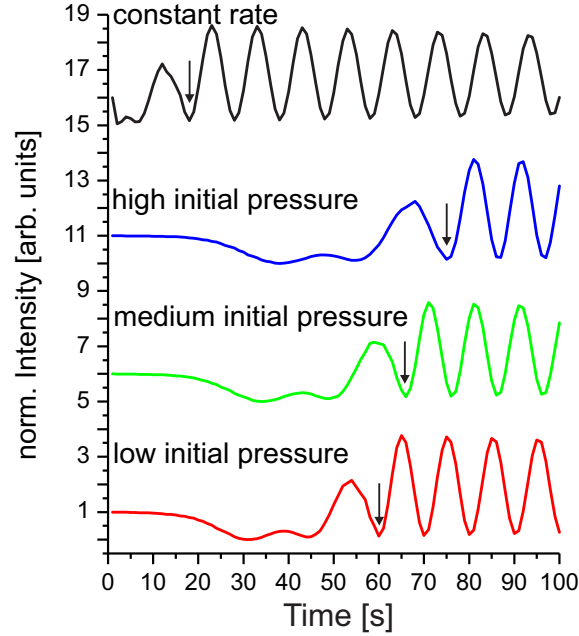


Figure 12.9: (a) $F_{new}(p,P,t)$ for the three different pressure conditions. For comparison the constant rate is indicated by black line. (b) Simulated *in situ* XRR curves with the different $F_{new}(p,t)$. $L = 30$ nm and $\varepsilon = 0.9$ are kept fixed. For comparison, the simulated *in situ* curve at a constant deposition rate $\Delta F = 0.215$ nm/s is additionally presented. t_{touch} is indicated by black arrows. The curves are shifted for better comparison.

moment, when the period of the oscillations is constant, delays with increasing pressure.

12.5 Comparison with the experimental data

Depending on the initial pressure, different characteristic features of the experimental *in situ* data were observed (s. Fig. 11.1). Although the here presented growth model bases on a simple island model, some characteristic features could be reproduced:

Changes in the period τ were observed in the *in situ* XRR measurements. However, when the steady growth regime was reached, periods with constant τ were identified.

The simulations showed that when the islands grow in size, growth oscillations with varying period length are observed. When a closed film is formed, the period of the oscillations is constant. Hence, by investigating the period length, different growth regimes can be directly distinguished.

An increase in intensity in the experimental data at the beginning of the sputter process was observed. Considering the layer model, a higher density of the growing film is expected (s. Chap. 8). The simulations based on the growth model showed, that an

intensity increase in the beginning occurs, if the surface coverage is higher than 50 % for the here presented material system. This indicates, that independent of the pressure, in the beginning of the sputter process, the Si substrate is covered by at least 50 % of VC. This characteristic feature allows a instant feedback of the nucleation behavior.

However, not all characteristic features could be reproduced: The experimentally observed increase in the mean value at *low* and *medium* initial pressure was not observed in the simulations. This is due to the simplified model. The model does not allow any changes in roughness, when a closed film is formed. Moreover, does not cover any inter diffusion process of the islands and neglects completely the influence of composition-induced re-nucleation processes.

Nevertheless, some characteristic features of the *in situ* curve were already reproduced. This confirms, that the film formation in the initial growth regime cannot be described by a simple layer model, as determined by post-growth XRR measurements. During the initial growth, changes in the in roughness, density and thickness influence strongly the *in situ* XRR data. Therefore simulations based on growth models are necessary for a deeper understanding.

12.6 Summary

In this chapter, the influence of the microstructure formation during the initial growth regime on the *in situ* XRR curve was investigated. Therefore, simulations based on a 2D island model were performed.

The distance L , the shape γ and the deposition rate F_D were systematically changed. The models were used for the calculation of *in situ* XRR curves.

Scaling laws for the maximum height, roughness and the surface coverage were determined - depending on L and γ . The same scaling behavior was found. This indicates, that microstructural changes due to different shapes or distances of the islands can not be distinguished. Hence, investigations of the microstructure using complementary methods is necessary.

A comparison with the experimental data showed, that simulations based on a simple growth model can already reproduce characteristic features of the *in situ* XRR. The here presented approach allowed gaining insight in the fundamental understanding of *in situ* XRR curves during complex growth conditions.

13 Tailoring the microstructure

The growth of multilayer thin films is a well-known method to tailor the optical, tribological and mechanical properties of a material. For hard coating materials, the fabrications of multiphase crystalline/amorphous multilayer systems are an interesting option to enhance the hardness of the coating [Stu09].

Multilayer systems are usually grown by alternating layers with different chemical composition, resulting e.g. in different average densities of the two layers (s. Chapter 2).

As shown in chapter 11, the growth conditions can influence the average density of a layer. By the controlled variation of the deposition parameters, a multilayer systems might be formed during the deposition using only a compound target. Moreover, it should be possible to observe the growth of multilayer systems directly by the temporal changes in the intensity. This approach is presented in this chapter. The influence of periodic interruptions of the growth process on the microstructure is monitored by *in situ* XRR measurements. The grown film is investigated by angle-dependent XRR measurements and TEM analysis.

13.1 Periodic interruption of the growth process

If the growth takes place already during the high pressure regime in the beginning of the deposition, an interface layer is grown (as shown in Chapter 11). Hence by sequentially repeating this growth procedure, a multilayer structure might be achieved.

In situ measurements are very sensitive to changes in the electron density (s. Chap. 11). The growth of a multilayer system should be directly observed by the changes in the intensity. Hence, during the deposition, the microstructure formation was monitored by *in situ* XRR measurements.

In Fig. 13.1 the time-dependent changes of the specular intensity during the whole deposition time of 200 s is shown. The experimental data, measured during the deposition periods 2,5,6, and 7 are presented.

The *in situ* measurements for each deposition period are very similar. The periodic signal indicates already the successful growth of a multilayer structure.

Comparing the period τ of the growth oscillations, an identical behavior is found. However, slight differences in the amplitude and the mean value are visible.

Especially in the first 20 s of the deposition period 1, the intensity of the *in situ* curve increases fast. For the later deposition periods, a decrease in intensity is visible.

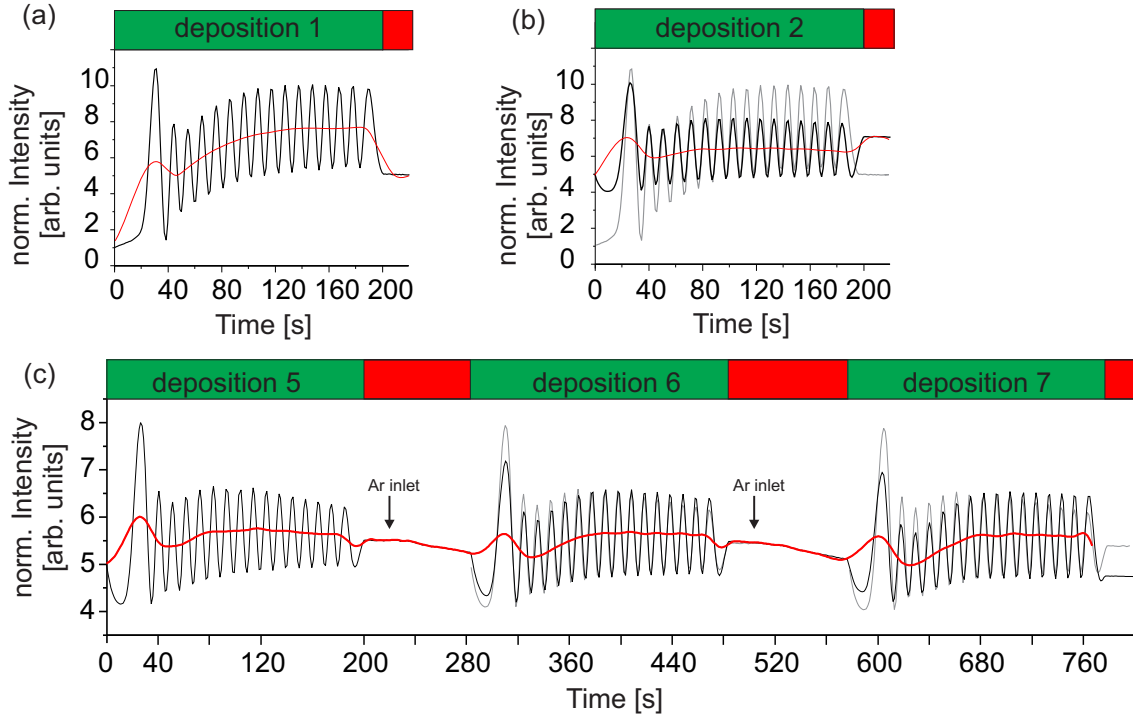


Figure 13.1: *Stationary* measurements during the (a) first deposition, (b) second deposition and (c) deposition periods 5-7. The *in situ* XRR data of the first deposition is presented in (b) for better comparison. The *in situ* data of the 5th deposition is presented in deposition period 6 and 7 for better comparison. The mean value is shown by red lines.

This can be explained by the fact, that the first period is deposited on the silicon substrate. As shown in Chap. 11, the intensity in the beginning is influenced (1) by the surface coverage of the $VC_{1-x}/a-C$ film and (2) by the higher electron density of $VC_{1-x}/a-C$ compared to the Si substrate.

The later periods are grown on top of $VC_{1-x}/a-C$ film. If growing a less dense layer on top of a more dense layer, a decrease in intensity is expected (s. Chap. 8). This indicates, that an interface layer is grown, which has a smaller electron density.

Comparing only the deposition periods larger than 2, the *in situ* XRR curves for the later periods are very similar. Not only the period of the growth oscillations is identical, additionally the amplitude and the mean value are comparable. This supports the interpretation, that the changes in the *in situ* curve for the depositions are mainly due to the different underlying layer.

When the deposition process is stopped, the intensity stays first constant. 60 s before the next plasma ignition, the intensity decreases first very slowly, then a slight decrease in intensity is visible.

This is related to the period of time, when the Ar gas is let in the chamber. However,

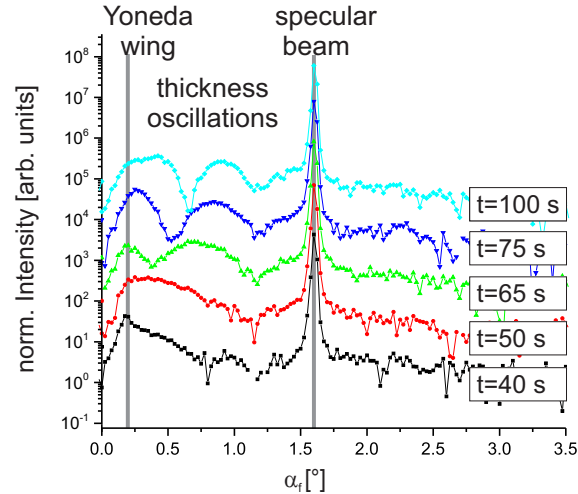


Figure 13.2: Line profiles of the intensity at different deposition times during the growth of $LP-a(2.5)$

this decrease in intensity is not observed for the first period. This might be related to Ar physisorption on the grown $VC_{1-x}/a-C$ film, which is different for Ar to Si.

[Jan07] investigated the physisorption of Ar in transition-metal-doped silicon clusters. They showed, that Ar complexes are only formed at positions of transition metals atoms by van-der-Waals binding. No binding of Ar was observed in case of pure silicon. They showed, that physisorbed Ar changes the morphology of the film. The roughening of the layer might explain the decrease in intensity.

In summary, the *in situ* XRR measurements for all deposition periods are similar. Slight changes in the amplitude are visible for the first deposition period. This can be explained by the fact that this deposition period is deposited on the Si substrate.

In the diffuse scattering, characteristic features are observed if measuring a multilayer structure with correlated roughness (s. Chap. 3). In the following, it will be shown, that monitoring the diffuse scattering during a multilayer growth gives instant feedback of an successful periodic modulation of the microstructure.

The used 2D PILATUS detector measured besides the specular beam directly the diffuse scattering (s. Chap. 5). For the presentation of the diffuse scattering, time-dependent reflectivity maps were generated.

From each PILATUS images, a line profile of the intensity was extracted for each time step. Fig. 13.2 presents various line scans at different deposition times.

The specular beam is located at $\alpha_{fix} = 1.6^\circ$. Characteristic features in the diffuse scattering are observed (s. Chap. 3). The Yoneda wing appears at $\alpha_f = \alpha_c$ and gives a direct measure of the electron density. It is located around $\alpha_f \approx 0.225^\circ$. This corresponds well to the expected value of α_c of the $VC_{1-x}/a-C$ thin film (s. Chap. 10).

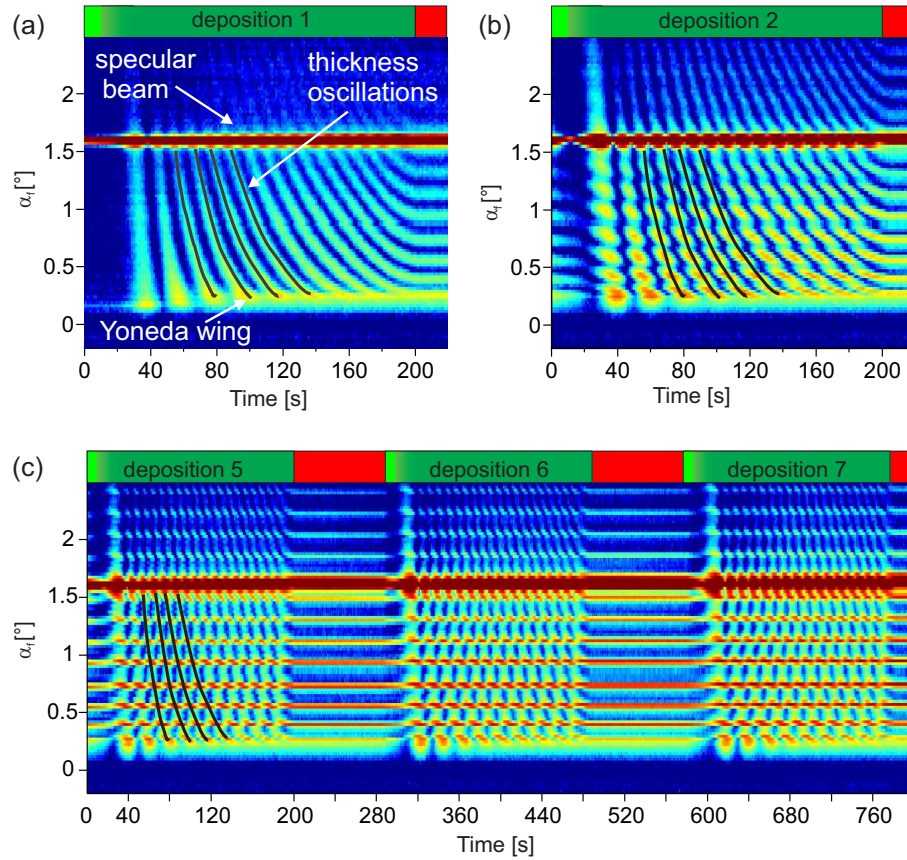


Figure 13.3: *In situ* XRR maps during the (a) first deposition, (b) second deposition and (c) deposition periods 5-7. The bending of the stripes is denoted by black lines.

In the angular range between the Yoneda wing and the specular beam, fringes appear. The fringes in the diffuse scattering occur if the roughness of the coating and the substrate are correlated. They are related to the thickness of the film. With increasing thickness, the period of the fringes decreases.

The experimental data are summarized in a matrix, where each column corresponds to one line profile, each row to one time step.

The time-dependent XRR map during the first deposition period is presented in Fig. 13.3 (a). The intensity is presented in logarithmic scale. The colorscale was chosen in order to enhance the diffuse scattering. Hence, the much more intense specular beam appears only as a red bar.

Stripes in the diffuse scattering are visible, which bend with deposition time. They correspond to the above-mentioned thickness oscillations. The bending of the stripes is a result of the decrease in the period of the fringes with increasing deposition time. The Yoneda wing shifts to higher values at the beginning of the deposition. This corresponds

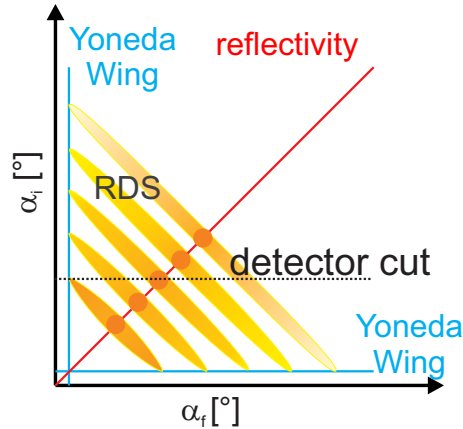


Figure 13.4: Scheme of the diffuse scattering map for a multilayer system with correlated roughness in angular space. The detector in the here used experimental setup cuts the reciprocal space (denoted by black dotted line).

to the growth of the much more dense $VC_{1-x}/a-C$ film on the silicon substrate.

In Fig. 13.3 (b) and (c), the *in situ* map measured during the second and the 5-7th deposition period are shown.

The *in situ* XRR maps of the periods beyond the first deposition show the same bending of the stripes (black lines). However, the intensity along the streaks is modulated. With increasing number of deposition, these peaks are more and more intense and pronounced.

For multilayer systems with correlated roughness of the layers, intensity stripes are visible in the diffuse map at the multilayer peak position of the specular beam (s. Chap. 3).

The line scans used for the generation of the *in situ* maps correspond only to a cut through reciprocal space. This is schematically shown in Fig. 13.4. The peaks visible in the stripes are hence related to the cut through the sheets of resonant diffuse scattering. Their position and width is determined by the location of the multilayer peaks in the specular position.

With increasing number of multilayer periods, the intensity of the resonant diffuse scattering increases. Hence the observed modulation of the stripes is related to multilayer peaks.

Furthermore, for all depositions, a shift of the Yoneda wing to higher angles is observed. For the first deposition, this is explained by the deposition of the more dense $VC_{1-x}/a-C$ on Si substrate.

For the later deposition, -as indicated by the observations of the specular reflected beam-, the interface layer has a smaller electron density compared to the following film. This leads to shift of the Yoneda wing from smaller to larger angles.

In summary, monitoring the diffuse scattering gives instant feedback of the periodic modulation of the microstructure.

In this experimental setup, not the entire reciprocal space is measured. However, this is not necessary, since the cut through the reciprocal space gives the directly the desired information: The direct visualization of the multilayer peaks, which increase in intensity with the number of deposition period. This allows instantaneously the conclusion, that a period structure was successfully grown. This was done by a simple deposition process using only one target.

The successful growth of a multilayer structure is additionally proved by angle-dependent XRR measurements and HRTEM analysis. This is presented in the next section.

13.2 Confirmation of the multilayer structure after deposition

The temporal changes in the diffuse scattering showed unequivocally the existence of a multilayer structure. In this section, angle-dependent XRR measurements and a HRTEM analysis are presented to emphasize this statement.

Angle-dependent XRR measurements after single deposition periods were directly performed after the deposition. Fig. 13.5 compares the measurements after the first, second, seventh, and tenth deposition period. The characteristic peaks in an XRR measurement of a multilayer structure are visible after the second deposition. They are denoted by the black dashed lines in Fig. 13.5 (a). Highlighted regions of the measurements are presented in Fig. 13.5 (b).

The angular spacing of those multilayer peaks depends on the thickness of the individual layers. For the first seven deposition periods, these multilayer peaks are located at the same position as the Kiessig fringes after the first depositions. This indicates, that the individual layers are similar. However after 7 depositions, a broadening of multilayer peak is observed. After 10 depositions a slight shift in the multilayer peak positions is visible for larger $q_z > 0.25 \text{ \AA}^{-1}$. Both indicates that the multilayer system is not perfectly periodic.

Besides the multilayer peaks, oscillations arising due to the interference of the total thickness of the film with the substrate are visible (s. Fig. 13.5 (b)).

For multilayer systems with $n > 2$ bilayers, $n - 2$ oscillations due to the total thickness between the multilayer peaks positions are expected [Pie04, AN11]. However, this is not observed in case of the XRR measurement after the seventh and tenth deposition period. For a better understanding of the measurements, simulations were performed.

In Fig. 13.6 (a) the angle-dependent XRR measurements and their simulations after the 1st, 2nd, 7th and 10th deposition period are presented.

For the simulations, a layer system was used. The input parameters are given in Tab.

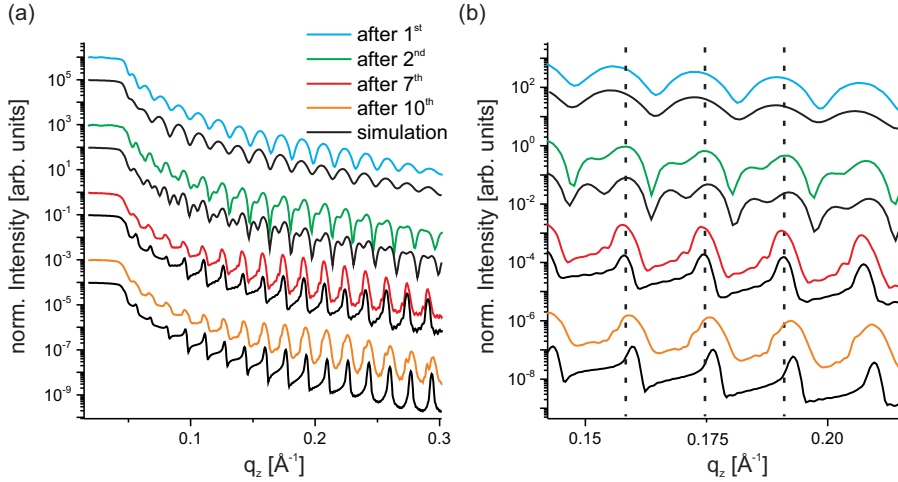


Figure 13.5: (a) Reflectivity measurements (color) and their simulations (black lines) after the deposition periods 1,2,7, and 10. (b) Highlighted region of the XRR measurements and their simulations. The multilayer peaks are indicated by black dotted lines. The curves are shifted for better comparison.

Layer	D [nm]	σ [nm]	ρ_e [g/cm ³]
Period 1			
I	8.10	0.57	4.68
II	28.50	0.36	5.10
Period 2-10			
I	7.50	0.50	4.68
II	28.50	0.36	5.10
III	0.80	0.10	2.90

Table 13.1: Thickness D , roughness σ and electron density ρ_e for the different layers, used as input for the simulation of the XRR measurements.

13.1.

As a first approach, a 2 layer system (layer I and layer II) was used to fit the XRR reflectivity measurements using the results of Chap. 11. This bilayer system was repeated taking into account the number of deposition periods. In Fig. 13.6(a), the simulated curve after the 7th growth period based on this model is shown in black. The experimental data is presented as red curve. As can be seen, the agreement of experimental data and simulation is not good. A weak peak intensity is visible

For achieving good agreement with the experimental data, a third layer (layer III) was introduced at the interface between the high density layer II and the low layer I. Layer

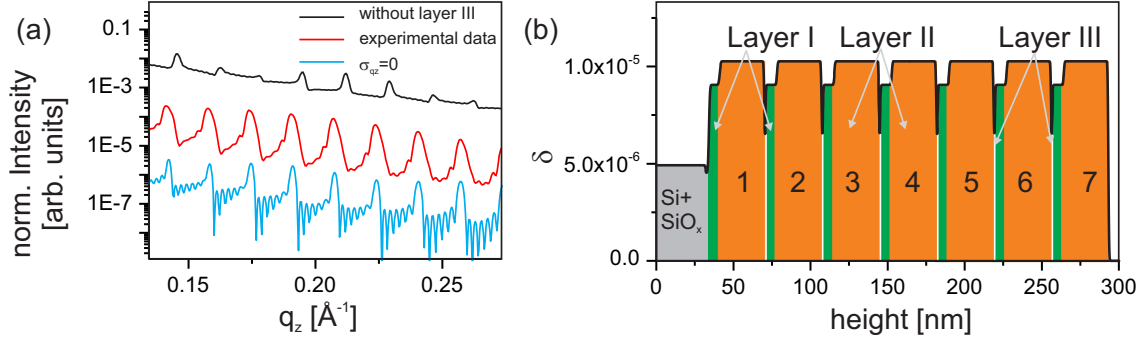


Figure 13.6: (a) Experimental Data of the XRR measurements after deposition period 7 (red curve). Simulated XRR curve without layer III (black curve) does not agree well with the experimental data. Simulated XRR curve without considering the resolution. All $n - 2$ Kiessig fringes due to the total thickness are resolved. (b) δ -profile based on the simulation input. The individual layers are highlighted by color (Si substrate+SiO_x:gray, Layer 1: green, Layer 2: orange, Layer 3: white)

III has a very low density and a thickness below 1 nm.

For achieving a good agreement with the experimental data, the thickness of layer I was reduced for the periods 2-10. This might indicate that layer III grows on expense of the layer I.

The simulations including a third layer lead to a good agreement with the experimental data. However, after 7 deposition periods, the multilayer structure is not perfectly modulated. This leads to a slight deviation between data and simulation, since a period modulated layer system was used for the fitting.

The experimental data showed, that not all oscillation due to the total thickness of the film are resolved. Therefore, the simulations were repeated, considering no resolution element (s. Fig. 13.6 (a), blue curve). As can be seen, without resolution $n - 2$ Kiessig fringes are resolved. Hence, the missing oscillations are not only due to the slight deviation of the period modulation, but additional due to the resolution of the experimental setup.

In Fig. 13.6 (b) the δ -profile used for the fit of the 7th period is presented. As can be seen, layer III leads to a sharp dip in the δ -profile.

Layer III might be a result a slight changes in the nucleation behavior. As mentioned before, the deposition periods 2-7 are grown on top of VC_{1-x} surface and not on the silicon substrate. Furthermore, the nucleation behavior might be influenced by the interruption of the growth process. It might be related to a layer of incorporated Argon. The latter would be in good agreement with the observations of the *in situ* XRR measurement. Here a decrease in intensity was observed during the insertion of the sputter gas.

Fig. 13.7 (left) shows schematically the model of the multilayer for the total of 10

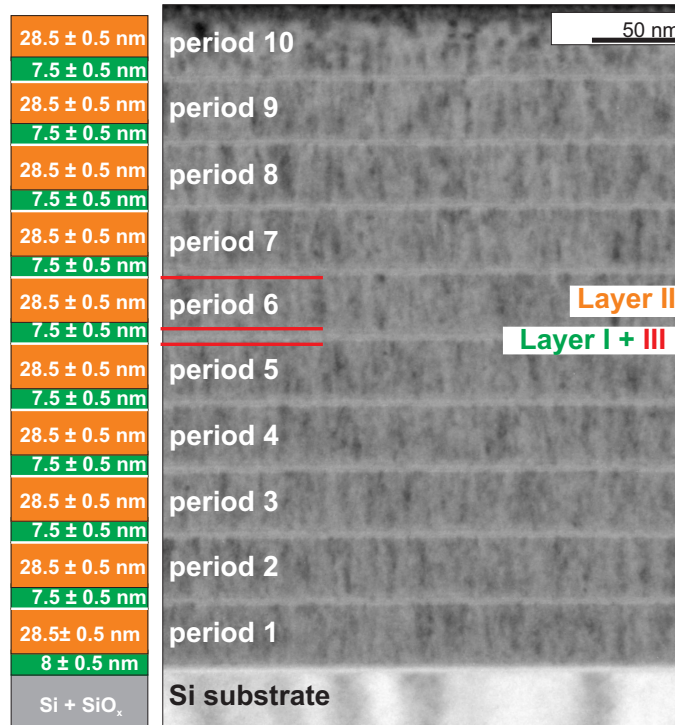


Figure 13.7: Model of the multilayer structure based on the results of the XRR analysis (left). TEM cross section of the multilayer after 10 periods (right). The different layers are indicated in period 6 in the images.

deposition periods. Layer III is indicated by a white line.

The dark-field cross section image in Fig. 13.7 (right) proves the high quality of the multilayer system. For period 6, the three layers are indicated in the image. Therefore the thickness of the layers from the simulation input for the angle-dependent XRR was used. The elongated nanocrystallites of layer II are clearly visible. Underneath, a bright region around the layers I and III is visible.

As can be seen, the grain structure repeats periodically. By interrupting the deposition process, the growth was restarted in the same way.

In summary, XRR and TEM measurements after the deposition confirmed the results of the *in situ* analysis. By periodically interrupting the growth process, a multilayer structure was successfully grown.

The interface layer were grown due to the variation of the gas pressure after plasma ignition. The influence of the growth interruptions on the microstructure formation is investigated in the next section.

13.3 Influence of the growth interruption

In the previous section, the successful growth of a multilayer structure was presented. For achieving a periodic modulation, the growth was intentionally interrupted. This rises the question how the growth interruption influence the microstructure formation. Therefore, another sample, *gas-ML*, was deposited. The pressure was modulated as before, but without interruptions of the growth process.

In Fig. 13.8 the development of the working gas pressure (a), the *in situ* measurements of (b) *LP-a(2.5)*, the *interruption* multilayer, and (c) the *in situ* XRR of *gas-ML*, the *non-interruption* multilayer, for the deposition periods 1-3 is presented. For better comparison, the time, at which the no deposition took place for the *interruption* multilayer, is shaded in gray.

The *in situ* measurements of the *non-interruption* multilayer show a periodic behavior. However, with increasing deposition period, the intensity decreases.

For the first 190 s, the sputter conditions for both samples are comparable. In both cases, the *in situ* curve oscillate with the same period τ . The development of the mean value is similar. The mean intensity of the *non-interruption* multilayer and the amplitude is slightly higher, which is a result of the slight variation in the pressure in the beginning (s. Chap. 11).

After 200 s, however, the deposition the *interruption* multilayer was interrupted. This is not the case for the *non-interruption* multilayer. Here the deposition period is longer. It includes an additional growth regime during the increase of the pressure.

In the following the changes of the *in situ* XRR curve during this additional growth period are described (s. Fig. 13.8 (c)).

With increasing pressure, the amplitude decreases with time. A similar decrease in amplitude was found for the sample, grown at *high* initial pressure. This indicates a strong increase in roughness of the film.

When the pressure is reduced, the amplitude increases again. However, the total intensity is lower than for the first period. This indicates, that the multilayer structure is much more rough compared to the *interruption* multilayer.

A similar behavior is found for the mean value, which changes inversely to the pressure. Changes in the period τ of the single oscillations are observed during the pressure variations. For better visibility, this region is highlighted in Fig. 13.9 (a).

The period of each oscillation was fitted using a $\cos(\omega t)$ -function (s. Chap. 9). The rate of the thickness increase, F_D , was calculated using Eqn. 8.8. The result is shown in Fig. 13.9 (b). At low pressure, $F_D = 0.216$ nm/s corresponds to the expected value of the thickness increase at 200 W DC Power (s. Chap. 9). With increasing pressure, F_D decreased. With decreasing pressure, F_D increased again. When the pressure was sufficiently reduced at $t \approx 400$ s, the rate of the thickness increase was again at $F_D = 0.216$ nm/s. This behavior was visible for each deposition period.

Based on the Keller-Simmons formula (s. Chap. 1), the time- and pressure-dependent

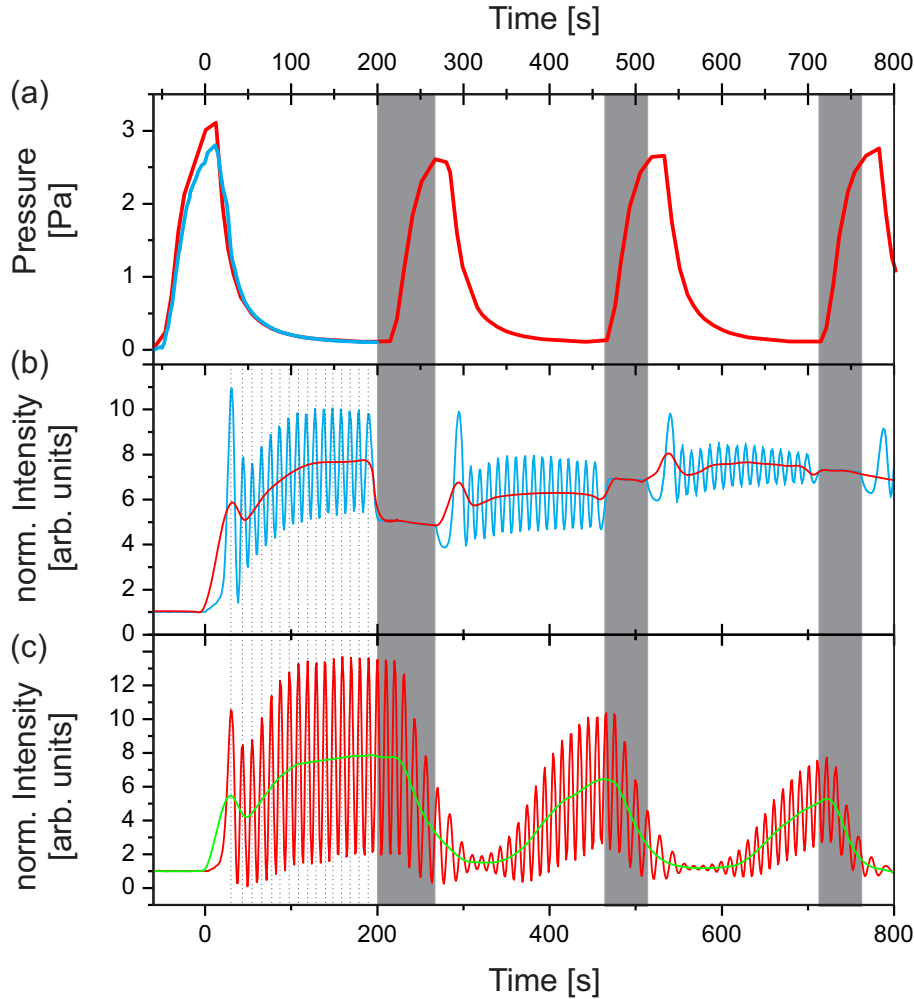


Figure 13.8: (a) Development of the working gas pressure of *gas-ML* and the first period of *LP-a* (2.5). *In situ* measurements during the first three periods of *LP-a*(2.5) (b) and *gas-ML* (c). The mean value is indicated by a green line. The minima of the growth oscillations are highlighted by dotted lines for better comparison for the first period.

changes in the deposition rate were calculated. The result is presented in Fig. 13.9 (b), red dots. As can be seen, the development of the time-dependent deposition rate and F_D are similar. However, the deposition rate is much lower compared to the rate of the thickness increase. This might indicate the growth of a porous film.

In addition to the *in situ* measurements, angle-dependent XRR measurements were conducted after the 10th period, presented in Fig. 13.10 (a). For comparison, the XRR measurement of the *interruption* multilayer after deposition period 10 is presented.

Also for the *non-interruption* multilayer, multilayer peaks are visible, indicating the peri-

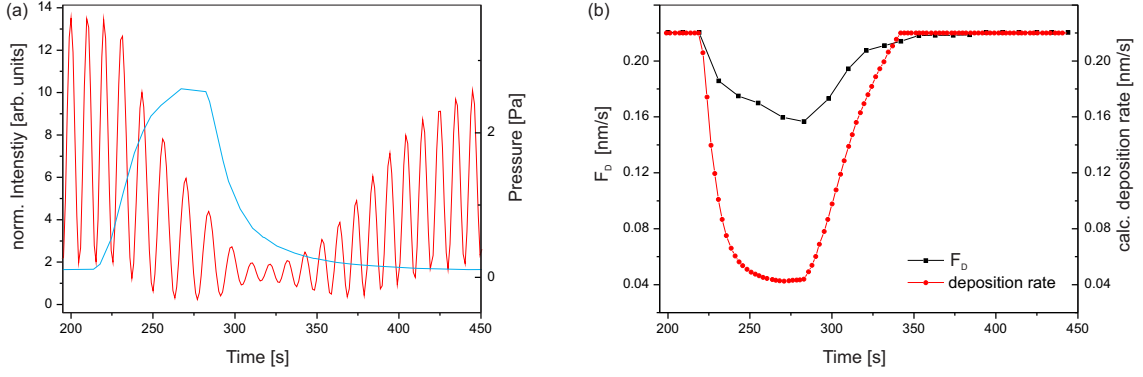


Figure 13.9: (a) Experimental *in situ* data during the variations of the gas. The amplitude is strongly damped and the period of the oscillation is changing. (b) Estimated rate of thickness increase from experimental data (black squares) and calculated deposition rate (red circles) during the pressure variations. F_D and the deposition rate decrease with increasing pressure.

Layer	D [nm]	σ [nm]	ρ_e [g/cm ³]
Period n=1			
I(n)	8.10	0.57	4.68
II(n)	31.00	2.20	5.10
Period n = 2-10			
I _b (n)	23.30	(1.10 + n · Δσ)	4.50
II _b (n)	28.20	(2.20 + n · Δσ)	5.10

Table 13.2: Thickness D , roughness σ and electron density ρ_e used as input parameter to simulate the angle-dependent XRR measurement of the *non-interruption* multilayer. The roughness was increased by $\Delta\sigma = 1\text{\AA}$ for each period n to account for the roughening of the system.

odic modulation of the density (denoted by arrows in Fig. 13.10). The oscillations due to the total thickness of the *non-interruption* multilayer are not so pronounced compared to the *interruption* multilayer. Furthermore, the intensity of the *non-interruption* multilayer decreases much faster than *interruption* multilayer.

Simulations of the angle-dependent XRR measurements were performed using a simple layer system as model. The input values are presented in Tab. 13.2. For the choice of the input parameters, the results of the analysis of the *in situ* measurements were used: Since the growth of the first bilayer is comparable to the deposition period 1 of the *interruption* multilayer, the same values were chosen. The thickness of layer II was increased due to the 20 seconds longer growth at low pressure conditions (s. Fig. 13.8). For the

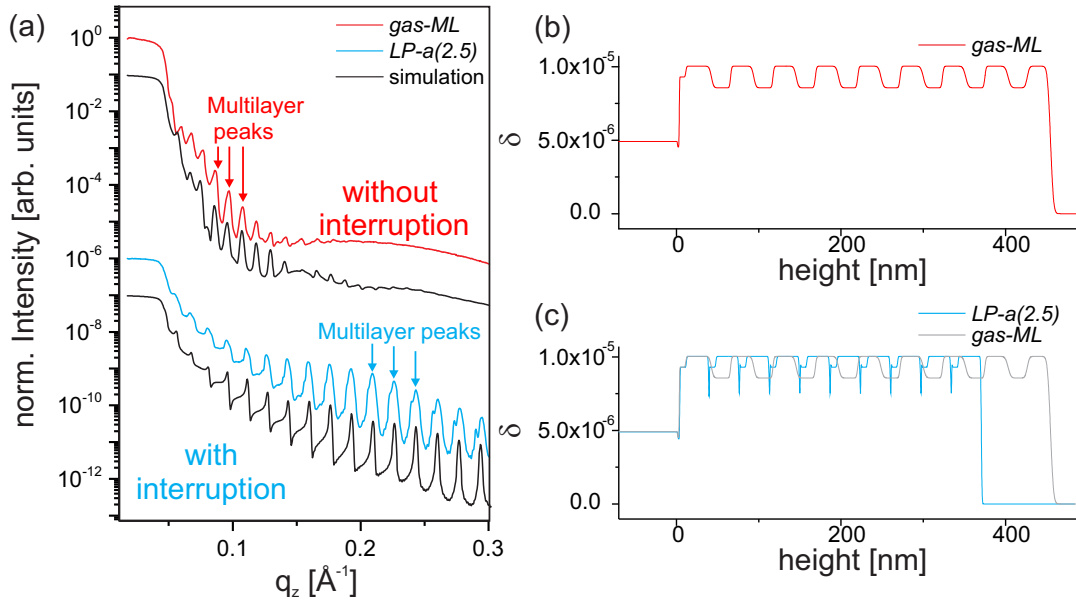


Figure 13.10: Experimental data and best simulations of angle-dependent XRR measurements of *LP-a(2.5)* and *gas-ML* after the deposition of the 10^{th} period. The curves are shifted for better comparison. (b) and (c) δ - profiles used for the simulation of the XRR data for both samples.

following deposition periods, a two layer system was introduced (layers I_b and II_b). It is assumed, that layer I_b grows during the high pressure, while layer II_b is deposited during low pressure conditions.

Because of the high pressure, for layer I_b , a higher roughness $\sigma = 1.1$ nm was assumed. The density of this layer was slightly reduced compared to layer I to achieve a better agreement with the experimental data. By doing that, the slope of the curve was better reproduced.

For layer II_b , the properties of the film were adapted to layer II. However, for the second deposition already a higher roughness is expected, since the amplitude of the *in situ* curve was strongly damped. Therefore, σ was increased to 2.2 nm for the second deposition period.

For each period, σ of the layers I_b and II_b were increased by $\Delta\sigma = 1$ \AA to account for the roughening of the system.

The resulting δ -profile is presented in Fig. 13.10 (b). The position of the critical angle, the multilayer peaks, and the general shape of the XRR curve are well reproduced. However, the simulations do not fit perfectly the experimental data. Although main features are reproduced, the here applied model is too simple to account for the microstructure formation during the complex pressure variations. For comparison, Fig. 13.10 (c) presents the δ -profile of *interruption* multilayer after the 10^{th} period. The δ -profile is only iden-

tical for the first deposition period with the one of the *interruption* multilayer system. The thickness of the bilayer system of 52.6 ± 1 nm is larger than for the *non-interruption* multilayer than 38 ± 1 nm for *interruption* multilayer (s. previous section). While the δ -profile of the *interruption* multilayer showed sharp interfaces, the transition of the individual layers in case of the *non-interruption* multilayer is smoother.

In summary, by only tuning the gas flow, a multilayer system was successfully grown. This shows, that the here presented multilayer structures are achieved by the controlled variation of the pressure.

Compared to the multilayer structure, obtained by growth interruptions, the *non-interruption* multilayer is much rougher. The interruptions of the growth process lead to a sharp interface, since in this case, no deposition takes place during the pressure increase.

13.4 Summary & discussion

In this chapter, the successful growth of multilayer systems prepared by sputter deposition from one target was presented.

The growth was monitored by *in situ* XRR measurements. This allows the non-destructive investigation of the variations of average density of the microstructure during growth.

In addition to the specular beam, temporal changes of the diffuse scattering were presented in this chapter. Instantaneously, the successful growth of the multilayer was observed. Due to the high sensitivity of this method, it can be applied to more complex systems, e.g., a-periodic multilayer systems or gradient samples.

The periodic modulation of the microstructure was confirmed by XRR and TEM after growth.

It was shown, that variations in the working gas pressure are the main driving force for tailoring the microstructure. Interruption of the growth process leads to smooth layers, while tuning of the gas flow results in a rough multilayer structure. This is related to the additional deposition during the pressure increase in the chamber.

By the variation of the pressure, the C/V ratio is tuned (s. Chap. 11). This in turn influences the texture, the roughness and the electron density of the film.

Most multilayer system reported in literature are grown by the alternation of layers of different materials. However, few multilayer systems, where only one material system was used, are found.

[Bul96] tried to achieve a Ti-N multilayer system using reactive sputtering from a Ti target. The N_2 flux was kept constant, the bias was systematically changed. Although the films showed enhanced properties compared to a single layer, the multilayer structure was not confirmed by SEM and XRR.

[Yoo96] claimed to have successfully grown a multilayer system by alternating the growth temperature during deposition of a-Si:H. However, the multilayer structure was again not confirmed.

Microstructural changes can be achieved by changing the deposition angle during the deposition. Here, the density contrast is generated by dynamical shadowing growth. This can lead e.g. to so called zig-zag, nanosprings or nanoball structures. This approach has been successfully performed for several material system e.g. using Cu, Si and W [Kar04], or Si [He11]. More successful approaches are found for diamond-like carbon systems. [Lai11] used two different deposition techniques in one chamber (RF-sputtering and PACVD), to grow a multilayer structure. Although the multilayer structure was confirmed by TEM, the entire deposition process is very complicated. By applying two different deposition techniques, the chemical bonding of the C was switched from C from $1sp_2$ (Soft Carbon) to $1sp_3$ (Hard Carbon). The same mechanism (Soft Carbon \leftrightarrow Hard Carbon) was exploited by [Li11]. By changing the bias during sputter deposition, the microstructure of the layers was changed due to switching of the bonding of C. Due to the different bonding, the microstructure is strongly affected, leading to the wanted density changes.

The here presented multilayer systems were prepared by a very simple deposition process. This growth procedure should be applicable to other material system, provided that (1) the involved elements differ significantly in their mass and (2) phase separation can occur. By using a monocarbide of a transition metal, this multilayer systems have a good adhesion to a metallic substrate. This is not the case for pure C multilayers. Therefore the here presented multilayer system could be used for e.g. wear-resistant protective coatings of cutting tools.

Summary & outlook

In this work the film formation of V-C prepared was monitored by *in situ* XRR measurements during sputter deposition from a compound target. For this the *in situ* measurements were methodically optimized for application-relevant growth conditions, dealing with high deposition rates and long deposition times. This method was used for the investigation of the influence of the DC power and the working gas pressure on the V-C film formation.

As a first step, for optimization of the *in situ* XRR method, experimental data of two measurement types during sputter deposition were collected under identical growth conditions. It was shown that *in situ* measurements at a fixed position of the incidence angle, so called *stationary* measurements, are a powerful tool to monitor the thin film formation in case of high deposition rates. A theoretical description of *in situ* XRR data was developed based on the Parratt algorithm and adapted to film growth.

This combined approach enabled a qualitative understanding of the period of growth oscillations and the envelope of the specular intensity. A direct relation between the rate of thickness increase and the period was found. An explicit formula for the estimation of the growth rate was derived. It was shown that changes in the amplitude of the growth oscillations can be attributed to electron density and roughness changes of the film. However, it was found that the experimental resolution (beam divergence) more and more affects the envelope of the measured data with increasing film thickness. A simple rule of thumb depending only on the resolution element was derived in order to estimate a critical thickness above which this resolution effect has to be taken into account. Below this critical thickness, the variations in the envelope can directly be related to microstructural changes.

Taking the resolution element into account enables the online-interpretation of the measured intensity in terms of growth velocity, roughness and electron density changes. This allows gaining insight into the instant response of the microstructure formation to growth parameter changes occurring, e.g., during the deposition of complex gradient samples. Further the theoretical framework developed in this work enables the detailed quantitative analysis of the thickness, roughness and mean electron density changes based on simulations of the growth model. This allowed the calculation of the *in situ* XRR curve and comparison to the experimental data. A direct extraction of the parameters (thickness, roughness and electron density) from the *in situ* data was possible for simple growth processes, where changes only occur at the growth front. Here a layer model was used for the simulations.

For gaining a deeper understanding of more complex growth systems including microstructural changes in the buried layers simulations based on a growth model were performed.

As a second step, the optimized *in situ* technique was used to monitor the growth of V-C films prepared by sputter deposition from a compound target. The influence of the DC power and the working gas pressure on the film formation was investigated. For a comprehensive understanding of the material distribution, the *in situ* results were supported by the use of complementary methods.

For investigating the influence of the DC power on the thin film formation, a time-saving approach was successfully applied: The rate of the thickness increase was extracted from the period of the growth oscillations at different applied DC powers. By doing so, it was found that the rate of the thickness increase is proportional to the applied DC power. HRTEM analysis and simulations of the sputter process indicated no significant changes in the electron density of the film. This led to the conclusion, that the thickness increase of the coating is dominated by the increasing deposition rate due to higher DC power, and not by microstructural changes. This result is in good agreement with the linear relation between power and deposition rate found for single element targets.

Further, *in situ* measurements showed that the working gas pressure does not only influence the deposition rate, but also significantly changes the time-dependent development of the roughness and electron density of the coatings. A reduced deposition rate was observed at high pressure, which can be explained by the increased collision rate of the sputtered particles in the gas phase.

Pressure-induced variations in the C/V-ratio of the films as implied by results of simulations of the sputter process, were confirmed by XPS measurements. The different morphology of the films grown at high and low pressure can be explained by composition-induced variations in the texture.

The results of the above-mentioned *in situ* studies were used to gain insight in the microstructure formation at fast varying deposition conditions. Changes in the initial growth at different initial pressures were directly evidenced in the *in situ* XRR curves. A bilayer growth was identified and confirmed by angle-dependent XRR measurements after growth: The varying growth conditions lead to the growth of a bilayer system. It was found that the interface layers grown on top of the Si substrate, differed in thickness, roughness and electron density, depending on the initial pressure.

For a fundamental understanding of how the microstructure formation in the initial growth regime influences the *in situ* XRR curve, simulations based on a 2-D growth model were performed. Half-ellipsoid islands growing on top of Si substrates were chosen, since TEM cross-section images indicated an elongated fiber structure. When the islands touch, a closed film is formed. The shape and the distance of the islands, as well as the deposition rate, were systematically changed. It was shown that the shape and the distance of the island influence the roughness of the system. This can be directly observed by the strong damping of the amplitude of the *in situ* curve. When a closed layer is formed and changes in the microstructure occur only at the growth front, the period of the oscillations

is constant. This is not the case while the islands are still separated. Hence, in case of island growth estimating the period of the oscillations during an *in situ* experiment can give direct feedback about different growth regimes. Comparison with the experimental data showed that already several characteristic features such as the oscillation period and behavior of the amplitude could be reproduced by this simple model. For a more detailed understanding, the simulations might be optimized by applying more complex models in the future, which could include e.g. the temporal changes in the chemical composition of the film.

The observed interface layer formation during the initial growth was exploited to intentionally grow a multilayer system by the controlled variation of the deposition parameters. The periodic modulation of the microstructure was achieved by subsequently interrupting the deposition process. For investigating the influence of the growth interruption, another sample was deposited, where only the pressure in the chamber was modulated. By doing so, a second multilayer system was successfully grown. This proves that multilayer structure is driven by the pressure-induced variations in the microstructure. Compared to the multilayer structure obtained by growth interruptions, the *non-interruption* multilayer was much rougher. The interruptions of the growth process lead to a sharp interface. In this case, the growth was restarted in the high pressure regime. For production of the multilayer structure, interruptions are favorable, since deposition during the pressure increase in the chamber is avoided.

Besides the specular beam, by using a 2D detector, also the diffuse scattering signal was simultaneously captured in real time. Observing the temporal changes in the diffuse scattering gave instantaneously feedback of the successful growth of a multilayer structure.

In the future, the optimized *in situ* XRR method presented in this work can be applied to gain insight in the film formation of almost any coating material, since it is independent of the crystalline structure.

Moreover, due to the high intensity of the reflected beam, *in situ* XRR measurements can also be performed using conventional X-ray laboratory sources. This makes this technique very interesting as a versatile tool for material science in general.

Synchrotron radiation gives access to faster processes and simultaneously allows the monitoring of the diffuse scattering signal. The diffuse scattering gives instant feedback of the correlated roughness during the formation of the multilayer. Due to the high sensitivity to the microstructural changes of this method, it can be also applied to more complex systems, e.g. aperiodic multilayer systems.

Considering the experimental setup, a larger sample-detector distance might be used for a better angular resolution (angular range covered by one pixel). This allows the better extraction of the position of the Yoneda wing, which is directly related to the electron density changes.

The here presented results concerning the material system V-C can be transferred to other monocarbides of transition metals e.g. Ti-C due to their structural similarity.

Hardness, adhesion, and friction are important properties for applications. Those proper-

ties should be investigated in the future, clarifying if they are enhanced for the multilayer structure compared to single layers.

The very simple growth procedure for achieving a multilayer structure should be applicable to other material systems, provided that the involved elements differ significantly in their mass and phase separation can occur.

Bibliography

- [Aba08a] ABADIAS, G: Stress and preferred orientation in nitride-based PVD coatings. *Surface and Coatings Technology* (2008), Bd. 202(11): S. 2223–2235
(Zitiert auf Seiten 19 and 20)
- [Aba08b] ABADIAS, G.; PAILLOUX, F. und DUB, S.N.: Epitaxial growth and mechanical properties of (001) ZrN/W nanolaminates. *Surface and Coatings Technology* (2008), Bd. 202(15): S. 3683 – 3687
(Zitiert auf Seiten 2 and 23)
- [Aba09] ABADIAS, G.; KOUTSOKERAS, L.E.; GUERIN, Ph. und PATSALAS, P.: Stress evolution in magnetron sputtered Ti-Zr-N and Ti-Ta-N films studied by in situ wafer curvature: Role of energetic particles. *Thin Solid Films* (2009), Bd. 518(5): S. 1532 – 1537
(Zitiert auf Seiten 94 and 100)
- [Adj95] ADJAOTTOR, A.A.; MELETIS, E.I.; LOGOTHETIDIS, S.; ALEXANDROU, I. und KOKKOU, S.: Effect of substrate bias on sputter-deposited TiC_x , TiN_y and TiC_xN_y thin films. *Surface and Coatings Technology* (1995), Bd. 76-77, Part 1(0): S. 142 – 148
(Zitiert auf Seite 10)
- [Aek08] AEKEN, K Van; MAHIEU, S und DEPLA, D: The metal flux from a rotating cylindrical magnetron: a Monte Carlo simulation. *Journal of Physics D: Applied Physics* (2008), Bd. 41(20): S. 205307
(Zitiert auf Seiten 2, 11, 13, and 60)
- [Alv14] ALVAREZ, Rafael; GARCIA-MARTIN, Jose M; LOPEZ-SANTOS, Maria C; RICO, Victor; FERRER, Francisco J; COTRINO, Jose; GONZALEZ-ELIPE, Agustin R und PALMERO, Alberto: On the Deposition Rates of Magnetron Sputtered Thin Films at Oblique Angles. *Plasma Processes and Polymers* (2014)
(Zitiert auf Seite 13)
- [AN11] ALS-NIELSEN, Jens und MCMORROW, Des: *Elements of modern X-ray physics*, Wiley, Oxford, 2. ed. Aufl. (2011), previous ed.: 2001. - Formerly CIP Uk
(Zitiert auf Seiten 25, 46, and 134)
- [And88] ANDERSEN, Hans Henrik: Sputtering from atomic-collision cascades. *Nuclear Instruments and Methods in Physics Research Section B: Beam Interactions with Materials and Atoms* (1988), Bd. 33: S. 466 – 473
(Zitiert auf Seite 98)

- [Bar98] BARNA, PB und ADAMIK, M: Fundamental structure forming phenomena of polycrystalline films and the structure zone models. *Thin Solid Films* (1998), Bd. 317(1): S. 27–33
(Zitiert auf Seiten 2, 16, and 17)
- [Bie80] BIERSACK, J.P. und HAGGMARK, L.G.: A Monte Carlo computer program for the transport of energetic ions in amorphous targets. *Nuclear Instruments and Methods* (1980), Bd. 174: S. 257 – 269
(Zitiert auf Seiten 57 and 58)
- [Bra75] BRADSHAW, AM und KRAUSE, U: APS-und XPS-Untersuchungen an Vanadium, Vanadiumkarbid und Graphit. *Berichte der Bunsengesellschaft für physikalische Chemie* (1975), Bd. 79(11): S. 1095–1101
(Zitiert auf Seite 95)
- [Bri03] BRIGGS, David [Hrsg.] (Herausgeber): *Surface analysis by Auger and X-ray photoelectron spectroscopy*, SurfaceSpectra, Manchester (2003)
(Zitiert auf Seite 35)
- [Bul96] BULL, SJ und JONES, AM: Multilayer coatings for improved performance. *Surface and Coatings Technology* (1996), Bd. 78(1): S. 173–184
(Zitiert auf Seiten 23 and 142)
- [Bun01] BUNSHAH, Rointan F. (Herausgeber): *Handbook of hard coatings : deposition technologies, properties and applications*, Materials science and processing technology series, Noyes Publications [u.a.], Park Ridge, NJ (2001)
(Zitiert auf Seiten 7 and 19)
- [Chi97] CHIARELLO, R.P.; YOU, H.; KIM, H.K.; ROBERTS, T.; KEMPWIRTH, R.T.; MILLER, D.; GRAY, K.E.; VANDERVOORT, K.G.; TRIVEDI, N.; PHILLPOT, S.R.; ZHANG, Q.J.; WILLIAMS, S. und KETTERSON, J.B.: X-ray reflectivity study on gold films during sputter deposition. *Surface Science* (1997), Bd. 380: S. 245 – 257
(Zitiert auf Seiten 1 and 67)
- [Cho99] CHOI, Jeong-Gil: The surface properties of vanadium compounds by X-ray photoelectron spectroscopy. *Applied surface science* (1999), Bd. 148(1): S. 64–72
(Zitiert auf Seite 95)
- [Cze91] CZEKAJ, D; GORANCHEV, B; HOLLMANN, EK; VOLPYAS, VA und ZAYTSEV, AG: Incident ion energy spectrum and target sputtering rate in dc planar magnetron. *Vacuum* (1991), Bd. 42(1): S. 43–45
(Zitiert auf Seite 58)
- [Dep08] DEPLA, Diederik und MAHIEU, Stijn (Herausgeber): *Reactive Sputter Deposition*, Springer Series in Materials Science, Springer Berlin Heidelberg (2008)
(Zitiert auf Seiten 7 and 58)

- [Die05] DIEKER, Henning und WUTTIG, Matthias: Influence of deposition parameters on the properties of sputtered $\text{Ge}_2\text{Sb}_2\text{Te}_5$ films. *Thin Solid Films* (2005), Bd. 478(1): S. 248–251
(Zitiert auf Seiten 13, 79, and 87)
- [Die14] Diener automation GmbH & Co. KG, last accessed: October 2014 (2014), URL <http://www.diener-automation.de/>
(Zitiert auf Seite 42)
- [Ekl07] EKLUND, P.; BECKERS, M.; FRODELIUS, J.; HOGBERG, H. und HULTMAN, L.: Magnetron sputtering of Ti_3SiC_2 thin films from a compound target. *Journal of Vacuum Science & Technology A: Vacuum, Surfaces, and Films* (2007), Bd. 25(5): S. 1381–1388
(Zitiert auf Seiten 2 and 100)
- [EM10a] EL MEL, AA; ANGLERAUD, B; GAUTRON, E; GRANIER, A und TESSIER, PY: Microstructure and composition of TiC/aC: H nanocomposite thin films deposited by a hybrid IPVD/PECVD process. *Surface and Coatings Technology* (2010), Bd. 204(12): S. 1880–1883
(Zitiert auf Seiten 2, 21, and 22)
- [EM10b] EL MEL, AA; GAUTRON, E; CHOI, CH; ANGLERAUD, B; GRANIER, A und TESSIER, PY: Titanium carbide/carbon composite nanofibers prepared by a plasma process. *Nanotechnology* (2010), Bd. 21(43): S. 435603
(Zitiert auf Seite 95)
- [Fai05] FAIRLEY, Neal und CARRICK, Alan: *The Casa cookbook*, Bd. 1: Recipes for XPS data processing, Acolyte Science, Knutsford (2005)
(Zitiert auf Seiten 35 and 95)
- [Fil10] FILLON, A.; ABADIAS, G.; MICHEL, A. und JAOUEN, C.: Stress and microstructure evolution during growth of magnetron-sputtered low-mobility metal films: Influence of the nucleation conditions. *Thin Solid Films* (2010), Bd. 519(5): S. 1655 – 1661
(Zitiert auf Seite 58)
- [Gem12] GEMMLER, Jochen: *Simulation von Wachstumsprozessen während des Magnetron-Sputterns*, Bachelor Thesis (2012)
(Zitiert auf Seite 115)
- [GES14] GESTIS-Stoffdatenbank, last accessed: October 2014 (2014), URL <http://www.dguv.de/>
(Zitiert auf Seiten 20 and 169)
- [Häg31] HÄGG, G: Gesetzmässigkeiten im kristallbau bei hydriden, boriden, carbiden und nitriden der übergangselemente. *Z. Phys. Chem. B* (1931), Bd. 12: S. 33–56
(Zitiert auf Seite 20)

- [He11] HE, Yuping und ZHAO, Yiping: Advanced multi-component nanostructures designed by dynamic shadowing growth. *Nanoscale* (2011), Bd. 3(6): S. 2361–2375
(Zitiert auf Seite 143)
- [Hol90] HOLLECK, HW: Advanced concepts of PVD hard coatings. *Vacuum* (1990), Bd. 41(7): S. 2220–2222
(Zitiert auf Seiten 2 and 23)
- [Iba06] IBACH, Harald: *Physics of surfaces and interfaces*, Springer, Berlin (2006)
(Zitiert auf Seite 15)
- [ICS14] Inorganic Crystal Structure Database, last accessed: October 2014 (2014), URL <http://www.fiz-karlsruhe.de/icsd.html>
(Zitiert auf Seiten 20 and 169)
- [Iri03] IRIFUNE, Tetsuo; KURIO, Ayako; SAKAMOTO, Shizue; INOUE, Toru und SUMIYA, Hitoshi: Materials: Ultrahard polycrystalline diamond from graphite. *Nature* (2003), Bd. 421(6923): S. 599–600
(Zitiert auf Seite 19)
- [Jan07] JANSSENS, Ewald; GRUENE, Philipp; MEIJER, Gerard; WÖSTE, Ludger; LIEVENS, Peter und FIELICKE, André: Argon Physisorption as Structural Probe for Endohedrally Doped Silicon Clusters. *Phys. Rev. Lett.* (2007), Bd. 99: S. 063401
(Zitiert auf Seite 131)
- [Jan13] JANSSON, Ulf und LEWIN, Erik: Sputter deposition of transition-metal carbide films- A critical review from a chemical perspective. *Thin Solid Films* (2013), Bd. 536: S. 1–24
(Zitiert auf Seiten 19, 20, 21, 22, and 161)
- [Kag04] KAGANER, Vladimir M.; BRAUN, Wolfgang; JENICHEN, Bernd und PLOOG, Klaus H.: Two stages of post-growth recovery in molecular beam epitaxy: a surface X-ray diffraction study. *Surface Science* (2004), Bd. 560: S. 88 – 102
(Zitiert auf Seite 67)
- [Kar04] KARABACAK, T; WANG, G-C und LU, T-M: Physical self-assembly and the nucleation of three-dimensional nanostructures by oblique angle deposition. *Journal of Vacuum Science & Technology A* (2004), Bd. 22(4): S. 1778–1784
(Zitiert auf Seite 143)
- [Kie31] KIESSIG, Heinz: Interferenz von Röntgenstrahlen an dünnen Schichten. *Annalen der Physik* (1931), Bd. 402(7): S. 769–788
(Zitiert auf Seite 30)
- [Kle10] KLEVER, C; SEEMANN, K; STUEBER, M; ULRICH, S; BRUNKEN, H; LUDWIG, A und LEISTE, H: Epitaxially stabilized TiN/(Ti,Fe,Co)N multilayer thin films

- in (pseudo-)fcc crystal structure by sequential magnetron sputter deposition. *Journal of Physics D: Applied Physics* (2010), Bd. 43(39): S. 395406
(Zitiert auf Seiten [2](#) and [23](#))
- [Kra12] KRAUSE, Bärbel; DARMA, Susan; KAUFHOLZ, Marthe; GRÄFE, Hans-Hellmuth; ULRICH, Sven; MANTILLA, Miguel; WEIGEL, Ralf; REMBOLD, Steffen und BAUMBACH, Tilo: Modular deposition chamber for *in situ* X-ray experiments during RF and DC magnetron sputtering. *Journal of Synchrotron Radiation* (2012), Bd. 19: S. 216–222
(Zitiert auf Seite [41](#))
- [Lai11] LAIDANI, N.; BARTALI, R.; MICHELI, V.; GOTTARDI, G. und CHEYSSAC, P.: Study of growth processes and mechanical properties of nanoscale multilayered C/C films. *Surface and Coatings Technology* (2011), Bd. 206(4): S. 654 – 666
(Zitiert auf Seiten [23](#) and [143](#))
- [Lee08] LEE, Hsin-Yi; HUANG, Tzu-Wen; LEE, Chih-Hao und HSIEH, Yung-Wei: Surface morphology of sputtered Ta₂O₅ thin films on Si substrates from X-ray reflectivity at a fixed angle. *Journal of Applied Crystallography* (2008), Bd. 41(2): S. 356–362
(Zitiert auf Seiten [1](#) and [67](#))
- [Lek87] LEKNER, John: *Theory of reflection of electromagnetic and particle waves*, Developments in electromagnetic theory and applications ; 3, Nijhoff, Dordrecht [u.a.] (1987)
(Zitiert auf Seite [25](#))
- [Li11] LI, Fengji; ZHANG, Sam; KONG, Junhua; ZHANG, Yujuan und ZHANG, Wali: Multilayer DLC coatings via alternating bias during magnetron sputtering. *Thin Solid Films* (2011), Bd. 519(15): S. 4910 – 4916
(Zitiert auf Seiten [23](#) and [143](#))
- [Lia04] LIAO, M. Y.; GOTOH, Y.; TSUJI, H. und ISHIKAWA, J.: Compound-target sputtering for niobium carbide thin-film deposition. *Journal of Vacuum Science & Technology B: Microelectronics and Nanometer Structures* (2004), Bd. 22(5): S. L24–L27
(Zitiert auf Seite [10](#))
- [Lia05] LIAO, M. Y.; GOTOH, Y.; TSUJI, H. und ISHIKAWA, J.: Deposition of vanadium carbide thin films using compound target sputtering and their field emission. *Journal of Vacuum Science & Technology A: Vacuum, Surfaces, and Films* (2005), Bd. 23(5): S. 1379–1383
(Zitiert auf Seiten [2](#), [10](#), [20](#), [95](#), and [100](#))
- [Lip05] LIPATNIKOV, Vladimir Nikolaevich: Phase equilibria, phases and compounds in the VC system. *Russian chemical reviews* (2005), Bd. 74(8): S. 697–723

- (Zitiert auf Seiten 20 and 21)
- [Lou94] LOUIS, E.; VOORMA, H.-J.; KOSTER, N.B.; SHMAENOK, L.; BIJKERK, F.; SCHLATMANN, R.; VERHOEVEN, J.; PLATONOV, Yu.Ya.; VAN DORSSEN, G.E. und PADMORE, H.A.: Enhancement of reflectivity of multilayer mirrors for soft x-ray projection lithography by temperature optimization and ion bombardment. *Microelectronic Engineering* (1994), Bd. 23: S. 215 – 218
(Zitiert auf Seiten 1 and 67)
- [Lüt10] LÜTH, Hans: *Solid Surfaces, Interfaces and Thin Films*, Graduate Texts in Physics, Springer, Berlin (2010)
(Zitiert auf Seite 15)
- [Mah06a] MAHIEU, S.; BUYLE, G.; DEPLA, D.; HEIRWEGH, S.; GHEKIERE, P. und GRYSE, R. De: Monte Carlo simulation of the transport of atoms in DC magnetron sputtering. *Nuclear Instruments and Methods in Physics Research Section B: Beam Interactions with Materials and Atoms* (2006), Bd. 243(2): S. 313 – 319
(Zitiert auf Seiten 11, 57, and 58)
- [Mah06b] MAHIEU, Stijn; GHEKIERE, Pieter; DEPLA, Diederik und DE GRYSE, Roger: Biaxial alignment in sputter deposited thin films. *Thin Solid Films* (2006), Bd. 515(4): S. 1229–1249
(Zitiert auf Seite 2)
- [Mah09] MAHIEU, Stijn und DEPLA, Diederik: Reactive sputter deposition of TiN layers: modelling the growth by characterization of particle fluxes towards the substrate. *Journal of Physics D: Applied Physics* (2009), Bd. 42(5): S. 053002
(Zitiert auf Seiten 108 and 113)
- [Mat98] MATTOX, Donald M.: *Handbook of physical vapor deposition (PVD) processing: film formation, adhesion, surface preparation and contamination control*, Noyes Publications, Westwood, NJ (1998)
(Zitiert auf Seiten 7 and 15)
- [May06] MAYRHOFER, Paul H.; MITTERER, Christian; HULTMAN, Lars und CLEMENS, Helmut: Microstructural design of hard coatings. *Progress in Materials Science* (2006), Bd. 51(8): S. 1032 – 1114
(Zitiert auf Seite 67)
- [MM09] MARTINEZ-MARTINEZ, D; LOPEZ-CARTES, C; FERNÁNDEZ, A und SÁNCHEZ-LÓPEZ, JC: Influence of the microstructure on the mechanical and tribological behavior of TiC/aC nanocomposite coatings. *Thin Solid Films* (2009), Bd. 517(5): S. 1662–1671
(Zitiert auf Seiten 21, 22, and 101)

- [Moe88] MOELLER, W.; ECKSTEIN, W. und BIRSACK, J.P.: Tridyn-binary collision simulation of atomic collisions and dynamic composition changes in solids. *Computer Physics Communications* (1988), Bd. 51(3): S. 355 – 368
(Zitiert auf Seiten 10 and 58)
- [Mou92] MOULDER, John F. und CHASTAIN, Jill (Herausgeber): *Handbook of x-ray photoelectron spectroscopy : a reference book of standard spectra for identification and interpretation of XPS data*, Perkin-Elmer, Physical Electronics Div., Eden Prairie, Minn. (1992)
(Zitiert auf Seiten 35, 36, 95, 98, 99, and 164)
- [Mra13] MRAZ, Stanislav; EMMERLICH, Jens; WEYAND, Felix und SCHNEIDER, Jochen M.: Angle-resolved evolution of the composition of CrAC thin films deposited by sputtering of a compound target. *Journal of Physics D: Applied Physics* (2013), Bd. 46(13): S. 135501
(Zitiert auf Seiten 2, 10, 57, 59, 99, and 100)
- [Mur87] MURRAY, Joanne L.: Phase diagrams of binary titanium alloys. *ASM International, 1987*, (1987): S. 354
(Zitiert auf Seiten 21 and 161)
- [Ned11] NEDFORS, Nils; TENGSTRAND, Olof; LEWIN, Erik; FURLAN, Andrej; EKLUND, Per; HULTMAN, Lars und JANSSON, Ulf: Structural, mechanical and electrical-contact properties of nanocrystalline-NbC/amorphous-C coatings deposited by magnetron sputtering. *Surface and Coatings Technology* (2011), Bd. 206: S. 354 – 359
(Zitiert auf Seite 21)
- [Nei08] NEIDHARDT, Jorg; MRAZ, Stanislav; SCHNEIDER, Jochen M.; STRUB, Erik; BOHNE, Wolfgang; LIEDKE, Bartosz; MOLLER, Wolfhard und MITTERER, Christian: Experiment and simulation of the compositional evolution of Ti-B thin films deposited by sputtering of a compound target. *Journal of Applied Physics* (2008), Bd. 104(6): S. 063304
(Zitiert auf Seiten 2, 10, 57, 59, 99, and 100)
- [Nev80] NEVOT, L. und CROCE, P.: Caractérisation des surfaces par réflexion rasante de rayons X. Application à l'étude du polissage de quelques verres silicates. *Rev. Phys. Appl. (Paris)* (1980), Bd. 15: S. 761–779
(Zitiert auf Seite 31)
- [Ols79] OLSON, R. R.; KING, M. E. und WEHNER, G. K.: Mass effects on angular distribution of sputtered atoms. *Journal of Applied Physics* (1979), Bd. 50(5): S. 3677–3683
(Zitiert auf Seiten 98 and 99)
- [Par54] PARRATT, L. G.: Surface Studies of Solids by Total Reflection of X-Rays. *Phys. Rev.* (1954), Bd. 95: S. 359–369

- (Zitiert auf Seiten 28 and 71)
- [Pau02] PAUL, A.; LIM, Jongmin; CHOI, Kyunsuk und LEE, Chongmu: Effects of deposition parameters on the properties of chromium carbide coatings deposited onto steel by sputtering. *Materials Science and Engineering: A* (2002), Bd. 332: S. 123–128
(Zitiert auf Seite 87)
- [Ped94] PEDERSEN, J. S. und HAMLEY, I. W.: Analysis of neutron and X-ray reflectivity data. II. Constrained least-squares methods. *Journal of Applied Crystallography* (1994), Bd. 27(1): S. 36–49
(Zitiert auf Seite 75)
- [Pet03] PETROV, I; BARNA, PB; HULTMAN, Lars und GREENE, JE: Microstructural evolution during film growth. *Journal of Vacuum Science & Technology A* (2003), Bd. 21(5): S. S117–S128
(Zitiert auf Seiten 2, 15, 16, 17, and 161)
- [Pev05] PEVERINI, Luca; ZIEGLER, Eric; BIGAULT, Thierry und KOZHEVNIKOV, Igor: Roughness conformity during tungsten film growth: An *in situ* synchrotron x-ray scattering study. *Phys. Rev. B* (2005), Bd. 72: S. 045445
(Zitiert auf Seiten 1 and 67)
- [Pfl84] PFLÜGER, J; FINK, J; WEBER, W; BOHNEN, KP und CRECELIUS, G: Dielectric properties of TiC_x , TiN_x , VC_x , and VN_x from 1.5 to 40 eV determined by electron-energy-loss spectroscopy. *Physical Review B* (1984), Bd. 30(3): S. 1155
(Zitiert auf Seiten 2 and 21)
- [Pie96] PIERSON, Hugh O.: *Handbook of refractory carbides and nitrides : properties, characteristics, processing and applications*, Materials science and process technology series : Electronic materials and process technology, Noyes Publ., Westwood, NJ (1996)
(Zitiert auf Seiten 20 and 169)
- [Pie04] PIETSCH, Ullrich; HOLY, Vaclav und BAUMBACH, Tilo: *High-resolution X-ray scattering: from thin films to lateral nanostructures*, Springer, 2 Aufl. (2004)
(Zitiert auf Seiten 25, 32, 49, 75, 134, and 162)
- [Rei09] REITHMAIER, Johann Peter (Herausgeber): *Nanostructured materials for advanced technological applications*, NATO Science for Peace and Security Series - B : Physics and Biophysics, Springer, Dordrecht (2009)
(Zitiert auf Seite 19)
- [Ren09] RENAUD, Gilles; LAZZARI, Remi und LEROY, Frederic: Probing surface and interface morphology with Grazing Incidence Small Angle X-Ray Scattering. *Surface Science Reports* (2009), Bd. 64(8): S. 255 – 380
(Zitiert auf Seiten 1 and 25)

- [Rep92] REPOUX, M: Comparison of background removal methods for XPS. *Surface and interface analysis* (1992), Bd. 18(7): S. 567–570
(Zitiert auf Seite 38)
- [Rob79] ROBINSON, R. S.: Energetic binary collisions in rare gas plasmas. *Journal of Vacuum Science & Technology* (1979), Bd. 16(2): S. 185–188
(Zitiert auf Seite 12)
- [Sam12] SAMUELSSON, Mattias; SARAΚINOS, Kostas; HÖGBERG, Hans; LEWIN, Erik; JANSSON, Ulf; WÄLIVAARA, Bengt; LJUNGRANTZ, Henrik und HELMERSSON, Ulf: Growth of Ti-C nanocomposite films by reactive high power impulse magnetron sputtering under industrial conditions. *Surface and Coatings Technology* (2012), Bd. 206(8-9): S. 2396 – 2402
(Zitiert auf Seiten 22, 100, and 101)
- [Sch07] SCHATT, Werner (Herausgeber): *Pulvermetallurgie: Technologien und Werkstoffe*, VDI, Springer, Berlin, 2., bearb. und erw. Aufl. Aufl. (2007)
(Zitiert auf Seite 19)
- [Sea90] SEAH, M. P. und SMITH, G. C.: Quantitative AES and XPS: Determination of the electron spectrometer transmission function and the detector sensitivity energy dependencies for the production of true electron emission spectra in AES and XPS. *Surface and Interface Analysis* (1990), Bd. 15(12): S. 751–766
(Zitiert auf Seiten 54, 55, and 163)
- [Sha10] SHAHA, K.P.; PEI, Y.T.; MARTINEZ-MARTINEZ, D. und HOSSON, J.Th.M. De: Influence of hardness and roughness on the tribological performance of TiC/a-C nanocomposite coatings. *Surface and Coatings Technology* (2010), Bd. 205(7): S. 2624 – 2632
(Zitiert auf Seite 87)
- [Sin88] SINHA, S. K.; SIROTA, E. B.; GAROFF, S. und STANLEY, H. B.: X-ray and neutron scattering from rough surfaces. *Phys. Rev. B* (1988), Bd. 38: S. 2297–2311
(Zitiert auf Seiten 31 and 32)
- [Sri14] SRIM: www.srim.org, last accessed: October 2014 (2014), URL <http://www.srim.org/>
(Zitiert auf Seite 10)
- [Sti04] STIERLE, A.; STEINHÄUSER, A.; RÜHM, A.; RENNER, F. U.; WEIGEL, R.; KASPER, N. und DOSCH, H.: Dedicated Max-Planck beamline for the in situ investigation of interfaces and thin films. *Review of Scientific Instruments* (2004), Bd. 75(12): S. 5302–5307
(Zitiert auf Seite 46)

- [Stu02] STUEBER, M.; LEISTE, H.; ULRICH, S.; HOLLECK, H. und SCHILD, D.: Microstructure and properties of low friction TiC-C nanocomposite coatings deposited by magnetron sputtering. *Surface and Coatings Technology* (2002), Bd. 150: S. 218 – 226
(Zitiert auf Seiten 2, 21, and 22)
- [Stu09] STUEBER, M.; HOLLECK, H.; LEISTE, H.; SEEMANN, K.; ULRICH, S. und ZIEBERT, C.: Concepts for the design of advanced nanoscale PVD multilayer protective thin films. *Journal of Alloys and Compounds* (2009), Bd. 483: S. 321 – 333, 14th International Symposium on Metastable and Nano-Materials (ISMANAM-2007)
(Zitiert auf Seiten 2, 23, and 129)
- [Sun10] SUN, Zhimei; AHUJA, Rajeev und LOWTHER, JE: Mechanical properties of vanadium carbide and a ternary vanadium tungsten carbide. *Solid State Communications* (2010), Bd. 150(15): S. 697–700
(Zitiert auf Seite 21)
- [Teg09] TEGHIL, R; DE BONIS, A; GALASSO, A; VILLANI, P; SANTAGATA, A; FERRO, D und BARINOV, SM: Nanostructured thin films obtained by ultra-short pulse laser deposition of vanadium carbide. *Applied Surface Science* (2009), Bd. 255(10): S. 5220–5223
(Zitiert auf Seiten 20 and 95)
- [Tho77] THORNTON, John A: High rate thick film growth. *Annual review of materials science* (1977), Bd. 7(1): S. 239–260
(Zitiert auf Seite 87)
- [Tho00] THOMPSON, C. V.: Structure Evolution during Processing of Polycrystalline Films. *Annual Review of Materials Science* (2000), Bd. 30(1): S. 159–190
(Zitiert auf Seite 15)
- [Tol99] TOLAN, Metin: *X-ray scattering from soft-matter thin films: materials science and basic research*, Springer tracts in modern physics ; 148, Springer, Berlin (1999)
(Zitiert auf Seiten 25 and 31)
- [Tot71] TOTH, Louis E.: *Transition metal carbides and nitrides*, Refractory materials, Acad. Pr., New York (1971)
(Zitiert auf Seiten 19, 20, and 169)
- [Tou93] TOUGAARD, S. und JANSSON, C.: Comparison of validity and consistency of methods for quantitative XPS peak analysis. *Surface and Interface Analysis* (1993), Bd. 20(13): S. 1013–1046
(Zitiert auf Seite 38)
- [Ulr04] ULRICH, S.; ZIEBERT, C.; STUBER, M.; NOLD, E.; HOLLECK, H.; GOKEN, M.; SCHWEITZER, E. und SCHLOSSMACHER, P.: Correlation between con-

- stitution, properties and machining performance of TiN/ZrN multilayers. *Surface and Coatings Technology* (2004), Bd. 188-189(0): S. 331 – 337
(Zitiert auf Seiten [2](#), [23](#), and [46](#))
- [Wai78] WAITS, Robert K: Planar magnetron sputtering. *Journal of Vacuum Science and Technology* (1978), Bd. 15(2): S. 179–187
(Zitiert auf Seiten [2](#), [10](#), [79](#), [83](#), and [87](#))
- [Wat03] WATTS, John F. und WOLSTENHOLME, John: *An introduction to surface analysis by XPS and AES*, Wiley, New York (2003)
(Zitiert auf Seite [35](#))
- [Wue11] WUESTEFELD, Ch.; RAFAJA, D.; DOPITA, M.; MOTYLENKO, M.; BAEHTZ, C.; MICHOTTE, C. und KATHREIN, M.: *Surface and Coatings Technology* (2011), Bd. 206(7): S. 1727–1734
(Zitiert auf Seite [67](#))
- [Yam95] YAMAMURA, Y. und ISHIDA, M.: Monte Carlo simulation of the thermalization of sputtered atoms and reflected atoms in the magnetron sputtering discharge. *Journal of Vacuum Science & Technology A* (1995), Bd. 13(1): S. 101–112
(Zitiert auf Seiten [58](#) and [99](#))
- [Yoo96] YOON, Jong-Hwan und LEE, Czung-Ho: Stability of undoped hydrogenated amorphous silicon multilayer film grown with alternating substrate temperature. *Applied Physics Letters* (1996), Bd. 69(9): S. 1250–1252
(Zitiert auf Seiten [23](#) and [142](#))
- [Yu13] YU, Shun; SANTORO, Gonzalo; SARKAR, Kuhu; DICKE, Benjamin; WESSELS, Philipp; BOMMEL, Sebastian; DÖHRMANN, Ralph; PERLICH, Jan; KUHLMANN, Marion; METWALLI, Ezzeldin; RISCH, Johannes F. H.; SCHWARTZKOPF, Matthias; DRESCHER, Markus; MÜLLER-BUSCHBAUM, Peter und ROTH, Stephan V.: Formation of Al Nanostructures on Alq₃: An in Situ Grazing Incidence Small Angle X-ray Scattering Study during Radio Frequency Sputter Deposition. *The Journal of Physical Chemistry Letters* (2013), Bd. 4(18): S. 3170–3175
(Zitiert auf Seiten [1](#) and [25](#))
- [Zha97] ZHANG, Zhenyu und LAGALLY, Max G: Atomistic processes in the early stages of thin-film growth. *Science* (1997), Bd. 276(5311): S. 377–383
(Zitiert auf Seiten [113](#), [114](#), and [119](#))
- [Zha05] ZHANG, Sam; BUI, Xuan Lam; JIANG, Jiaren und LI, Xiaomin: Microstructure and tribological properties of magnetron sputtered nc-TiC/a-C nanocomposite. *Surface and Coatings Technology* (2005), Bd. 198(1-3): S. 206 – 211
(Zitiert auf Seite [101](#))

- [Zha13] ZHANG, Xiaojuan; WANG, Bo; ZHAN, Zhaolin und HUANG, Feng: Microstructure, chemical states, and mechanical properties of VCCo coatings prepared by non-reactive magnetron sputtering. *Thin Solid Films* (2013), Bd. 540(0): S. 135 – 141
(Zitiert auf Seiten [2](#) and [100](#))
- [Zha14] ZHANG, Kan; WEN, M.; CHENG, G.; LI, X.; MENG, Q.N.; LIAN, J.S. und ZHENG, W.T.: Reactive magnetron sputtering deposition and characterization of niobium carbide films. *Vacuum* (2014), Bd. 99(0): S. 233 – 241
(Zitiert auf Seiten [100](#) and [101](#))
- [Zie85] ZIEGLER, James F und BIRSACK, Jochen P: *The stopping and range of ions in matter*, Springer (1985)
(Zitiert auf Seiten [57](#) and [58](#))

List of Figures

1.1	Schematic of a sputter chamber during deposition. The main components are shown.	8
1.2	The Ar ion bombard the composite target leading to a sputtering of target atoms. For more details s. text.	10
1.3	Image of the V-C target. The racetrack is indicated by circles.	12
1.4	The sputtered particles drift to the substrate and diffuse. For more details s. text.	14
1.5	Scheme, showing the several stages of microstructural evolution. Adapted from [Pet03].	16
2.1	(a) Schematic binary phase diagram of TM-C (adapted from [Mur87],[Jan13]),(b) Rocksalt structure. The non-metal sublattice sites are only randomly occupied.	21
2.2	Schematic of the evolution of the microstructure depending on the C content, adapted from [Jan13].	22
3.1	Scheme of the X-ray reflectivity geometry, showing the notation used in the text.	28
3.2	Simulated XRR curve of a 20 nm thick V-C film on Silicon substrate. . .	29
3.3	(a) Scheme of a rough film. Here the fluctuations around the mean height can be described by a Gaussian distribution. (b) Development of the potential V for the unperturbed (left) and perturbed (right) case. The potential V is proportional to the mean electron density ρ . z is oriented normal to the surface of the interface.	31
3.4	Scattering geometry of XRR measurements. Interfacial roughness gives rise to intensity in the non-specular direction.	33
3.5	(a) Schematic of multilayer structures: (1) ideal multilayer, (2) with perfect correlated roughness, and (3) with uncorrelated roughness. (b) Scheme of a diffuse XRR map indicating the characteristic features in case of measuring a multilayer system with correlated roughness. The gray dotted line indicates More details s. text.	33
4.1	(a) Scheme of the emission of a photoelectron due to the irradiation of X-rays. (b) Scheme of an XPS chamber showing X-ray tube, sample and electron energy analyzer	36

4.2	XPS spectrum of a VC thin film. The photoemission peaks of V and the Auger line of V (V_{LMM}) are highlighted.	37
4.3	(a) V2p peak with the three different backgrounds. (b) V2p after background correction.	38
5.1	(a) The sputtering chamber system installed at the UHV Analysis Laboratory at ANKA highlighting important parts. (b) Scheme of configuration of the sputter chamber used in this work.	42
5.2	Time-dependent development of DC Power (red) and pressure in the chamber (blue) logged during the growth of (a) <i>LP-a(3.5)</i> , (b) <i>P-step</i> , during the multilayer growth (c) by interrupted deposition (<i>LP-a(2.5)</i>) and (d) by tuning the gas flow (<i>gas-ML</i>). Please note, that for <i>LP-a(2.5)</i> the different periods were put after each other. The interruption is indicated by gray boxes.	44
5.3	Map of part of the ANKA hall. The synchrotron experiments were performed at the MPI Beamline (highlighted in blue). Complementary measurements were performed at the UHV Analysis Lab (highlighted in red) and the DiffLab (highlighted in green).	46
5.4	Schematic beamline layout of the Max-Planck-Beamline located at ANKA.	47
5.5	The sputtering chamber setup at the MPI Beamline in the experimental hutch. a) Overview showing the chamber mounted on the 4+2 circle diffractometer, the control unit and the PC for the automatically control of the deposition process. b) Closer look at the 4+2 circle diffractometer. The beryllium windows are shown without protection shielding. The three detectors (PILATUS, APD, and NaI scintillator) are fixed on the detector arm of the diffractometer.	48
5.6	Scheme for the determination of the geometry factor showing the illumination of the sample at small incidence angles. After [Pie04].	49
5.7	(a) Scheme of the scattering geometry setup at fixed angular position. (b) Schematic drawing of the different angle positions at the specular beam used for the conversion of pixel in angular range.	50
5.8	(a) Pilatus images before (left) and during deposition after 150 s (right). The images are already imported into MATLAB. The integration range for the specular beam is indicated with the red box, the region for the diffuse background subtraction is shown in black. Main features of the reflectivity are highlighted. (b) Integrated intensity around the specular beam (red lines) and the diffuse background (black lines), corresponding to the above-presented PILATUS images. Additionally the integrated intensity after background subtraction (green lines) is presented.	51

- 5.9 (a) Scheme of the UHV Cluster at the UHV Analysis Laboratory at ANKA. Highlighted with color: the sputtering chamber (green), the XPS Chamber (blue), docking station (red), loadlock (yellow) and used part of the transfer system (orange). Courtesy of CreaTec Fischer & Co. GmbH except image of AFM - Courtesy of Omicron Nano Technology GmbH. (b) The X-ray Photoemission Spectroscopy Chamber 54
- 5.10 XPS spectrum of Ag reference sample (black) and reference curve (gray) taken from [Sea90]. 55
- 6.1 Emission Flux of C and V atoms depending on the emission angle from (a) SRIM simulation (Note the logarithmic scale) and (b) TRIDYN simulation. 0° correspond sputtering along the normal direction of the target 60
- 6.2 (a) Scheme of sputtering chamber used for the SIMTRA simulations. (b) Race track approximated by Gaussian function. $x=0$ corresponds to the center of the target. 61
- 6.3 (a) Scheme of the sputter process, showing the maximum and minimum emission angle β_{max} and β_{min} . (b) Emission Flux of C and V atoms depending on the emission angle from TRIDYN simulation (s. Chapter 9). The angular range given by β_{max} and β_{min} is indicated. 62
- 7.1 Measurements of two *in situ* XRR curves of VC_{1-x} on Si(100) for the first 400 seconds of deposition. The time axis corresponds to both curves. The gray boxes indicate time intervals of 100s. At $t=0$ s (red line) the plasma was ignited. (a): *Scanning* measurement. (b) *Stationary* measurement at the fixed angular position $\alpha_{fix} = 1.6^\circ$ (corresponding to $q_z(\alpha_{fix}) = 0.283 \text{ \AA}^{-1}$). The position of α_{fix} is denoted by an arrow in (a). 68
- 7.2 Number n of scanning points per Kiessig fringe at 10 keV X-ray energy and $\Delta\alpha = 0.005^\circ$ for different deposition rates and times. The lines correspond to fixed n values and their corresponding film thickness d . For more details s. text. 69
- 8.1 The sample is sliced into a virtual stack of layers j with height z_j . This virtual stack is used for the calculation of the XRR curve. More details s. text. 72
- 8.2 Simulation of *stationary* XRR curves at $\alpha_{fix} = 1.6^\circ$ for a deposition time $T_D = 600$ s with constant $F_D = 0.22$ nm of (a) a perfect flat V-C thin film ($(\sigma(t) = 0 \text{ \AA})$ and $\sigma_{q_z} = 0 \text{ \AA}^{-1}$, (b) a linear increase in roughness ($\sigma(t) = 0.005 \text{ \AA/s} \cdot t$) and $\sigma_{q_z} = 0 \text{ \AA}^{-1}$, and (c) including only a finite resolution ($\sigma_{q_z} = 0.002 \text{ \AA}^{-1}$, $\sigma = 0 \text{ \AA}$). The envelopes of all curves are highlighted by red curves. For better comparison, the *in situ* curve of model (a) is presented in (b) and (c) as gray dotted curve. 74

8.3	Simulation of <i>scanning</i> XRR curves after the deposition at $T_D = t_1$ and $T_D = t_2 \gg t_1$, using the resolution elements $\sigma_{q_z} = 0 \text{ \AA}^{-1}$ (dotted lines) and $\sigma_{q_z} = 0.002 \text{ \AA}^{-1}$ (continuous lines). The upper curve is shifted for a better comparison. At $t_2 = t_1 + \Delta t$, the influence due to σ_{q_z} increases. . .	76
9.1	(a) <i>Stationary in situ</i> measurement during the growth of $P - step$. The mean intensity is marked by a red line. (b) Oscillation period T for different DC powers (black squares) and calculated F_D in nm/s from oscillation period (red circles).	80
9.2	Fitting of the growth oscillation at 75 W. The mean value of the intensity is marked by the green line.	82
9.3	(a) HRTEM cross-section image of the thin film. Regions at DC power of 50 W (b) and 200 W (c) are highlighted for better comparison.	82
9.4	DC current and DC voltage at the different DC powers.	84
9.5	Nascent angular distribution of (a) V and (b) C at the DC power of 50 W and 200 W.	85
10.1	Selected process parameters ((a) and (c)) and <i>stationary in situ</i> measurements ((c) and (d), black dotted lines) at high and low working gas pressure, respectively. The mean value of the intensity is marked by a purple line. Simulations are presented with red lines. The orange line marks the begin of steady growth conditions.	90
10.2	(a) XRR measurements (color) and the fits (black lines) of the Si substrates (using the X-ray energy of 10 keV). (b) δ -profile resulting from the fit. (c) XRR measurements (color) and the fits (black lines) of the samples after growth (using the X-ray energy of 8.05 keV (Cu- K_α)). (d) δ -profile resulting from the fit. The gray box indicates the Si substrate with its natural oxide layer.	92
10.3	Simulation input for the stationary measurements: (a) thickness $D(t)$, (b) $\delta(t)$, (c) $\sigma(t)$. The point in time, t_s , when the <i>steady growth conditions</i> are reached, is indicated by dotted lines for both samples.	93
10.4	(a) Overview scans of the samples grown at low (black) and high (red) pressure. The photo emission peaks of the detected elements are highlighted by blue boxes. (b) Detailed region scans for V2p and O1s. (c) Detailed region scan for the C1s revealing the splitting of the peak due to different chemical bonding.	96
10.5	(a) Overview scans of the V thin film. For comparison, a typical overview scan of a VC thin film is presented. The V2p photoemission peaks are indicated by orange boxes. The C1s peak position is highlighted by a blue box. The curves are shifted for a better comparison. (b) Normalized C1s peaks of the three samples. Expected peak position of C1s peaks are indicated by blue boxes [Mou92].	99

10.6	$\Theta - 2\Theta$ scans performed after deposition of the sample grown at high pressure (upper curve) and low pressure (lower curve). The curves are vertically shifted for better comparison. The main peaks are indicated by gray boxes.	101
11.1	<i>In situ</i> XRR measurements (black dotted lines) for the different pressure conditions. The pressure development is presented as blue line. At $t=0$ s the plasma was ignited (marked by a green line). In case of (a), the pressure was kept constant. (b)-(f) present the experimental data at different initial pressures, where the Ar flux was reduced after plasma ignition. <i>In situ</i> measurements which show similar characteristics are plotted in the same row.	105
11.2	(a) Dependence of F on the experimental parameters DC power and pressure. For details s. text. (b) Development of the pressure at <i>high</i> initial pressure, the calculated element-specific MFP, and its mean values $\langle \lambda(E_{sp,p}(t)) \rangle$	107
11.3	$F_{new}(p,P,t)$ for the three different pressure conditions.	108
11.4	(a) Angle-dependent XRR measurements (colored lines) for different initial pressures after growth. The best fits (always shown in black) is shifted for better comparison. (b) and (c) present highlighted regions of the XRR measurements at high and low initial pressure. (d) δ -profiles around layer I resulting from the input parameters for the fit.	109
11.5	Thickness $D(P)$, roughness $\sigma(P)$ and electron density $\rho_e(P)$ for the different interface layer, used for the fit of the experimental data.	110
11.6	TEM analysis of samples deposited at <i>high</i> initial pressure. Highlighted regions at for the <i>steady</i> growth regime are presented in the upper row, regions close to the Si substrate are shown in the lower row. (a) and (b): HRTEM cross section images. In (c) and (d), the area surrounded by a red line presents the region chosen for the diffraction analysis. The corresponding diffraction pattern is presented in (e) and (f).	110
11.7	Proposed growth models for the different initial pressures.	113
12.1	Scheme of the two-dimensional islands with an half-ellipsoid shape using $\varepsilon=0.2$ at different times. The major and minor axis of the ellipse are indicated in (b).	116
12.2	Scheme of the calculation of the density profile of the islands. (a) Slicing of the growth model into virtual slices. (b) Corresponding δ -profile.	116
12.3	Distribution of the islands for different distances $L = 60$ nm, 30 nm and 5 nm. The size of the islands decrease with increasing L . $\gamma = 0.44$ is kept constant.	120

12.4	Time-development of (a) the maximum thickness $z_{max}(t)$, (b) roughness $\sigma(t)$ and (c) surface coverage $S(t)$ for $L = 60$ nm, 30 nm and 5 nm. The moment t_{touch} , when the islands touch is indicated by black arrows.	120
12.5	Calculated <i>in situ</i> XRR measurements of the growth models at fixed deposition rate $\Delta F=0.215$ nm/s and fixed shape ($\gamma = 0.44$) considering different distances L of the islands. The arrow denotes the moment t_{touch} , when the islands touch. The curves are all shifted by a constant value for better comparison.	121
12.6	Islands with different shapes defined by $\gamma = 0.44, \gamma = 0.87, \gamma = 1, \gamma = 1.15,$ and $\gamma = 2.29$ at the same deposition time t . The distance $L = 30$ nm is kept constant.	123
12.7	Time-development of (a) the maximum thickness $z_{max}(t)$, (b) roughness $\sigma(t)$ and (c) surface coverage $S(t)$ for $\gamma = 0.44, \gamma = 1,$ and $\gamma = 2.29$ at a fixed distance $L = 30$ nm. The moment t_{touch} , when the islands touch is indicated by black arrows.	124
12.8	Calculated <i>in situ</i> XRR measurements of the growth models at fixed deposition rate $\Delta F=0.215$ nm/s and fixed distance $L = 30$ nm with different shape (defined by γ) of the islands. The curves are all shifted by a constant value for better comparison.	125
12.9	(a) $F_{new}(p,P,t)$ for the three different pressure conditions. For comparison the constant rate is indicated by black line. (b) Simulated <i>in situ</i> XRR curves with the different $F_{new}(p,t)$. $L = 30$ nm and $\varepsilon = 0.9$ are kept fixed. For comparison, the simulated <i>in situ</i> curve at a constant deposition rate $\Delta F = 0.215$ nm/s is additionally presented. t_{touch} is indicated by black arrows. The curves are shifted for better comparison.	126
13.1	<i>Stationary</i> measurements during the (a) first deposition, (b) second deposition and (c) deposition periods 5-7. The <i>in situ</i> XRR data of the first deposition is presented in (b) for better comparison. The <i>in situ</i> data of the 5 th deposition is presented in deposition period 6 and 7 for better comparison. The mean value is shown by red lines.	130
13.2	Line profiles of the intensity at different deposition times during the growth of <i>LP-a(2.5)</i>	131
13.3	<i>In situ</i> XRR maps during the (a) first deposition, (b) second deposition and (c) deposition periods 5-7. The bending of the stripes is denoted by black lines.	132
13.4	Scheme of the diffuse scattering map for a multilayer system with correlated roughness in angular space. The detector in the here used experimental setup cuts the reciprocal space (denoted by black dotted line).	133

13.5	(a) Reflectivity measurements (color) and their simulations (black lines) after the deposition periods 1,2,7, and 10. (b) Highlighted region of the XRR measurements and their simulations. The multilayer peaks are indicated by black dotted lines. The curves are shifted for better comparison.	135
13.6	(a) Experimental Data of the XRR measurements after deposition period 7 (red curve). Simulated XRR curve without layer III (black curve) does not agree well with the experimental data. Simulated XRR curve without considering the resolution. All $n - 2$ Kiessig fringes due to the total thickness are resolved. (b) δ -profile based on the simulation input. The individual layers are highlighted by color (Si substrate+SiO _x :gray, Layer 1: green, Layer 2: orange, Layer 3: white)	136
13.7	Model of the multilayer structure based on the results of the XRR analysis (left). TEM cross section of the multilayer after 10 periods (right). The different layers are indicated in period 6 in the images.	137
13.8	(a) Development of the working gas pressure of <i>gas-ML</i> and the first period of <i>LP-a (2.5)</i> . <i>In situ</i> measurements during the first three periods of <i>LP-a(2.5)</i> (b) and <i>gas-ML</i> (c). The mean value is indicated by a green line. The minima of the growth oscillations are highlighted by dotted lines for better comparison for the first period.	139
13.9	(a) Experimental <i>in situ</i> data during the variations of the gas. The amplitude is strongly damped and the period of the oscillation is changing. (b) Estimated rate of thickness increase from experimental data (black squares) and calculated deposition rate (red circles) during the pressure variations. F_D and the deposition rate decrease with increasing pressure.	140
13.10	Experimental data and best simulations of angle-dependent XRR measurements of <i>LP-a(2.5)</i> and <i>gas-ML</i> after the deposition of the 10 th period. The curves are shifted for better comparison. (b) and (c) δ - profiles used for the simulation of the XRR data for both samples.	141
A.0	Scheme of the growth model. The integration range is indicated by a red box.	171

List of Tables

2.1	Properties of monocarbides of Group IVA and VA - transition metals after [Tot71, Pie96, GES14, ICS14]	20
5.1	Overview of all samples presented in this work. → indicates, that the growth parameter is not constant over the entire deposition time.	43
6.1	Table presenting the input parameters (electron density and SBE) for SRIM and TRIDYN simulations	59
6.2	Table presenting the results of the SRIM and TRIDYN simulations for the average energy E_{sp} and the total sputtering yield Y_{tot} of the sputtered particles.	59
9.1	Table presenting the resulting average energy E_{sp} and the sputter yield Y of the sputtered particles at the DC power of 50 W and 200 W.	84
9.2	Results of the SIMTRA simulations: Fraction of the sputtered particles arriving on the substrate N/N_0 for $N_0 = 10^7$ sputtered particles from the target and the average final energy E_{final} . The energy dependent mean free path at $p = 0.2$ Pa was calculated using the average energy E_{sp} of the sputtered particles, determined by TRIDYN simulations.	86
10.1	The average energy E_{sp} of the sputtered particles was determined by TRIDYN simulations. From this, the energy dependent mean free path at $p = 0.2$ Pa and $p = 4$ Pa was calculated. Values for mass and radii are taken from the SIMTRA program. The fraction of the sputtered particles arriving on the substrate N/N_0 was simulated using SIMTRA.	94
10.2	Background subtraction method and relative sensitivity factors (R.S.F.) used for the determination of the chemical composition of the VC samples.	97
10.3	Results for the chemical composition of the VC_{1-x} thin films grown at a Ar pressure of 0.2 Pa by XPS and EPMA, and Ar pressure of 2 Pa by XPS	97
13.1	Thickness D , roughness σ and electron density ρ_e for the different layers, used as input for the simulation of the XRR measurements.	135

- 13.2 Thickness D , roughness σ and electron density ρ_e used as input parameter to simulate the angle-dependent XRR measurement of the *non-interruption* multilayer. The roughness was increased by $\Delta\sigma = 1\text{\AA}$ for each period n to account for the roughening of the system. 140

Growth model: Calculations

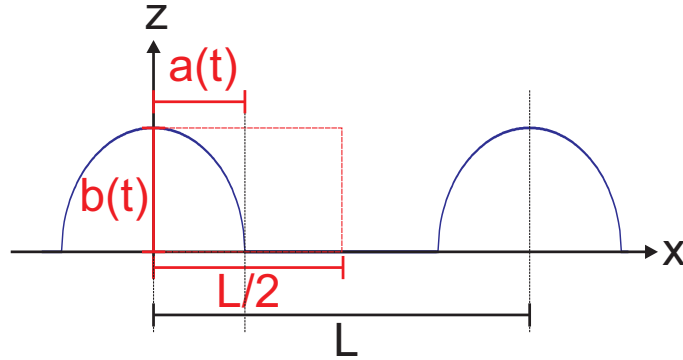


Figure A.0: Scheme of the growth model. The integration range is indicated by a red box.

In this section, the calculations of the time-dependent maximum height and roughness for the island model, depending on the distance L and shape γ are presented (s. Chap. 11).

For the calculations, the symmetry of the model was taken into account (s. Fig. A.0). The integration range in x -direction was performed in all cases in the interval $[0, L/2]$.

The time-dependent height $z(x, t)$ is given by (s. Eqn. 12.10):

$$z(x, t) = \begin{cases} \gamma a(t) \sqrt{1 - \left(\frac{x}{a(t)}\right)^2} \Theta(a(t) - x) & \text{for } t < t_{touch} \\ \frac{L}{2} \gamma \sqrt{1 - \left(\frac{2x}{L}\right)^2} + F_D \frac{L}{2} t & \text{for } t \geq t_{touch} \end{cases}, \quad (\text{A.1})$$

where Θ is the Heaviside-function.

With Eqn. A.1 for $t < t_{touch}$, the mean height $\langle z(x) \rangle$ is calculated by:

$$\langle z(x, t) \rangle = \frac{1}{(L/2)} \int_0^{L/2} dx z(x, t) \quad (\text{A.2})$$

$$\begin{aligned}
&= \frac{1}{(L/2)} \int_0^{\frac{L}{2}} dx \gamma a(t) \sqrt{1 - \left(\frac{x}{a(t)}\right)^2} \Theta(a(t) - x) \\
&= \frac{1}{(L/2)} \int_0^{a(t)} dx \gamma a(t) \sqrt{1 - \left(\frac{x}{a(t)}\right)^2} \\
&= \frac{\pi \gamma a^2(t)}{2 L}
\end{aligned}$$

For $t \geq t_{touch}$, the shape of islands is kept constant. For the mean height $\langle z(x) \rangle$ is then given by (using Eqn. A.1):

$$\begin{aligned}
\langle z(x,t) \rangle &= \frac{1}{(L/2)} \int_0^{\frac{L}{2}} dx z(x,t) \tag{A.3} \\
&= \frac{1}{(L/2)} \int_0^{\frac{L}{2}} dx \left[\frac{L}{2} \gamma \sqrt{1 - \left(\frac{2x}{L}\right)^2} + F_D \frac{L}{2} t \right] \\
&= \frac{1}{(L/2)} \left[\underbrace{\int_0^{\frac{L}{2}} dx \frac{L}{2} \gamma \sqrt{1 - \left(\frac{2x}{L}\right)^2}}_{\frac{\pi}{4} \gamma L^2} + \underbrace{\int_0^{\frac{L}{2}} dx F_D \frac{L}{2} t}_{\frac{L}{2} F_D L t} \right] \\
&= \frac{\pi}{8} L \gamma + F_D \frac{L}{2} t
\end{aligned}$$

Taking the results of the previous calculations, the rms-roughness $\sigma(t) = \sqrt{\langle (z(x,t) - \langle z(x,t) \rangle)^2 \rangle}$ of the system can be calculated (s. Chap. 3). For $t < t_{touch}$, $\sigma(t)$ is calculated using Eqn. A.1 and the result of Eqn. A.2:

$$\begin{aligned}
\sigma(t)^2 &= \langle (z(x,t) - \langle z(x,t) \rangle)^2 \rangle \tag{A.4} \\
&= \langle z(x,t)^2 \rangle - \langle z(x,t) \rangle^2 \\
&= \frac{1}{(L/2)} \int_0^{\frac{L}{2}} dx \gamma^2 a^2(t) \left(1 - \left(\frac{x}{a(t)}\right)^2 \right) \Theta(a(t) - x) + \\
&\quad \frac{1}{(L/2)} \int_0^{\frac{L}{2}} dx \left(\frac{\pi \gamma a^2(t)}{2 L} \right)^2
\end{aligned}$$

$$\begin{aligned}
&= \frac{\gamma^2 a^2(t)}{(L/2)} \int_0^{a(t)} dx \left(1 - \left(\frac{x}{a(t)} \right)^2 \right) + \\
&\quad \frac{1}{(L/2)} \int_0^{\frac{L}{2}} dx \left(\frac{\pi \gamma a^2(t)}{2 L} \right)^2 \\
&= \frac{\gamma^2 a^2(t)}{(L/2)} \left(\frac{2}{3} a(t) \right) + \left(\frac{\pi \gamma a^2(t)}{2 L} \right)^2 \\
&= \frac{\gamma^2 a^3(t)}{(L/2)} \left(\frac{2}{3} - \left(\frac{\pi}{4} \right)^2 \frac{2 a(t)}{L} \right) \\
&\rightarrow \sigma(t) = \sqrt{\frac{\gamma^2 a^3(t)}{(L/2)} \left(\frac{2}{3} - \left(\frac{\pi}{4} \right)^2 \frac{2 a(t)}{L} \right)}
\end{aligned}$$

For $t \geq t_{touch}$, $\sigma(t)$ is calculated by using Eqn. A.1 and the results of Eqn. A.3:

$$\begin{aligned}
\sigma(t)^2 &= \langle (z(x,t) - \langle z(x,t) \rangle)^2 \rangle \tag{A.5} \\
&= \frac{1}{(L/2)} \int_0^{\frac{L}{2}} dx \left[\frac{L}{2} \gamma \sqrt{1 - \left(\frac{2x}{L} \right)^2} + \right. \\
&\quad \left. F_D \frac{L}{2} t - \left(\frac{\pi}{8} L \gamma + F_D \frac{L}{2} t \right) \right]^2 \\
&= \frac{1}{(L/2)} \int_0^{\frac{L}{2}} dx \left[\frac{L}{2} \gamma \sqrt{1 - \left(\frac{2x}{L} \right)^2} - \frac{\pi}{8} L \gamma \right]^2 \\
&= \frac{1}{(L/2)} \int_0^{\frac{L}{2}} dx \left[\left(\frac{L}{2} \right)^2 \gamma^2 \left(1 - \left(\frac{2x}{L} \right)^2 \right) + \right. \\
&\quad \left. \left(\frac{\pi}{8} \right)^2 L^2 \gamma^2 - \left(\frac{\pi}{8} L^2 \gamma^2 \sqrt{1 - \left(\frac{2x}{L} \right)^2} \right) \right] \\
&= \frac{2}{3} \frac{L^2}{4} \gamma^2 - \left(\frac{\pi}{8} \right)^2 L^2 \gamma^2 \\
&= \frac{L^2}{4} \gamma^2 \left(\frac{2}{3} - \left(\frac{\pi}{4} \right)^2 \right) \\
&\rightarrow \sigma(t) = \sqrt{\frac{L^2}{4} \gamma^2 \left(\frac{2}{3} - \left(\frac{\pi}{4} \right)^2 \right)}
\end{aligned}$$

Acknowledgments

Ich möchte mich an dieser Stelle bei allen Personen bedanken, die zum Gelingen dieser Arbeit beigetragen haben. Mein Dank gilt insbesondere

- Tilo Baumbach, dass er mir die Möglichkeit gegeben hat an ANKA/IPS zu promovieren. Während dieser Zeit hat er mir viele Freiheiten gegeben, um mich sowohl wissenschaftlich als auch persönlich weiterzuentwickeln. Durch die Arbeit an ANKA konnte ich viel lernen und neue Einblicke in die abwechslungsreiche Forschung an Synchrotronstrahlungsquellen gewinnen.
- Dagmar Gerthsen für die Übernahme des Korreferats, ihr Interesse an meiner Arbeit und die Bereitstellung der TEM Messungen.
- Bärbel Krause für die tolle Betreuung in den letzten Jahren. Ihre ständige Unterstützung und ihre Motivation waren immer ein großer Antrieb für mich. Ich habe in dieser Zeit unheimlich viel von ihr gelernt. Danke!
- Sunil Kotapati for suffering together with me through all beamtimes, for performing several complementary measurements, and for a very nice working atmosphere.
- the former members of the research project sputtering: Susan Darma, Jochen Gemmler and Franz Schotsch for fruitful discussions and support.
- allen Menschen die mich bei meiner Arbeit im UHV Analysis Labor unterstützt haben, besonders Hans Hellmuth Gräfe, Annette Weißhardt und Anja Seiler.
- Martin Köhl für viele Diskussionen und seine Hilfe - nicht nur, wenn es um Formeln ging.
- Miguel Mantilla and Peter Wochner for support at the MPI Beamline at ANKA.
- Reinhard Schneider, Erich Müller, and Nadejda Firman, LEM, KIT für die Erstellung der TEM/SEM Bilder. Danke auch dafür, dass sie sich soviel Zeit genommen haben, um die Bilder zu analysieren und die Ergebnisse zu diskutieren.
- Michael Stüber, Sven Ulrich und Kolja Erbes, IAM-AWP, KIT für zahlreiche ertragreiche Diskussionen zum Thema Sputtern und Hartbeschichtungen und die Durchführung der Mikrosondenmessungen.

- Svetoslav Stankov and Shyjumon Ibrahimkutty for their support at the DiffLab at ANKA.
- Lothar Weinhardt und Dagmar Kreikemeyer-Lorenzo für die Unterstützung bei den XPS Messungen/Analysen.
- Thomas van de Kamp und Elias Hamann für das Korrekturlesen und das berühmte offene Ohr zu jeder Zeit.
- meinen Freunden, Janina Bittighofer, Patrice Brenner und Martin Hoßbach, meiner Familie, besonders meinen Eltern Jutta Kaufholz-Zachmann und Günter Zachmann, und vor allem Daniel Hänschke für ihre großartige moralische Unterstützung in den letzten Jahren.